Technische Universität München

TUM SCHOOL OF NATURAL SCIENCES

On-Surface Synthesis and Characterization of Porphyrin Square Tetramers, Gulf Edged Graphene Nanoribbons and Nanoporous Graphene

Eduardo Enrique Corral Rascon

Vollständiger Abdruck der von der TUM School of Natural Sciences der Technischen Universität München zur Erlangung des akademischen Grades eines Doktors der Naturwissenschaften (Dr. rer. nat.) genehmigten Dissertation.

Vorsitz: Prof. Dr. David Egger

Prüfer der Dissertation:

1. Prof. Dr. Willi Auwärter
2. Prof. Dr. Michael Gottfried

Die Dissertation wurde am 18.10.2022 bei der Technischen Universität München eingereicht und durch die TUM School of Natural Sciences am 16.11.2022 angenommen.

Abstract

With the continuous reduction in size of integrated circuits (IC), and other building blocks of electronic devices (ED), these have entered the nanometer scale. The current trend of the scientific efforts aim to replace silicon as the base element of ED for carbon based ones. In this thesis, we present the characterization of organic materials, with tools from the field of Scanning Probe Microscopy (SPM), such as Scanning Tunneling Microscopy (STM), Scanning Tunneling Spectroscopy (STS), and Atomic Force Microscopy (AFM).

Specifically, we present an on-surface chemistry route to synthesize square-like porphyrin tetramers with a central cyclooctatetraene (COT) ring, coexisting with other oligomers. This approach employing temperature-induced dehydrogenative porphyrin homocoupling on Ag(100) in an ultra-high vacuum (UHV) environment provides access to surface-supported, unsubstituted porphyrin tetramers that are not easily achievable by conventional synthesis means. The monomeric free-base (2H-P) and Zn-metalated (Zn-P) porphines were employed to form square-like 8H-P and 4Zn-P tetramers on Ag(100). An atomic-level characterization by bond-resolved atomic force microscopy (AFM) and scanning tunneling microscopy and spectroscopy (STM) is provided, unequivocally identifying the molecular structures.

In this thesis is also reported the bottom-up on-surface synthesis of well-defined gulf-type graphene nanoribbons (g-GNR)s and their lateral fusing induced nanoporous graphene (NPG) structures on Au(111). The g-GNRs bear wide-bandgap and foster delocalized frontier orbitals which appear confined along the edges when probed with scanning tunneling microscopy/spectroscopy. The thermal lateral fusion of g-GNRs produces atomically precise NPG structures with electronic isotropy and a wide-bandgap. Despite the delocalized nature of the frontier orbitals, they appear localized at the nanopores and NPG borders. DFT calculations show that even though such states bear a high resemblance to image potential states or super atom molecular orbital states, they originate from the conduction bands instead.

In addition to the structural and electronic characterization of the g-GNRs we present an analysis of the structural defects and reaction pathways that are chemically agreeable to explain how some of these structures came to be. The analysis has the aim of presenting data that can serve as the basis to improve the structure of monomers that may be utilized for the bottom-up on-surface synthesis of GNR.

With these results we have added to the collective scientific and technical knowledge, the understanding and properties of in-situ synthesis of elements that may be utilized as basic elements of ED with free-base and zinc metalated porphines, as well as g-GNR.

Table of Contents

Chapter 1 Introduction

Electronic devices form part of our daily lives, as they are nearly omnipresent, either as part of our jobs, personal entertainment in leisure times, or even indirectly, by being used by any of the service providers that sustain our modern life style. At the time of writing this thesis, silicon chips face a shortage due to the economic factors 2 years after the beginning of the Covid-19 global pandemic and the intrinsic nature of the fabrication of integrated circuits which is resource intensive[1].

In 1965 Gordon Moore made the prediction that the amount of transistors would double every two years[2]. As it happens to be the case, this trend now faces physical limitations[3] and when we take into consideration the amount of waste from electronic devices (e-waste), its poor management[4] and the health factors associated with it[5], we see the need to develop technologies that can replace the existing ones.

Depending on the type of integrated circuit (IC), the materials used must fulfill a function. Porphyrins have the potential to be used as logic gates, or for information storage[6-8]. To connect to the electrodes that power the devices we find conductive elements in the form of graphene nanoribbons (GNR) that can also be employed to create field effect transistors (FET) devices[9-11]. Materials such as NPG remain an area that remains largely unexplored, and thus, no potential applications can currently be properly proposed without knowledge of their properties.

Before any new development reaches implementation several challenges need be overcome. For decades now, the current method of fabrication of electronic devices is the top-down (TD) approach, in which the bulk material is given its final shape and function. Another approach, the bottom-up (BU), takes the opposite route, in which basic building blocks are sequentially put together to assemble the final product[12]. The development of scanning probe microscopy (SPM) allowed for the analysis of ever smaller materials that has reached the manipulation of individual atoms[13] and resolution of chemical bonds[14].

Electronic devices are comprised by several components that fulfill different functions, such as energy storage, conduction, interpretation of signals in the form of logic gates, among others. Depending on chemical structure, organic and organometallic compounds have been divided as *small molecules* and polymers[15-17]. Porphines belong to the small molecule class, while GNRs are polymers. The monomeric precursors used in this work are shown in figure 1.1. A brief reminder

for the reader are the definitions of porphyrins and polymers according to the International Union of Pure and Applied Chemistry (IUPAC)[18]:

Porphyrins. Natural pigments containing a fundamental skeleton of four pyrrole nuclei united through the α-positions by four methine groups to form a macrocycle structure.

Macromolecule. A molecule of high relative molecular mass, the structure of which essentially comprises the multiple repetition of units derived, actually or conceptually, from the molecules of low relative molecular mass.

Polymer. A substance composed of macromolecules.

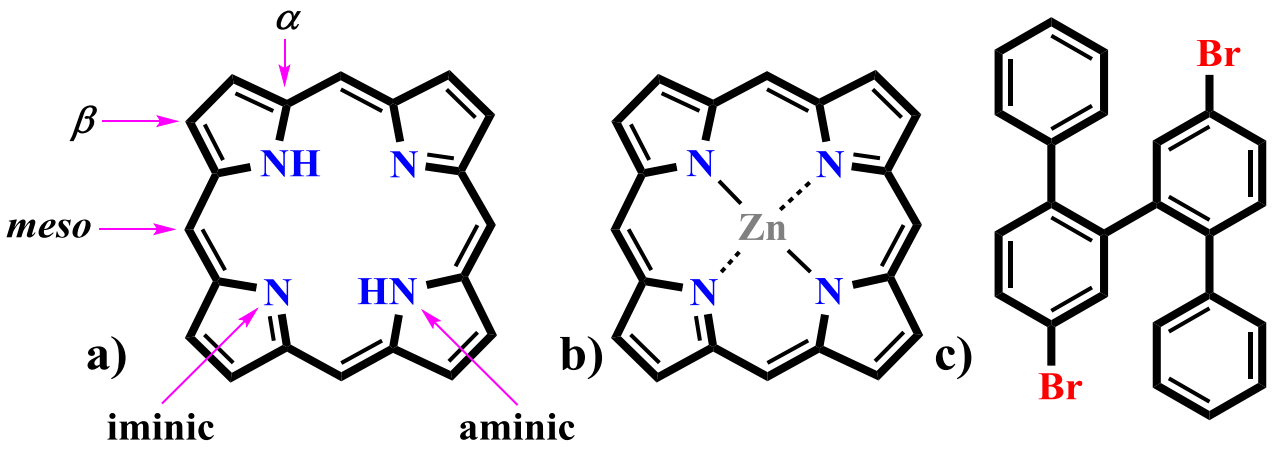

Figure 1.1 Molecules used in this work. a) free-base porphine with marked positions (2H-P). b) Zinc metalated porphine (Zn-P). c) Dibromo quarterphenyl (DBQP). Hence forth these molecules will be treated as monomers and structural details will be introduced in the respective section of the thesis.

The manner in which these molecules can be/need to be processed to fabricate electronic devices will not be addressed in this thesis, nor is the fabrication of devices. Preceding those stages is the elemental research that must be performed to find suitable elements and understand how these work. In this regard porphyrins are promising candidates for the fabrication of electronic devices, with the proof of concept in the published studies 8, 19, but as seen on the methods that were employed, these require the bulk properties of the materials. In the TD approach the material is eliminated while leaving room for the electric connections. The ideal BU approach would be to build a device by carefully placing the many components of a device, however current methodology of the BU approach also requires the removal of material in the transition from one step to another of the elaboration of electronic components as seen in the methodology of reference

20. There is yet another approach to employ molecules to create devices, in so called single molecule devices (SMD). For the elaboration of such devices a molecule must be placed in a desired configuration, in a determined point of space, and while it is true that this poses a challenge, we can find literature on the topic, even specifically on porphyrins[21-23].

For a molecule to be used as a molecular switch it should display a reversible switching process between at least two stable states. Free-base porphyrins and phthalocyanines will be discussed. Tautomerization of free-base porphyrins is spontaneous in solution and in solid state, more specifically single crystals employed for X-ray crystallography[24], not to be confused with on-surface studies. Studies have also been performed on the tautomerization process of monodeprotonated porphyrins in solution[25]. With the advent of surface science, control has been gained over this process at cryogenic temperatures. Initial studies to control the tautomerization process of naphthalocyanines were performed on insulating bilayers of NaCl on Cu(111), in which a double proton transfer is reported in a 90° process[26]. However, on Ag(111) there was no need for insulation and the process was carried out on the bare metal, the same report includes control over metalation process[27]. A report on tetraphenylporphyrins (TPP) includes not only the tautomerization of both inner H atoms, but also on the monodeprotonated core in which the remaining H atom can move to either of the adjacent N atoms or to that at the opposite position[28]. In the previous experiments the movement of the inner H atoms was largely aleatory. This is much different on Ag(100), in which upon deposition, phthalocyanine displays prochiral electronic features at low bias[29]. Depending on the manner of adsorption the movement of the inner H would be clockwise or counterclockwise, the directionality could be reversed upon manipulation of the molecule[30, 31]. Due to the substitution pattern of phthalocyanines it is not possible to have two adjacent monomers that do not break symmetry or the continuous native structure has to change. In this regard porphyrins have higher flexibility, covalent dimers or even higher structures can be made to have one, two or three bonds between subunits. Of the triply linked motif, references 6 and 7 threat the change of electron transport properties. Our research group has published results on two types of free-base porphyrin on Ag(111) which include tautomerization and homocoupling[32, 33].

In 2H-P dimers (4H-P) the conductive properties are thought to be ruled by the position of the inner H atoms[6, 7]. Worth noting is that the previously mentioned process of tautomerization has so far eluded any form of control at room temperature, preventing practical applications. These inner H

atoms can be substituted by metals as a form of functionalization. Evidence indicates that the coordinated metal center in porphyrins plays a minimal role in the manner in which the current flows through porphyrins[34-38]. A property of metalated porphyrins that may be exploited is their ability to hold charges, as free-base porphyrins are unable to hold charge without chemical changes that inherently change their chemical structure[39, 40], while metalated porphyrins can do that though this does not mean these are not prone to structural changes[41]. Finally it can be mentioned that the metal centers can coordinate to other molecules, a property that has been used to perform SMD studies[34, 35, 38].

The components of electronic devices require connections that make it possible to power them or the conduction of signals that are interpreted by the many components that comprise them. GNRs are a class of molecules that are subject of research to fit this purpose by serving as nanowires[42-45]. A key aspect explored for this thesis, was the research in GNR, a carbon allotrope, that much like graphene, is comprised of C atoms with sp^2 hybridization, with the difference that it has a one-dimensional structure. The classification is by the type of edges and width, the precursor can be modified to make the inclusion of heteroatoms, create vacancies or non-hexagonal moieties[46], examples of these features are presented in figure 1.2. A more comprehensive list can be found on reference 47, the text also covers synthesis and properties.

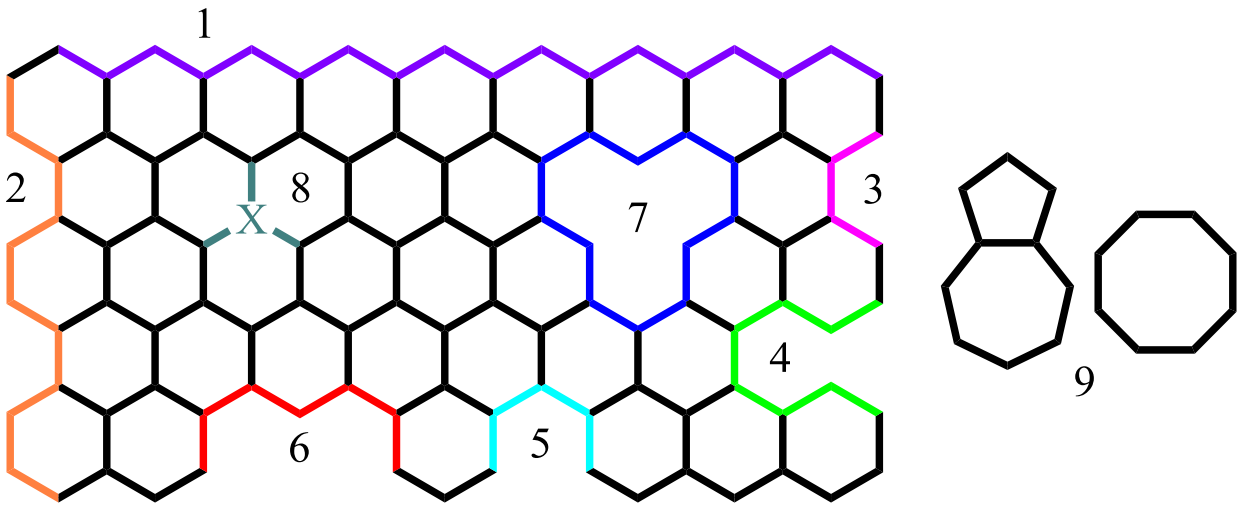

Figure 1.2 Structural features of the various forms of graphene. Simplified drawing of a graphene sheet depicting a non-exhaustive amount of types of edges and internal modification. C atoms are to be considered to be have sp^2 hybridization. H atoms removed for clarity. Color coded and numbered: 1) zig-zag edge. 2) arm-chair edge. 3) bay. 4) fjord. 5) cove. 6) gulf. 7) vacancies. 8) heteroatoms. 9) 2 types of non-hexagonal moieties.

Worth noting is that GNR and other carbon allotropes can be made to fuse laterally to create graphene sheets that may include similar structural features to the parent compound. A class of graphene that has appeared using this methodology is one with vacancies of controlled size. This supramolecular structure is termed nanoporous graphene (NPG)[48-54]. Devices were constructed in the work of references 50, 53 and 54. Overall there is limited data on NPGs, as such there, therefore all data acquired has novelty, a feature most suitable for a doctoral thesis.

Thermally activated on-surface synthesis on coinage metals

To achieve the construction of new macromolecules of interest, an *in-situ* approach was taken, consisting on the deposition of precursors that can be sublimated on a substrate that can catalyze the reaction and in which the necessary measurements for characterization can be performed. The reactions employed in this thesis were based on thermally activated processes and catalyzed by metals, in this case Ag(100) and Au(111). A brief summary is presented next.

The reaction mechanism of the Ullmann coupling has been studied since the first successful use in the synthesis of GNRs on Au(111)[55]. A general reaction mechanism can be proposed for the plethora of monomers covered in literature. The synthesis of GNR typically utilizes monomers with two or more halogens in its structure, though typically bromine (Br) is utilized, iodine (I) and chlorine (Cl) have also been employed[56, 57]. Due to the much different chemistry of Cl[56, 58], the following text will be about the more reactive Br and I halogenated compounds. On scheme 1.1 can be observed the different reactions that take place in the synthesis of GNR and NPG. Starting at the monomeric stage, upon deposition, a hemolytic cleavage of the halogen bond takes place and a C radical is formed. An organometallic stage then can take place and finally a C-C bond is formed[59-61]. It is in this stage that the Ullmann coupling reaction has ended. The resulting oligomer can then undergo another type of reaction, a dehydrogenation process. The first of two reported graphitization processes involves the removal of H atoms within the oligomeric structure which finalizes the planarization of the GNR. A final graphitization process involves the lateral fusion of the resulting GNR. This step typically requires the loss of H atoms running along the periphery of the GNR and the formation of C-C bonds at either selected sites or the complete structure. The resulting products are known as graphene nano networks (GNN)[49, 50, 53, 62] of which NPG is a subclass of.

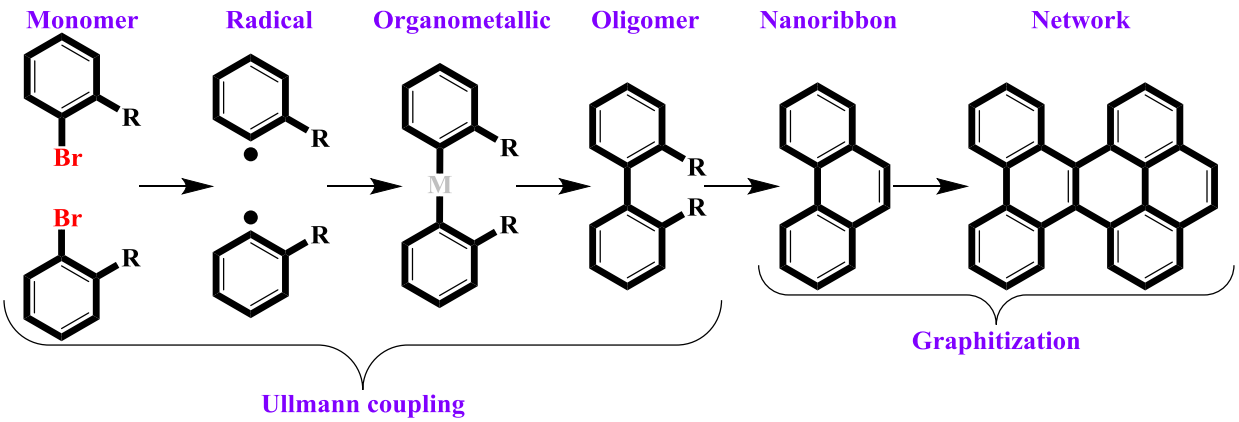

Scheme 1.1 Stages of the on-surface synthesis of GNR. Thermally activated sequence of steps in the synthesis of a GNR/GNN.

Complementary to the GNR precursors, two types of porphines were also employed for the covalent coupling of larger macrocycles on coinage metals. The on-surface coupling of porphyrins can be divided in two types depending on the structure to be coupled. The coupling can be by the porphyrin macrocycle itself[33, 63] or by the chemical groups at the outer edge (e.g. phenyl)[64]. In this thesis, we focus on the former scenario, aiming for the coupling of the unsubstituted macrocycle, porphines.

The chemical products of porphine dehydrogenation varies on each of the coinage metals. On Cu(110), as temperature increases, the first reaction is the self-metalation of the core of the porphine, that is, if it does not currently chelates another metal. C-C bonds are not reported to be formed, rather once the molecule loses H atoms, it readily forms C-Cu bonds, and if enough precursors are present the resulting product is an organometallic one, with C-Cu-C between monomers. Multiple binding motifs are reported[65-68]. Organometallic stages are also reported for 5,15-diphenyl porphyrins on Cu(110)[68] and Cu(111)[69], in which the most reactive sites correspond to the porphyrin macrocycle. The chemistry of porphyrins on Ag(111)[33] and Au(111)[63] is different, as there is no reported organometallic stage. On Ag(111) the newly formed C-C bonds are primarily at the *meso* position, with further dehydrogenation taking place and planarizing the molecule in a cyclodehydrogenation process. Three binding motifs are reported, with the highly ordered triply linked dimers being the preferred product at low coupling temperatures[33]. On terraces of Au(111), for unsubstituted porphines, there were four binding motifs identified, with a clear preference for doubly linked dimers at sufficiently high temperatures. No organometallic stage was identified[70]. Finally, worth noting is that highly ordered polymers, consisting of triply linked subunits, were obtained with the Zn-metalated, 5,15-diphenalenyl substituted porphyrin on Au(111)[71]. The

authors do not attempt to explain why the compound exhibits this chemical specificity, but it may be due to a combination of steric factors and the delocalization of the radicals at the β positions that make them the most reactive sites.

In summary, on-surface results that are available in literature include porphine dimers, disordered oligomers and linear oligomers, but no square-like oligomers or regularly structured C-C coupled two-dimensional porphine sheets.

Worth noting is that the coupling of porphyrins on Ag(111) and Au(111), as well as the cyclodehydrogenation of porphyrins and GNR oligomers, are reactions that find a counterpart in solution chemistry. The on-surface approach has been compared to *oxidative coupling* and *oxidative cyclodehydrogenation*, for which the reader is invited to research on the topic of Scholl reaction and oxidative agents[72].

Chapter summary

Chapter 2 will treat the fundamentals of the STM, AFM and STS techniques, as well as the equipment employed for this work.

In chapter 3 the bottom-up synthesis via surface assisted dehydrogenative coupling and characterization of two types of square porphine tetramers are presented. The characterization of these macromolecules includes evidence of covalent coupling of porphines via AFM imaging and lateral manipulation, as well as dI/dV maps for its electronic properties. Theoretical insights were provided as part of a collaboration with the group of Dr. Pavel Jelinek, including, Dr. Pingo Mutombo, and Adam Matej, from the Institute of Physics of the Czech Academy of Sciences.

In chapter 4 the structural and electronic characterization of two distinct products of consecutive graphitization of DBQP is presented. The first of which is the gulf edged GNR structure 3-CGNR-1-1, the second product is NPG which is obtained by lateral fusion of the previously mention GNR. As part of a collaboration, computational results were provided by Xavier De Cerio and Dr. Aran García Lekue from the Donostia International Physics Center. The DBQP precursor was provided by Dr. Hiroshi Sakaguchi from Kyoto University.

In chapter 5 the possible reaction mechanisms that lead to the side products observed after the graphitization process of the DBQP oligomers are discussed.

In chapter 6 the results are summarized, conclusions are offered and an outlook is presented.

Chapter 2 Experimental Methods

The experimental data in this work was measured with a machine that employs qPlus sensor tips, thus combining two types of scanning probe microscope (SPM), Scanning Tunneling Microscope (STM) and non-contact Atomic Force Microscope (nc-AFM).

The first kind of SPM was invented by Binnig and Rohrer in 1982, their work was rewarded with a half of the Nobel Prize in Physics of 1986. In their work, they proved it was possible to produce an image of a surface using tunneling effect[73, 74]. This technique is limited to conductive samples, mostly metallic, for this reason, the AFM was developed in 1986, by Binnig, along with Quate and Gerber[75], which allowed the imaging of non-conductive samples.

It would be until the mid-90´s with the work of Giessibl that true atomic resolution would be achieved with AFM. More recent breakthroughs include research would continue until the imaging of chemical bonds in molecules[14, 76].

The fundamentals for these techniques will be described in the following sections, more in-depth explanations can be found elsewhere[77-87].

2.1 Scanning Tunneling Microscopy (STM)

2.1.1 Tunneling Effect

The STM junction is comprised by three main components, these are tip, vacuum and sample as depicted on figure 2.1(a), of which tip and sample are metallic. In classical mechanics an electron cannot overcome a barrier if the barrier height exceeds the electron's energy. However the concept that dominates STM is quantum tunneling, in which an electron of energy E can go through a barrier $\phi > E$. In quantum mechanics the electrons of a solid are described by a wave function (ψ).

The tunneling current exponential decay of one order of magnitude for every 100 pm between sample and tip is the property of STM that makes it possible to produce images with atomic resolution. It is this decay that confines tunneling current to the front-most atom of the metallic tip and through which it flows to the sample.

The wave function ψ decays exponentially in the barrier (red line in figure 2.1 c),

$$\psi(z) = \psi(0)\exp - \frac{\sqrt{2m(\phi - E)z}}{\hbar}$$

(equation 2.1)

in which *m* corresponds to the mass of the particle and $\hbar$ (1.05 * 10-34 J*s) is the Dirac constant. The tunneling current I_t is then calculated by considering the density of states of the sample, $\rho_s(E_F)$, at the Fermi edge:

$$I_t \propto V\rho_s(E_f)\exp\left[-2\frac{\sqrt{2m(\Phi - E)z}}{\hbar}\right] \propto V\,\rho_s\,(E_F)e^{-1.025\sqrt{\Phi z}}$$

(equation 2.2)

The barrier Φ is considered to be in *eV* and distance *z* is in Angstrom units. In the work of Binning *et al*., the work is performed on Au(110) as such the barrier height is of 5 *eV*, corresponding to the work function of gold.

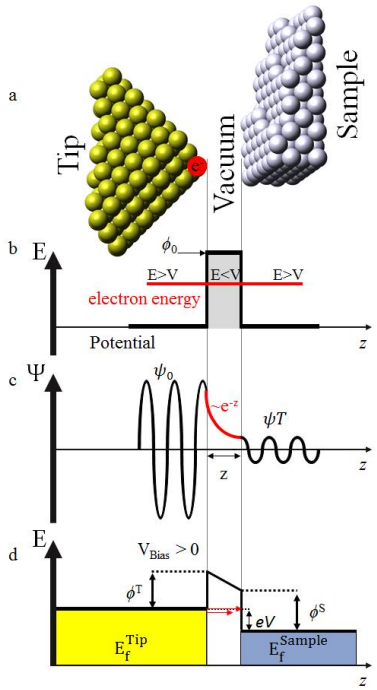

Figure 2.1 Tunneling process scheme. a) Real space scheme. Vacuum gap *z* separates the tip and sample. In a classical view electrons do not flow as the circuit is not closed. b) Energy diagram. The metal tip-vacuum-metal arrangement imposes a barrier for the electrons (thick black line under the assumption that the work function is the same for tip and sample). The energy of the electron is indicated by the red line. c) Wave function graph. The electron wave function ψ_0 oscillates in front of the barrier, decays in the barrier of width *z* as it is transmitted as ψ_T and oscillates past the barrier. d) Tunneling junction with a positive bias applied to the sample. In the limit of zero temperature and small voltages only electrons at the Fermi energy contribute to the tunneling current.

The operation of an STM is in three-dimensions, but the previous model describes a single dimension. Matching the work of Binning *et al*., Tersoff and Hamman showed that equation 2.2 can be applied to such a landscape under the assumption that the tunneling tip wave function is approximated by a spherical *s*-wave and $\rho s(E_f)$ is the local density of states of the sample (LDOS)[73, 74, 88, 89].

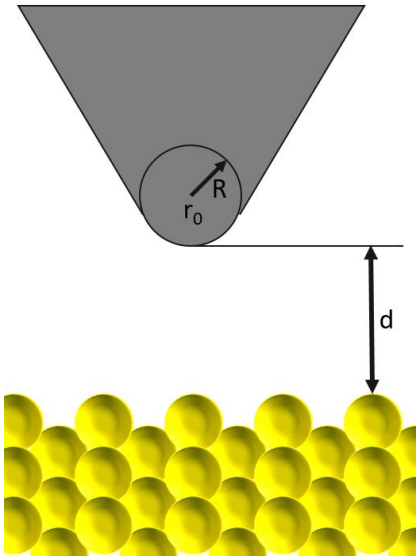

Figure 2.2 Tersoff-Hamman schematic of tunneling geometry. The shape of the tip is arbitrary but it is assumed that locally, the closest point to the surface, is spherical. Radius of curvature *R*. Distance of nearest approach is *d*. Center of the curvature of the tip r_0. Figure reproduced from reference 89.

The Tersoff-Hammann model[88, 89] has its basis on the transfer Hamiltonian approach, which was introduced by Bardeen[90]. The tunneling current between electrodes (tip and sample) separated by an insulator (vacuum) is considered to be

$$I_t = \frac{4\pi e}{\hbar}\int_{-\infty}^{\infty}[\mathrm{f}(E_F - eV + \varepsilon) - \mathrm{f}(E_F + \varepsilon)]\,\rho_s(E_F - eV + \varepsilon)\rho_t(E_F + \varepsilon)M^2\mathrm{d}\varepsilon$$

(equation 2.3)

in which

$$\mathrm{f}(E) = \frac{1}{1 + e^{(E-E_F)/k_\mathrm{B}T}}$$

(equation 2.4)

is the Fermi function, the density of states of the "*electrodes*" ρ_s and ρ_t correspond to sample and tip, e is the electron charge, $\hbar$ is Planck´s constant, ε is an integration variable, and finally, Bardeen showed that the tunneling matrix element *M* is given by

$$M = \frac{\hbar}{2m} \int_{\text{surface}} \left(\psi_s^* \frac{\partial \psi_t}{\partial z} - \psi_s \frac{\partial \psi_t^*}{\partial z} \right) \mathrm{d}S$$

(equation 2.5)

In here the wave functions ψs, ψt correspond to those of the tip and sample respectively. The problem is solved for the sample and the tip separately and then the matrix element is determined according to (2.5). Equation (2.5) can be simplified at low voltages to

$$I_t = \frac{4\pi e}{\hbar} \int_0^{eV} \rho_s(E_F - eV + \varepsilon)\rho_t(E_F + \varepsilon)M^2 \mathrm{d}\varepsilon$$

(equation 2.6)

If we have a flat LDOS tip, the ρ_t is constant in the studied energy range, this in turn means that the energy dependent part of the tunneling is determined by the sample:

$$I_t \propto V\rho_s(E_F - eV)$$

(equation 2.7)

Then we can make the statement that the tunneling current is determined by the LDOS of the sample at the Fermi energy at the position of the tip r_0 (figure 2.2). In simpler words, this means that the tip follows the contour of the surface DOS for a constant current. A feedback loop of the STM adjust the tip height to keep the current constant.

2.1.2 Scanning Tunneling Spectroscopy (STS)

As STM depends on the DOS, the signal is influenced not only by the topography of the surface that is subject of research, but also its electronic structure. STS was proposed by Selloni *et al.* in 1985 with an experiment on graphite[91]. Further experimental demonstrations were done by Feenstra and coworkers[92-94], where they computed how the derivative of the tunneling current *I* is related to the electronic states of the surface using a simplified tunneling model. The goal in an STS experiment is to obtain the density of states of the sample. Two elements are required to record spectroscopic data, these are tip and sample, and as such, a tip with a flat density of states

must be reproducible. The tunneling current can be written as stated in equation 2.8 when the voltage is small, temperature low and the tip-sample distance is as short as a few Å.

$$I \propto \int_0^{eV} \rho_s\,(\vec{r}_0, E)\rho_t(\vec{r}_0, E - eV)T(E, eV, d, \phi)\,dE$$

(equation 2.8)

In here the position of the tip over the sample surface is represented by $\vec{r}_0$, d is the tip-sample distance, and T is the transmission probability that depends on the energy of states involved, the bias voltage applied between the tip and sample, and the work function of both tip and sample. The relation of any two can be measured in STS, for this, the third one must remain fixed. Three modes of spectroscopy measurements result from this: (1) *I-V* curves, which results as a variation of the tunneling current when the bias voltage is measured while the tip-sample distance remains fixed, (2) *I-z* curves, which is the variation of the tunneling current with as the distance between tip and sample is measured, while the bias voltage V remains fixed, finally, (3) *z-V* curves, variations of the tip-sample distance are measured as function of the bias voltage with a tunneling current that is fixed.

The results presented in this work were performed using only the first of these modes, as such, these will be discussed.

I-V curves

The tunneling current is expressed as equation 2.9 when it is differentiated with respect to the bias voltage.

$$\frac{dI}{dV} \propto \rho_t(0)\rho_s(eV)T(E, eV, d, \phi) + \int_0^{eV} \rho_t(E - eV)\rho_s(E)\frac{dT(E, eV, d, \phi)}{dV}dE + \int_0^{eV} \rho_s(E)\frac{d\rho_t(E - eV)}{dV}T(E, eV, d, \phi)dE$$

(equation 2.9)

For simplification two assumptions are made, that the DOS of the tip is constant and that the transmission coefficient is constant in the V range of the measurement, thus the second and third terms are constant and the final expression is:

$$\frac{dI}{dV} \propto \rho_s(\vec{r}_0, eV)$$

(equation 2.10)

In this approximation, the differential conductance *dI/dV* measures the sample DOS at the energy *eV* relative to the Fermi energy of the sample.

Experimentally, a modulation voltage is superimposed on the direct bias V_{dc} that is applied between the tip and the surface of the sample. The modulation voltage has sinusoidal shape and its frequency ω must be larger than the feedback loop cut-off (alternatively constant height is employed). The current *I* is modulated by ω but the feedback loop does not correct the tip-surface distance (constant height) and the *ac* signal of *I* gives the derivative. The component of *I* which is in phase with ω, which is measured with a lock-in amplifier, giving off the *dI/dV* signal at V_{dc}.

2.1.3 STM Modes of Operation

The STM apparatus has two operation modes, constant current mode and constant height mode, of these, constant current was employed for topographic measurements, and constant height for AFM and spectroscopy.

Constant Current Mode

In this mode a current and a bias are set and a feedback loop is applied to constantly adjust the z-position of the tip in a way that the measured tunneling current stays constant. While the term topography is usually applied for the data obtained in this mode, it is advisable to use it with caution, as described in reference 86, the contours of constant tunneling current are not identical with the contours of constant total charge density, which would be the ideal topography of a surface. Rather, they are related to contours of constant local density of states at the Fermi level (LDOS). On an atomic scale, images often depend on the applied voltage because of variations in the LDOS.

Constant Height Mode

There are two main requirements for this mode, a highly planar surface and low thermal drift typically achieved by working at cryogenic temperatures. The tip moves parallel to the substrate and thus, may come in contact with the surface or material deposited on it, thus changing its properties. To prevent such situation, the instrument is operated in constant current mode and tilt correction is performed electronically before opening the feedback loop. The tip, as usual moves in the *x* and *y* plane but the height *z* can be stablished before every scanned image is obtained or in a single image several height positions may be used[95-97].

dI/dV Map Mode

As explained in the STS section, the *dI*/*dV* information at a specific position above the sample can be obtained by differentiating the I-V curve or directly from the current signal using a lock-in amplifier by modulating the bias. For a *dI*/*dV* map, a specific bias is used and the *dI*/*dV* signal is recorded when scanning a defined region, yielding information on the LDOS at that bias, resulting in the spatial distribution of the electronic states. This mode is typically used at constant height.

2.2 Atomic Force Microscopy (AFM)

STM operation is limited to conductive samples as it relies on the measurement of a tunneling current that must be registered to record any type of image or spectra. In contrast, the AFM imaging mechanism bases on the forces between a sharp tip and a sample (F_{ts}). The tip is mounted at the end of a cantilever which serves as a force sensor. The static deflection of the cantilever or the change in its dynamic properties due to tip-sample forces are then exploited. As depicted in figure 2.3, based on the tip-sample distance we can distinguish three main regions of different interactions. If too far away, the forces between the sample and the tip are negligible (yellow), however, as the tip approaches the sample attractive forces occur (purple) and very short distances repulsive forces start to develop (green). Three operation modes that make better use of these forces have been developed, contact mode AFM (cm-AFM) where the repulsive forces are at their highest, non-contact AFM (nc-AFM) where typically the attractive forces dominate, and

taping mode which covers both of these regions, though it is only nc-AFM in which the text will focus. In different texts[77-83] the reader is informed of the non-monotonous behavior of F_{ts}, which poses additional difficulties for z-feedback[83, 82].

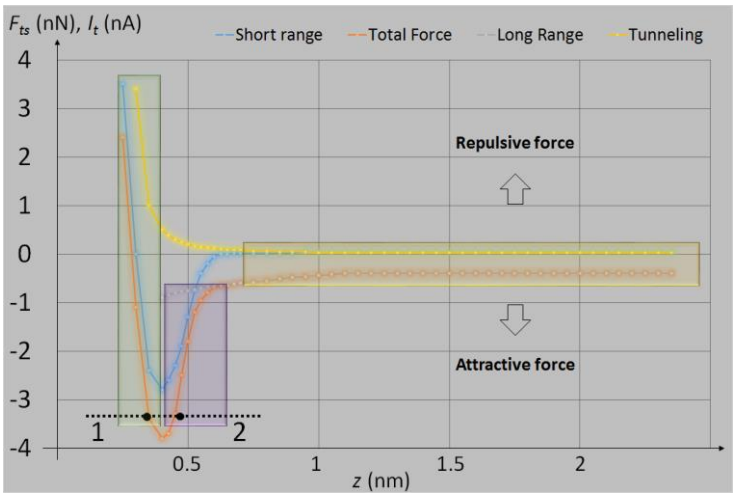

Figure 2.3 Plot of the tunneling current (I_t) and tip-sample force (F_{ts}). Qualitative distance dependence of tunneling current, long and short range forces. Tunneling current increases monotonically with decreasing distance while total force reaches a minimum and increases for distances below bond length. Yellow curve shows the distance dependence of the tunneling current I_t with increasing distance. F_{ts} (Orange curve) is comprised of short and long range forces (Grey curve). Points 1 and 2 are two examples of the non-monotonic behavior of F_{ts}. Graph reproduced from references 78, 82.

The principles of AFM will be explained first, followed by the relevant information regarding the experimental setup used for the results reported in this work.

2.2.1 Tip-Sample Forces

The range in which these forces become relevant need to be considered for proper calibration of the equipment and interpretation of the recorded data.

Pauli repulsion

Depending on the literature chosen, this section can appear as *short range forces* or *chemical forces*. Arising from overlap of electron wave functions and repulsion of ion cores, the range of these forces is then comparable to the extension of the electron wave function (<1nm). Forces are attractive when the overlap of electron waves reduces the total energy, comparable to molecule binding. When the atoms of the tip and the sample approach each other at distances closer

than those in a chemical bond, the repulsion between the inner electron shells becomes important, the repulsive interaction due to the overlap of inner closed shells orbitals is not just electrostatic, there is also the quantum mechanical component of Pauli exclusion principle. Attractive short-range forces are in the order of 0.5-1 nN per interacting atom at tip-sample distances typical for STM operation. The variation of short-range forces on the atomic scale makes atomic resolution possible in force microscopy[98-100].

Empiric model potentials are used for the qualitative discussion of the tip-sample interactions, such as the Lennard-Jones Potential, described as

$$V_{L-J} = -E_{bond}\left(2\frac{\sigma^6}{z^6} - \frac{\sigma^{12}}{z^{12}}\right)$$

(equation 2.11)

where E_{bond} is the bonding energy, z is the distance between the atoms of the surface and sample, and σ is the equilibrium distance. Another model is the Morse Potential

$$V_{Morse} = -E_{bond}\left(2e^{-\kappa(z-\sigma)} - e^{-2\kappa(z-\sigma)}\right)$$

(equation 2.12)

The Morse Potential has an additional parameter, the decay length κ.

Van der Waals Force (vdW)

At distances larger than 1 nm vdW force is the largest force of consideration in this work. The vdW forces are dipole-dipole forces that arise from fluctuations and dipoles induced in their electric field. They are always present and can attract the chemically inert atoms. Three types of dipole interactions are identified, interactions between two permanent dipoles (Keesom force), permanent dipole and an induced dipole (Debye force), and two induced dipoles (London dispersion force), and all three component interactions can be summed[101], thus the vdW potential (V_{vdW}) of two particles at distance d can be modeled as

$$V_{vdW} \propto -\frac{C}{d^6}$$

(equation 2.13)

The distance dependence with the minus sixth power corresponds to a long-range interaction. The van der Waals interaction is non-directional and additive, in the setting used for the experiments of this work, the total force correspond to the forces of the sample and the tip, which is not just the

apex of it, but from the bulk of it, similar principle for the sample, this is due to the long range of the force. The total interaction can be obtained by integration. If the tip of the sphere is considered to be a sphere of radius *R* and the sample considered to be a semi-infinite solid, the resulting van der Waals interaction force is

$$F_{vdW} = -\frac{HR}{6D^2}$$

(equation 2.14)

D is the tip-sample distance measured from the tip apex, and *H* is the Hamaker constant. The Hamaker constant is a material property representing the strength of the van der Waals interaction, It is defined as $H = \pi^2 C \rho_A \rho_B$, with *C* being the coefficient in the atom-atom pair potential in equation 2.13 and ρ_A, ρ_B being the densities of tip and sample. It is important to remember that in UHV conditions vdW forces are always attractive[101-103].

Electrostatic forces

These act between charges on tips and samples. Their strength and distance dependence obey Coulomb's law. Charges can be trapped at sample surfaces during the surface preparation procedure. The decay of the surface charge can be measured by their electrostatic force down to single charges. Charges on the surface may attract metal tips which are necessary for tunneling. The method for determining the force is to calculate the interaction between the charges and their mirror image in the tip. Neutral surfaces that are polar interact with conductive tips via image forces[104, 105]. Electrostatic forces act between conductive tips and conductive samples when they are at different potentials, however, the experimental results presented here were carried out at a constant bias of 0, so contributions to the measurements are assumed to be small (though not nonexistent) and will not be discussed in detail.

Magnetic forces

Though magnetism is relevant to the topic of aromaticity, which will be discussed in the properties of the molecules used for these projects. The experiments themselves are not performed under magnetic fields and as such will not be treated in this text.

2.3 Frequency Modulated Atomic Force Microscopy (FM-AFM)

The experimental data presented here was recorded using a FM atomic force microscope at UHV and cryogenic temperatures (5-7 K). A qPlus sensor was utilized for imaging, and the tip itself was decorated with a CO molecule for bond resolved AFM (br-AFM)[14, 106-110].

2.3.1 Principles of FM-Atomic Force Microscopy

This section follows the following sources 78-80, 82. Atomic Force Microscopy can be divided according to the parameters used to measure the samples, for FM-AFM there are six parameters:

1. the spring constant of the cantilever k,
2. the eigenfrequency of the cantilever (also called natural frequency, which is excited when a piezoactuator oscillates the tip as it hangs freely) f_0,
3. the quality factor of the cantilever Q,
4. the oscillation amplitude A,
5. the frequency shift of the cantilever Δf,
6. the bias voltage between the tip and sample V_t

The first three parameters are determined by the type of cantilever that is used, while the latter three parameters can be freely adjusted. Non-contact AFM (nc-AFM) was developed for UHV and cryogenic environments in which the cantilevers would reach quality factors Q of 10,000 - 30,000. This values limit the acquisition time of dynamic force microscopy, since the oscillation amplitude of the cantilever needs a long time to adjust.

In FM-AFM, a cantilever with eigenfrequency f_0 and spring constant k is subject to controlled feedback in a way that amplitude A of oscillation remains constant during the experimental procedure, as represented in figure 2.4. The tip deflection signal phase is shifted, routed through an automatic gain control circuit and fed back to the actuator which is responsible of the oscillation motion. The input frequency f is a function of f_0, its quality factor Q, and the phase shift φ between the mechanical excitation generated at the actuator and the deflection of the cantilever. If $\varphi = \pi/2$, the loop oscillates at $f = f_0$.

The oscillation frequency is what is measured in FM-AFM and the connection between frequency shift Δf and forces acting between tip and sample must be understood. Stated in reference 80, "*the motion of the cantilever, in which the tip is located, can be described by classical mechanics, in this case a weakly disturbed harmonic oscillator. In* figure 2.4 *is presented the schematic view of an oscillating cantilever (with spring constant k, effective mass m*) the deflection q´(t) of the tip of the cantilever: it oscillates with an amplitude A at a distance q'(t) from the sample. The closest point to the sample is* $q = d$ *and* $q(t) = q'(t) + d + A$"[80].

"*The Hamiltonian for the cantilever is*"

$$H = \frac{p^2}{2m^*} + \frac{kq'^2}{2} + V_{ts}(q)$$

(equation 2.15)

"*where* $p = m^* dq'/dt$. *The unperturbed motion is given by*"

$$q'(t) = \mathrm{A}\cos(2\pi f_0 t)$$

(equation 2.16)

"*and the frequency is*"

$$f_0 = \frac{1}{2\pi}\sqrt{\frac{k}{m^*}}$$

(equation 2.17)

The Resonance frequency shifts due to tip-sample interaction, the cantilever oscillation frequency follows this shift. The frequency shift Δf in FM mode is proportional to a weighted average of the tip-sample force over a cantilever oscillation cycle.

$$\Delta f = \frac{f_0}{2k} < k_{ts} >$$

(equation 2.18)

In classic FM-AFM, k_{ts} varies by several orders of magnitude during one oscillation cycle and a perturbation approach has to be employed to calculate the frequency shift. These approaches are the Hamilton-Jacobi method and the Fourier method.

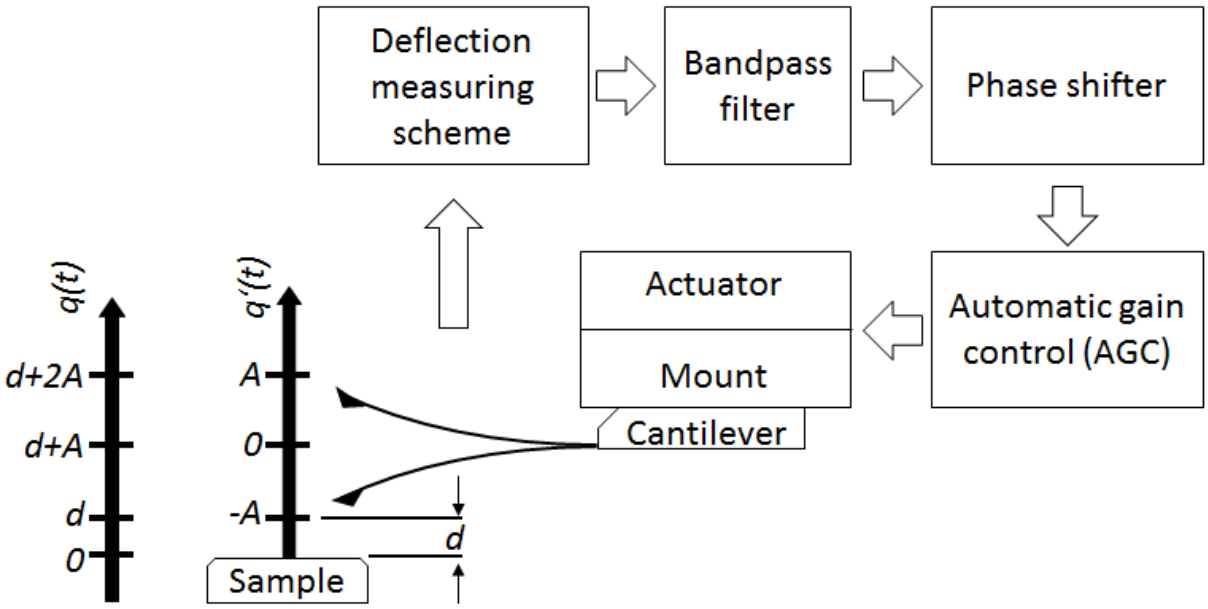

Figure 2.4 Block diagram of the amplitude regulator in FM-AFM. In the schematic view of the oscillating cantilever are given the representation of geometric terms, in which *A* is the amplitude and *d* is the closest distance from the tip to the sample. Input signal is the cantilever´s deflection sensor. The bandpass filter discriminates the noise. The phase shifter changes the sinusoidal signal by 90°. The AGC feeds energy into the cantilever compensating losses. Finally the actuator excites the cantilever[79, 80, 111]. Image reproduced from references 78, 80.

Though the previously mentioned approaches have been employed with success, the mathematical expressions are complicated and as such, integration by parts lead to a simpler one.

$$\Delta f(z) = \frac{f_0}{2k} \int_{-A}^{A} k_{ts}(z - q') \frac{\sqrt{A^2 - q'^2}}{\pi A^2/2} \mathrm{d}q'$$

(equation 2.19)

Based on this equation, the tip-sample forces can be extracted form df measurements. Worth noting is that in real experiments the frequency shift curve $\Delta f(z)$ is not available as a continuous function but as a set of discrete points as noted on reference 112, computational power is required for proper interpretation of the data, the example given in that work involves the deconvolution of matrices of 120*120.

Other methods have been introduced for calculation of tip-sample forces from the experimental data, most notably the method of Sader and Jarvis[113, 114].

As mentioned in the first paragraph of section 2, all the data presented in this work was acquired with a machine that combines nc-AFM and STM, and allows the simultaneous recording of Δf and tunneling current. The measured tunneling current is the time-average of one oscillation cycle. Because the magnitude of the average tunneling current increases with small amplitudes, the use of small amplitudes reduces the noise in the combined measurements[106, 115].

2.3.2 AFM Tips and qPlus Sensors

Miniature quartz tuning forks are employed in electronic and watch industries, these force sensors present several advantages[79-81, 116] with respect to conventional force sensors:

- Piezoelectric readout of the prongs oscillation amplitude.
- Higher quality factor *Q*.
- Higher stiffness which avoids jumping to contact.
- Thermal stability.

It is hard to quantitatively obtain the tip-sample force gradient from the resonance Δf. The reason for that is that the formalism developed for conventional cantilevers is not strictly valid for tuning forks as the symmetry of the beams is broken when a tip is mounted onto one of them[79, 83]. This asymmetry can be compensated by mounting a counterweight or in this particular setting, by gluing the free beam to a support, it is this configuration that is known as *qPlus,* and Q does not drop[116-118]. The complex challenges that had to be overcome to distinguish noise and signals detected by qPlus sensors are explained in detail in reference 116, these will not be explored in this text.

By applying an AC voltage to a piezoelectric actuator the tuning fork is excited mechanically, the single crystal quartz is a piezoelectric material, the detection of the bending oscillation of the prong of the tuning fork is performed electrically using piezoelectric effect.

2.4 The Experimental Setup

This thesis relies on an existing experimental setup that is described in detail by Felix Bischoff[119], who was a member of the team that put it in operation. Accordingly, the description here focus, only on the most relevant technical aspects.

2.4.1 The Apparatus

Consisting of a stainless steel vessel manufactured by VAb GmbH[120], it is separated into two chambers, one housing a commercial LT-STM/AFM by CreaTec[121], with which data was collected (further referenced as AFM chamber) and the preparation chamber, both are separated by a gate valve. The vessel itself is mounted on an aluminum frame suspended on 4 pneumatic dampers[122] that isolate it from ground vibrations.

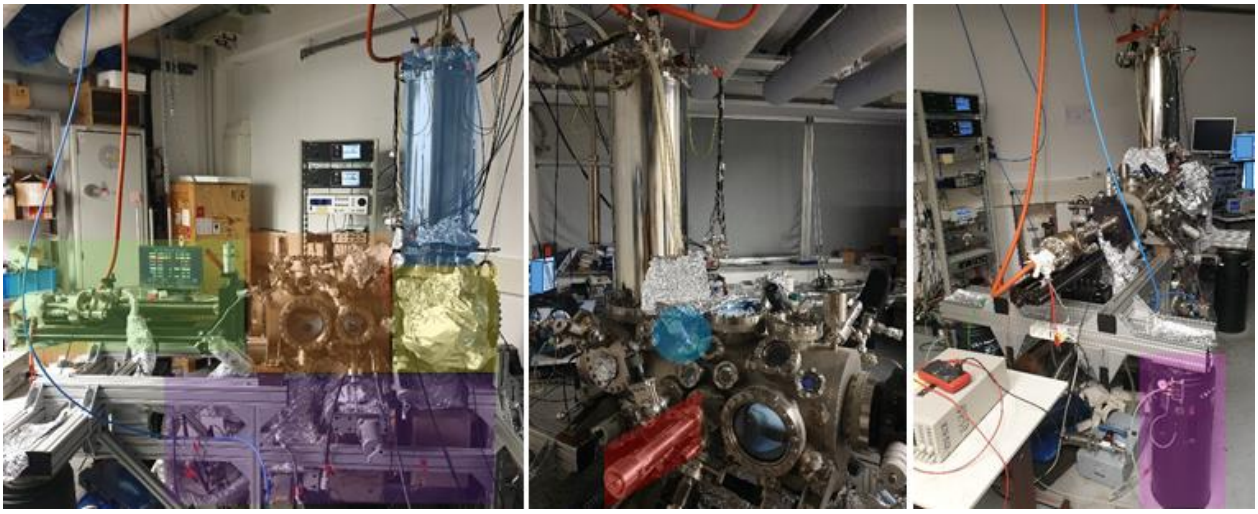

Figure 2.4 STM/AFM microscope. In the left image, indicated by different colors are the next sections: green-manipulator, orange-preparation chamber, purple-vacuum pumps, yellow-SPM chamber, blue-cryostat. In the middle image, indicated in red is the outer magnet that moves the sample parking lot, in blue the outer section of a custom made shutter. In the right image indicated in violet is one of the 4 pneumatic dampers.

There are multiple reasons for the separation of the two main chambers, the AFM chamber hosts a cryostat in which the probe is located, the cryostat itself consists of two reservoirs, one filled with liquid nitrogen (77 K, LN_2) and another filled with liquid helium (4.2 K, LHe). At these temperatures the various gases and molecules used in the preparation chamber would contaminate the walls to which they would stick. During the sample transfer the temperature increase would induce desorption and unwanted contamination of the sample. The vacuum of this chamber is maintained by an ion pump[123] (for an explanation see below) and the previously mentioned cold walls of the cryostat which serves as a permanent cold trap. Relevant to the operation of the ion pump is that over time, gases and other molecules stick to the walls of the cryostat and the increase

of temperature of its walls during transfers leads to desorption of said molecules which can contaminate the prepared samples and may harm the ion pump.

The preparation chamber consists of:

- Manipulator with which samples are held and moved between the chambers.
- "Parking lot" in which mounted crystals that are not being used can be stored in UHV conditions.
- Three types of pumps
    - Ion getter pump or simply ion pump. Consists of an array of parallel steel tubes in between two titanium plates that are close to the steel tube´s open ends. The working principle relies on the ionization of the gas particles that remain in the chamber that hit the titanium plates. The impact releases Ti atoms which cover the surfaces of the ion pump and react with the ionized particles.
    - Turbo-molecular pump (TMP)[124], diaphragm pump (DP)[123] and rough pump. These three are mechanical pumps, worth noting is that the vibrations can be transmitted to the probe and act as a source of noise.
    - Titanium sublimation pump (TSP). Consists of resistively heated Ti filaments from which Ti atoms sublimates and covers the surrounding walls. Due to the chemical reactivity of Ti the gas particles react upon contact and are removed from the volume.
- Sputter gun[125]. Used to prepare atomically clean sample surfaces by ionizing argon atoms and the Ar^+ ions are then accelerated into the sample.
- Loadlock. Used to transfer samples from the laboratory into the preparation chamber.
- Mass spectrometer[126]. Used for gas analysis, leak detection and measurement of the composition of the various substances utilized.

2.4.2 The Ultra High Vacuum System (UHV)

As previously indicated in the first paragraph of section 2 the acquisition of data was carried out at pressures of ~$1*10^{-10}$ mbar, the preparation of samples involved different conditions explained further in their respective sections.

To create the vacuum the machine is heated up to 393 K (120 °C) in a process known as *bake out.* For this, the machine is sealed and the mechanical pumps start running. The outer walls of the machine are covered first with heating tapes and the temperature of the section that each covers is measured with thermocouples, the machine is then covered with aluminum foil or a baking tent. A temperature controller reads the temperature and automatically turns of the heating tapes to ensure that the temperature does not increase further, the reasoning being that sensitive parts, such as the piezo electronic devices with which the probe is manipulated can be damaged if a higher temperature is reached. After 72-96 hours the internal pressure should reach at least a minimum of $9*10-^{8}$mbar, and it is then that the heating process stops, and all filaments are degassed while the walls are still warm.

2.4.3 Sample Preparation

In this work Ag(100) and Au(111) single crystals were employed as samples. A sample consists of a base (figure 2.5) in which an electrically heated oven is clamped. Temperature is controlled manually by adjusting current/bias. The temperature is read via thermocouple. The base is thermally and electrically insulated from the oven with sapphires that clasp and keep it in place. Wires are insulated by ceramics.

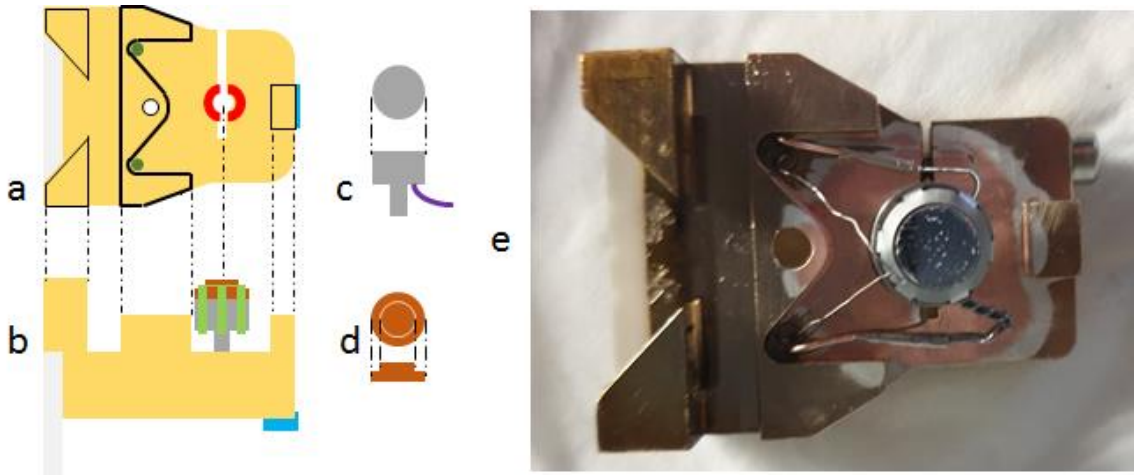

Figure 2.5 Representation of an assembled sample. a) Upper view of a sample holder without the oven, represented in red are the sapphires used to fix in place the oven, in dark green are the ceramics through which the oven and thermocouple are connected to the contact plate marked in grey. b) lateral view of a sample holder with mounted oven. In green can be observed the molybdenum star used to fix the crystal to the oven. c) and d) same perspectives of oven and crystal, respectively. e) picture of an assembled sample, omitted from the schematic drawing are the wirings that here can be observed.

For the surface of a sample to be in quality that can be scanned the undesired impurities must be removed. This is achieved by employing fast ions impacting the surface and ejecting atoms/particles from the exposed surface, this includes layers of the metal sample[127, 128]. Optimized values for sputtering Ag and Au can be found in documents from the provider[125, 129, 130]. Once the sputtering time is over, the sample is annealed to the desired temperature, always making sure to not reach the melting temperature. For a sample that was exposed to the atmosphere and has since not been cleaned, our typical procedure is as follows, the first 4 cycles of sputtering last 40-45 min as a minimum, with an Ar pressure of $1\text{-}2*10^{-5}$ mbar, followed by annealing cycles with temperature increments of 50 K (50 °C) starting at 373 K (100 °C) and lasting until the pressure stabilizes. Subsequent sputtering cycles can be reduced to 20 minutes, annealing temperatures with the same increments are applied until reaching 823 K (550 °C) for Ag(100) and 923 K (650 °C) for Au(111). The quality of the surface needs to be checked before attempting any experiments (blank preparation), once it is ensured that the crystal is in working conditions, and by extension the preparation chamber, the sample is ready for deposition of the organic molecules that are to be analyzed. Further use of the sample can be done with several sputtering/annealing cycles similar to the final step described here.

For the deposition of organic molecules an organic molecular beam evaporator (OMBE) was used. To ensure the cleanliness of the OMBE and crucible as well as the functionality, the empty crucibles are placed in the available slots, a blank is used to close the end and a baking procedure is performed normally for all the OMBE at 423 K, but the head of the evaporator at the maximum temperature of operation (723 K), all for 15 min ensuring that all the potential minor remains of the organic material are desorbed or graphitized. Once this step has been performed the crucibles can be filled with the organic material (2H-P, Zn-P and DBQP). For the OMBE to be introduced in the preparation chamber a bake out with the organic molecules needs to be performed at 423 K overnight (12 hours minimum). The temperature of the bake out may be lowered if necessary, this will depend on the reported temperatures for the melting point, evaporation or sublimation. Once the OMBE is open to the chamber and closed to the pumping station the molecules may be degassed, with temperature increments that may not reach the temperature of deposition and letting the pressure in the chamber decrease to $1*10^{-9}$mbar or stabilize.

Chapter 3 Porphine Tetramers on Ag(100)

The focus of this chapter is the synthesis of a surface-anchored square-like porphyrin tetramer with a COT moiety, based on temperature-induced dehydrogenative homocoupling of porphine precursors on Ag(100). Both free-base (8H-P) and Zn-functionalized (4Zn-P) tetramers could be achieved, coexisting with other oligomers. Despite the yield and selectivity being low, it opens up the opportunity to comprehensively characterize such intriguing tetramers by STM and bond-resolved AFM, complemented by DFT calculations. A collaboration established with the group of Pavel Jelinek from the Institute of Physics of the Czech Academy of Sciences who provided us with DFT calculations. All DFT calculations included in this thesis were performed in gas phase or on substrate as indicated in the text. AFM simulations were performed with a CO tip with a charge of q = -1[131-133].

3.1 Introduction

The concepts of aromaticity and antiaromaticity are currently defined by the IUPAC by means of chemical stability and the stabilization and destabilization of transition states of pericyclic reactions[134]. The chemistry of aromatic molecules is widely known and the concept itself applied to predict the outcome of reactions. Much less is known of antiaromatic molecules, usually due to these compounds being too unstable to be isolated under common laboratory conditions or the molecule adopting a stable configuration, forgoing antiaromaticity[135-137]. If molecules with antiaromatic character exist, they are usually stabilized by steric effects of various classes of substituents[138-145]. For example, the antiaromatic form of COT has been studied solely on molecules in which the substituents force the planarity[146-148].

Porphyrin macrocycles consist of four pyrroles united through the α-positions by four methine bridges, as marked in figure 3.1a. Available for chemical reactions are the C atoms at the β and *meso* positions for external peripheral functionalization, and the N atoms at the core, for which abundant literature exists. Of relevance to this chapter is the literature that covers the topics of aromaticity/antiaromaticity and on-surface reactions. The degenerate tautomerism of free-base porphine (2H-P) (considered as such since there are twelve tautomeric states of which only two are inequivalent) has been investigated in detail, and it has been determined that the H transfer occur in a 90° fashion, that is the H transfer occurs from one adjacent N atom to the other but not from

opposite positions. The free-base *trans* and *cis* structures are depicted in figures 3.1b and 3.1c respectively. The aromatic pathway of 18π e^- is defined by the position of the inner H[24, 149, 150]. The aromatic pathway and bond order of metalated porphyrins is a topic that is still investigated, but so far different approaches have led to similar conclusions, that the different delocalization pathways, such as those of figures 3.1e-g contribute to the overall aromaticity of the macrocycle[151-155].

It is relevant to remind the reader that at the time of writing there are no direct means to determine aromaticity, and even though NMR is accepted, doubts are cast on the reliability or the manner in which aromaticity takes place[156-158], or as Bröring would put it, there is a "*confrontation of philosophies*"[159]. Alongside NMR, other ways in which aromaticity and bond alternation are measured is by analyzing the products of chemical reactions. Computational efforts to understand aromaticity include concepts such as nucleus independent chemical shifts (NICS)[160], anisotropy of the induced current density (ACID)[161], and harmonic oscillator model of aromaticity (HOMA)[162].

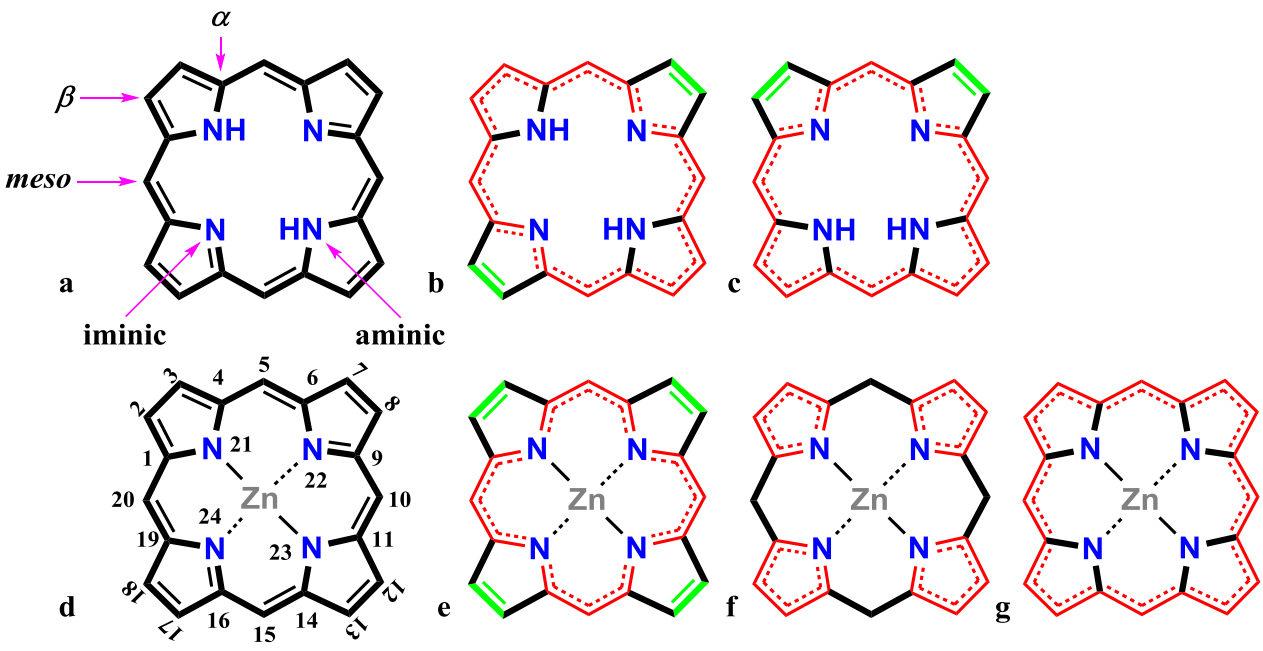

Figure 3.1 Monomer structures, and aromatic pathways of free-base porphine (2H-P) and zinc porphine (Zn-P). Marked in red can be found the agreed electron delocalization pathway in the respective macrocycles, in green are marked the olefinic *β-β* bonds. a) 2H-P with the three types of C atoms and the two types of N atoms are marked. b-c) *trans* and *cis* tautomers, respectively, of 2H-P. d) Zinc metalated porphine with the numbered positions.[163] e-g) theorized delocalization pathway of metalated porphines.

Porphyrin chemistry provides access to polyporphyrin systems forming COT moieties. These include biscorroles[141] and tetrameric porphyrin sheets[142]. In NMR analysis, the latter have shown a unique downfield shift assigned to a paratropic current near the COT moiety, and the former has two oxidation states, one of which is NMR silent.

In a pioneering study by the Osuka group[142], tetrameric porphyrin units were deposited by a pulse injection method on a Cu(100) support in UHV, followed by STM imaging. The STM appearance was determined by the bulky *meso*-di-*tert*-butylphenyl substituents. Despite porphyrins and related compounds being heavily employed in studies at interfaces, favored due to their functionalities and chemical versatility[164, 165] we are not aware of any other report on surface-anchored square-like porphyrin tetramers. In general, the intact deposition poses a severe challenge for extended oligomers, e.g., due to limited stability or solubility, and thus represents a bottleneck for successful characterization by surface science techniques, such as STM and AFM. Specifically, when employing low-temperature and functionalized tips, the latter method can provide bond-resolution in surface-anchored organic molecules and architectures and thus represents a most powerful tool to comprehensively characterize porphyrin compounds.

3.2 On-Surface Porphine Homocoupling

In scheme 3.1, highlighted in blue are the bonds that form the internal COT, comprised by intraporphyrin (pyrrole) and interporphyrin *β-β* bonds. In green can be observed the *meso-meso β-β* bonds of triply fused oligomers closing the rings of the naphthalene moiety. Irrespective of the substitution at the core of each porphine subunit, we can divide the pyrrole rings by their relative positions, and the naphthalene moiety formed between the triply fused subunits can also be subdivided, this will be referenced further.

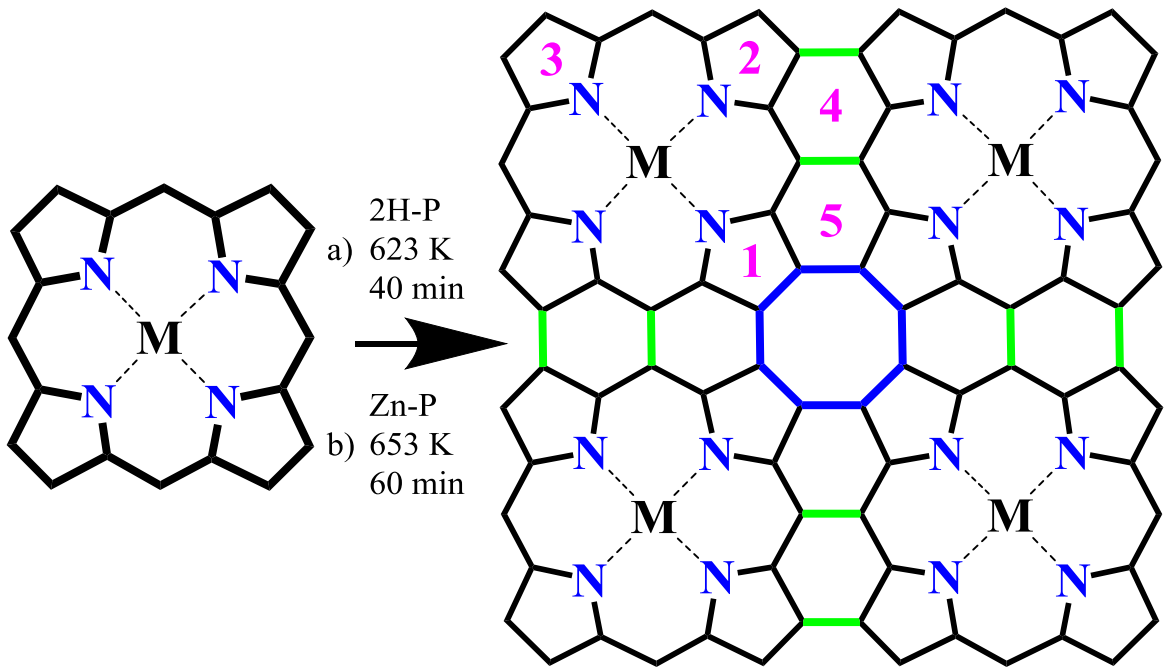

Scheme 3.1 On-surface synthesis of 8H-P and 4Zn-P tetramers on Ag(100) from 2H-P and Zn-P precursors. a) Typical annealing parameters for the 2H-P case. b) Annealing procedure for Zn-P. The central COT moiety of the Por tetramer is highlighted in blue, additional *meso-meso, β-β* links in green. Distinct rings are numbered (see text for discussion).

Coinage metal substrates provide a convenient platform for the synthesis of extended covalently bonded organic structures[166] (see also Chapter Introduction). In particular the successful formation of porphine dimers and larger oligomers by dehydrogenative homocoupling of 2H-P has been observed on Ag(111)[33] and Au(111)[63] substrates. Importantly the head-on coupling – which is required for the formation of the regular tetramer structure (scheme 3.1) – has been successfully induced with relatively high yields on Ag(111)[33]. Inspired by these experiments, we extended our synthesis endeavor to a Ag(100) support, which provides a fourfold symmetry, modifying the protocol. Aiming for the formation of 8H-P tetramers, about two monolayers (ML) of 2H-P were deposited at *rt* followed by annealing at 623 K for 40 min, inducing the coupling and desorption of unreacted 2H-P monomers. For Zn-P tetramers, once two ML of Zn-P were obtained, the sample was annealed at 653 K for 60 minutes, with continuous supply of Zn-P for the first 20 minutes to counter the depletion of reactants due to desorption.

Figure 3.2a shows an STM image after applying this procedure for 2H-P, revealing the coexistence of several oligomers with distinct structures. Dimers are the main product, with a lower number of oligomers of higher mass, such as "L-shaped" trimers occurring. Importantly, the image shows a square-like unit that will be identified as 8H-P tetramer. Most porphine subunits reveal a central

depression, attributed to the free-base macrocycle core and only few oligomers include bright centers assigned to temperature-induced self-metalation with Ag, consistent with reports on Ag(111)[33]. The center-to-center distance within straight dimers amounts to 8.5±0.2 Å, thus matching values reported for *β-β, meso-meso, β-β* triply linked oligomers on Ag(111)[33] and in solution (8.45 Å)[167]. The same distance is observed within the tetramer, thus indicating successful covalent homocoupling. Indeed, bond-resolved AFM imaging (figure 3.2b) undoubtedly confirms C–C bond formation and helps to unambiguously identify the bonding motifs of oligomers observed in figure 3.2a.

Whereas intramolecular resolution was reported for dimers on Ag(111)[168], and tapes of disubstituted porphyrins on Au(111)[71], the bond-resolved imaging of oligomers with two-dimensional extension is unprecedented. The AFM data confirm a parallel alignment of the oligomer macrocycles with the surface and a rather planar adsorption configuration, without indications of a displacement of N atoms towards the surface or other out-of-plane distortions. Minor variations in the AFM contrast and appearance of the porphyrin cores are attributed to the adsorption geometry and to the central atoms (hydrogens vs. Ag)[168]. Structural details of the 8H-P (and 4Zn-P) tetramers will be discussed in the respective paragraphs (vide infra). The regular oligomers, such as the straight dimers and tetramers, are only observed in distinct orientations on the Ag(100) lattice, signaling the influence of molecule-substrate interactions. For example, the longitudinal axis of the dimers deviates by ±20° from the dense-packed high symmetry directions of Ag(111) (free-base: ±20±2°, Zn: ±18±2°) , whereas alignment angles of ±30±2° and 17±2° are observed for the 8H-P and 4Zn-P tetramers (figure 3.2a).

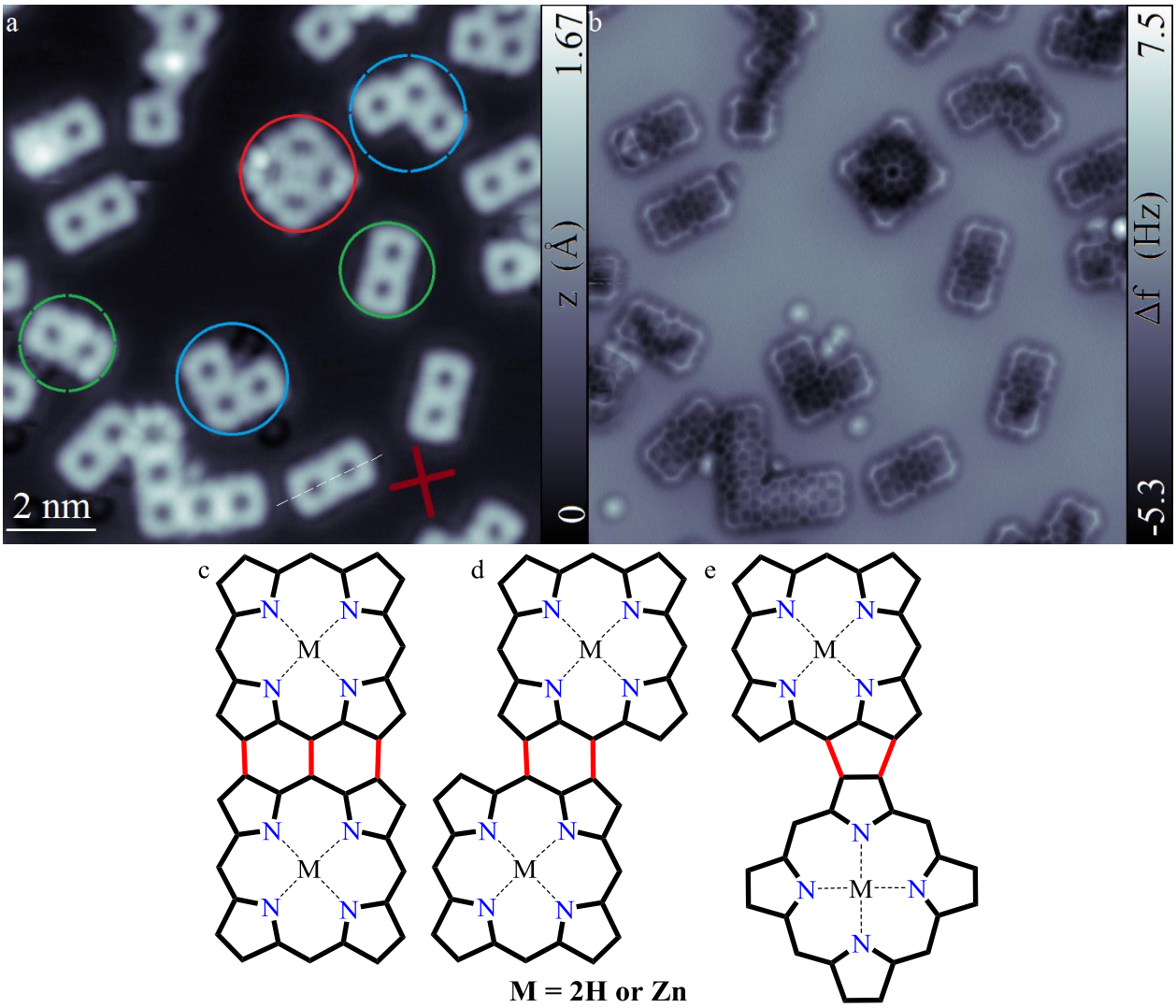

Figure 3.2 Porphine homocoupling on Ag(100), product overview and bonding motifs. a) STM image after annealing 2H-P at 623 K (50 mV, 12 pA). b) corresponding bond-resolved nc-AFM image, revealing the structure of the oligomers. Colored circles in a) highlight tetramer (red), trimer (blue), and dimer (green), comprising triply fused porphines. Less symmetric motifs are marked by dashed circles. The red cross reflects the dense-packed Ag(100) directions, the white dashed line the longitudinal axis of a dimer. The round protrusions in b) are assigned to CO molecules. c) Triple linkage *β-β*, *meso-meso*, *β-β*. d) Double linkage *meso-β*, *meso-β*. e). Double linkage *β-meso*, *β-β*. Newly formed bonds marked in red.

Our data provide no indication for an organometallic intermediate (C–Ag–C) in the coupling of the porphyrin macrocycles and thus contrast reports on Cu(111)[169] and Cu(110)[66, 68] describing an organometallic (C–Cu–C) stage, which may not transition to a C-C bond. Furthermore, no peripheral dehydrogenation is discernible in the observed reaction products.

The yield of porphine tetramers is very low (estimated to be below 1% considering the number of reactants in a dense-packed porphine bilayer). Two reaction paths can be devised for the synthesis

of the porhin tetramers, one of them being the sequential addition of monomers via formation of *β-β, meso-meso, β-β* bonds, that is, the progression from a straight dimer, to an "L-shaped" trimer, and finally to a tetramer. The alternative pathway involves the addition of two straight dimers fusing laterally. For the first to be possible, once a trimer is formed, a monomer would need to approach and perfectly integrate into the trimer's opening, cleaving a total of twelve C–H bonds (simultaneously or in a series of steps). A staggered configuration with a monomer located in the trimer's opening, but only featuring *meso–β*, *meso–β* links was observed in the experiments ("failed tetramer", not shown) and might be considered as a reaction intermediate. However, for the monomer to translate to the final position, two C–C bonds (and eight C–H bonds) should break, which may prove to not be feasible at the reaction temperature. Alternatively, the initial formation of a single *β-β* bond (e.g., discussed in ref. 63) might be followed by rotation of the monomer, aligning it for tetramer formation. Without conclusive experimental or theoretical insight, it can only be speculated what the possible mechanisms can be, such as out-of-plane movements, an initial cleavage of *β*-C–H bonds (less labile than *meso*-C-H bonds[33]), and the consideration of entropic contributions of the released hydrogen[63]. The intricate paths make the low reaction yield understandable. Worth noting is that not a single structure was found in which a porphine is fused solely to the *β*-C in the bay area of an oligomers (defined by four adjacent *β* carbons at the periphery)[170].

3.3 Zinc Metalated Porphyrin Tetramers (4Zn-P)

Figure 3.3a shows a high-resolution AFM image of a 4Zn-P tetramer, synthesized on Ag(100) by the procedure described above. As discussed when addressing the large-scale image of the 2H-P derived oligomers (figure 3.2), the molecular plane is aligned coplanar with the Ag(100) surface. The AFM data unravel details of the molecular structure. The center-to-center distance of 8.5±0.2 Å matches the values introduced above for *β-β, meso-meso, β-β* coupled dimers and 8H-P tetramers, with these bonds being clearly discernible. The central COT ring is resolved and encloses an area with the lowest Δ*f* values (i.e., dark contrast). On contrary, the molecular periphery and specifically the four *β-β* bonds representing the tetramer's corners show high Δf values (i.e., bright contrast). Nonetheless, the modest Δf variation across the tetramer signals a rather planar molecular conformation. On first sight, the 4Zn-P tetramer appears four-fold symmetric (i.e., D_{4h}) in the AFM

data. However, a close inspection of figure 3.3a reveals subtle differences in the eight bonds that "radiate out" of the COT moiety, reducing the symmetry. Specifically, adjacent intraporphine bonds at the *α-β* positions (ring 1, compare numbering in scheme 3.1) show bright and dark contrast, respectively (see blue and red arrow in figure 3.3a). We attribute this effect, which introduces chirality (compare figure 3.4), to the adsorption registry of the tetramer on the Ag(100) lattice. As shown in figure 3.4, the four "dim" bonds are positioned above Ag atoms, whereas the "bright" bonds are located above bridge positions (red and blue arrows). To determine the registry and orientation of the 4Zn-P tetramer on the Ag(100) atomic lattice we imaged the free Ag surface that is contiguous to the target molecule. The process involves changing the height of the tip, once the image of the substrate has been imaged the tip is retracted 0.28 nm. It is important to prevent the tip from approaching the molecule laterally to safeguard the integrity of both molecule and tip.

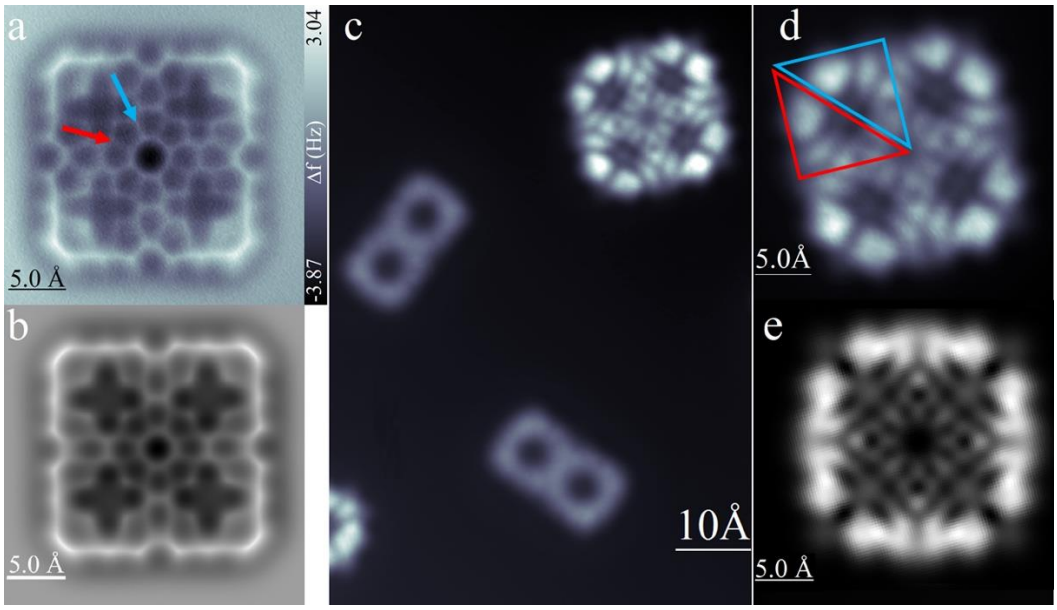

Figure 3.3 4Zn-P tetramer. Experimental and simulated AFM and dI/dV maps of a Zn-P tetramer. a) Constant height nc-AFM measurement of a square Zn-P tetramer. b) Simulated AFM images of the corresponding Zn-P porphine tetramer on Ag(100). c) Experimental dI/dV map of a tetramer and two dimers (50 mV). d) Zoom-in of Zn-P tetramer dI/dV map (50mV). e) Simulated dI/dV map of the 4Zn-P tetramer.

Figure 3.3b shows a simulated AFM image of a 4Zn-P tetramer on a Ag(100) slab, based on a DFT-optimized structure. The simulation reproduces the key characteristics of the experimental image and provides additional insights. For example, the simulations reflect the apparent elongations of the bonds of the benzenoid rings 4, as well as in the pyrroles 2 and 3 (see scheme 3.1), in which the bonds of the outer *meso*-C and *α*-C appear rather blurry (precluding a reliable determination of bond lengths). Also, the alternating intensity of the radial bonds discussed above

is reflected in the simulation. Similar to the experimental results, the corner pyrroles (rings 3) appear brighter than pyrroles 2, even though the structural model does not show a relevant height difference or tilting. These differences are attributed to an effect of the force field, as demonstrated for other antiaromatic molecules[171, 172]. The structural model reveals that the eight C atoms constituting the COT are closest to the Ag surface.

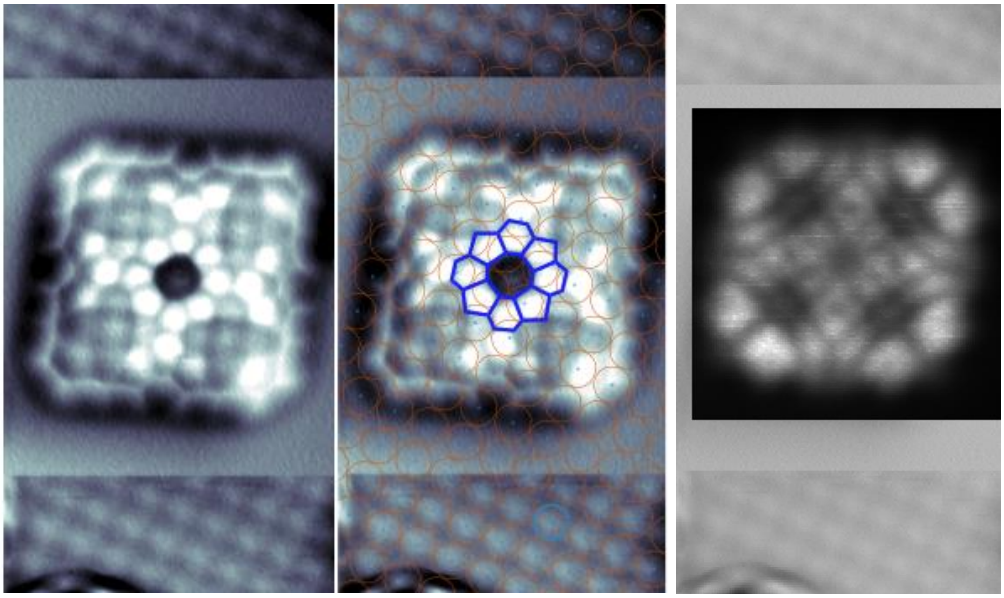

Figure 3.4 4Zn-P tetramer adsorption registry on the Ag(100) atomic lattice. During scanning, the tip height was adapted to resolve the Ag(100) lattice (top and bottom part of the image) and to scan the tetramer without displacement (middle part). The overlay in the middle panel highlights the registry of the COT-constituting rings (in blue) on the Ag(100) atomic lattice (orange circles). The panel to the right is an overlay of a dI/dV map of the same structure (50 mV).

To obtain information on the electronic structure of the 4Zn-P tetramer, constant height d*I*/d*V* mapping at different bias voltages was performed, further complemented by theoretical modeling. Figure 3.3c shows such a d*I*/d*V* map of an Ag terrace hosting a 4Zn-P tetramer and two dimers. The pronounced sub-molecular contrast reveals a distinct pattern for the 4Zn-P tetramer, signaling contributions of molecular electronic states. In contrast, a different and more subtle contrast variation is evident for the dimers, immediately pointing to distinct differences in the electronic structure of tetramers and dimers. Figure 3.3d shows a d*I*/d*V* map of a 4Zn-P tetramer recorded at 50 mV. It reflects the same well-defined pattern, which persists in a very large bias voltage range from -700 mV to 350 mV (see figure A1). It is characterized by a central ring composed of eight intensity maxima and two "L-shaped" protrusions separated by one node at each corner of the tetramer. Similar to the observation in the AFM image, a subtle symmetry reduction can be observed in the d*I*/d*V* maps, which introduces chirality to the electronic structure. The apparent

brightness of one of the "L-shaped" protrusion at each corner exceeds the one of its neighbor, as highlighted by the blue and red triangles in figure 3.3d. The contrast variations in the d*I*/d*V* maps thus reflect the variation of bonds in the AFM data, the "brighter" protrusions occur in the segment of the molecule with "brighter" *α-β* bonds. "Electronic chirality" was reported before in structurally achiral molecules such as phthalocyanines adsorbed on Ag(100) and Cu(100) and attributed to asymmetric charge transfer between molecule and substrate[173, 174], with effects on the molecular functionality[175, 176].

To rationalize the experimental observations on the 4Zn-P tetramer's low-energy electronic structure (i.e., electronic contributions of occupied and empty states near the Fermi level E_F), DFT calculations were performed. Specifically, the origin of the characteristic pattern in the dI/dV maps is addressed. The key features of the experimental dI/dV map can be reproduced when considering the density of states of the degenerated lowest unoccupied molecular orbital LUMO+2 and LUMO+3 in gas phase (see figure 3.3e). For a rationalization of why these orbitals describe the experimental dI/dV close to E_F, we refer the reader to the next section about 8H-P.

3.4 Free-Base Porphyrin Tetramers (8H-P)

Figure 3.6f shows a high-resolution AFM image of an 8H-P tetramer, synthesized on Ag(100) by the procedure described in section 3.2. Most intramolecular bonds are clearly resolved, confirming the successful formation of the highly symmetric tetramer skeleton structure (see scheme 3.1). There are similarities with the metalated 4Zn-P tetramer: i) the corner pyrroles (rings 3) are imaged brighter than the adjacent pyrroles (rings 2), specifically at the N positions. ii) The bonds to the peripheral *meso* carbon atoms appear blurry, precluding a reliable bond length (bond order) analysis. iii) An elongation of bonds in rings 2, 3 and 4 is observed. iv) The bonds of rings 1 and 5, which comprise the COT, alternate in their Δf contrast. Compared to the 4Zn-P tetramer data (figure 3.3a), the AFM images of 8H-P tetramers reveal more pronounced Δf contrast variations across the molecule. Three concentric ring-like areas are discernible, marked by three colored dashed quarter circles in figure 3.6f. The outer (pink) and inner (yellow) areas, constituted by rings 3 and 1, 5, respectively, show bright Δf contrast. The intermediate area (orange), covering the macrocycle centers and rings 2, 4, shows a significantly dimmer Δf contrast. This feature, characteristic for the 8H-P tetramer, reflects the symmetry reduction in each porphine subunit

induced by the position of the hydrogens and the presence of iminic (–N=) and aminic (–NH–) pyrrole rings, as discussed below.

A typical d*I*/d*V* map recorded on an 8H-P tetramer is shown in figure 3.6i. It closely resembles the data achieved for 4Zn-P tetramers (compare figure 3.3d). Eight intensity maxima on a central ring and two "L-shaped" protrusions separated by one node at each corner are observed. The pattern persists in a large bias voltage range from -250 to 50 mV (figure A2). The two protrusions at the corners show different Δf contrast, inducing chirality and mirroring the differences in the *α-β* bonds. Such asymmetries are also observed in 4H-P dimers (figure A2).

We note that bias voltage pulses can induce irreversible modifications of the tetramers, recognizable by a broad depression at the porphine cores in AFM images (figure A3). This effect is tentatively attributed to a loss of central hydrogen. Furthermore, scanning at perturbative conditions can promote a translation and rotation of 8H-P tetramer on the Ag(100) lattice, confirming the rigidity and stability of the on-surface synthesized oligomer (figure 3.5).

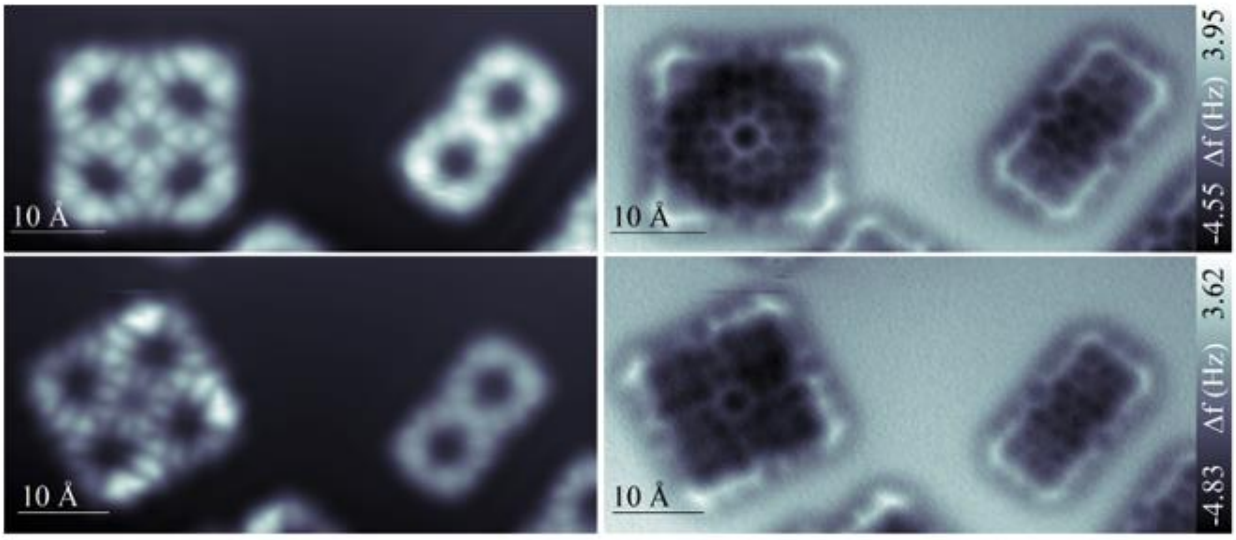

Figure 3.5. STM-induced manipulation affording lateral displacement and rotation of tetramer units. The top left panel shows a dI/dV map image before manipulation. The bottom left panel shows a dI/dV map after manipulation. The corresponding nc-AFM images are found to the right. The data demonstrate the robustness of the on-surface synthesized tetramers. The modifications discernible in the dI/dV maps are tentatively assigned to the change in the surface registry upon manipulation, affecting molecule - substrate interactions.

To rationalize the experimental observations on the 8H-P tetramer, it is necessary to acknowledge the complexity induced by specific tautomer configurations, which might differ between the porphine subunits. For free-base porphine monomers on Ag supports, only one tautomer configuration could be identified in low-temperature STM experiments, namely that in which the inner H atoms occupy N positions 21 and 23, which also allowed for current induced tautomerization[177, 178]. With no indication of dehydrogenation of the macrocycle centers, an 8H-P tetramer thus might occur in 16 possible tautomeric states (excluding *cis* tautomers of each monomer, figure A4) that can be reduced to six inequivalent configurations as is explained for the 2H-P monomer in section 3.1. However, only two tautomer configurations are consistent with the highly symmetric appearance of the 8H-P tetramer in both bond-resolved AFM data and d*I*/d*V* maps, namely configurations $T_{\times}$ and $T_{\diamond}$, sketched in figure 3.6a and b, respectively. For both structures, the red ellipses highlight the orientation of the inner hydrogen pair in each porphine subunit. In solution at *rt*, a functionalized 8H-P tetramer has been identified to occur as a single tautomer, corresponding to model $T_{\times}$[142]. Note that temperature might affect the tautomeric state, as exemplified by 22-hydroxybenziporphyrin that has two tautomers, one aromatic and another antiaromatic, with the latter being favored at low temperature (183 K)[179].

The direct identification of the tautomeric state from scanning probe microscopy (performed at 5 K) is not straightforward. In high resolution STM images of porphine monomers and dimers on Ag(111), the orientation of the hydrogen pairs was deduced from intensity variations in the macrocycle.[177, 178] However, the STM data on the 8H-P tetramer on Ag(100) do not allow for such an assignment (compare figure 3.2a). In br-AFM imaging, the situation is even more intricate. There is only one experimental study in which the orientation of the hydrogen pair in a monomer (2H-naphthalocyanine/NaCl/Cu(111)) could be deduced from the Δf contrast, by considering large tip-sample distances[96]. In the current system, this approach was not conclusive. Furthermore, it was shown for porphine dimers on Ag(111) that the adsorption registry can modify the Δf appearance of the molecular cores, that might appear as "bright" or "dark" crosses[168]. Indeed, as described above, figure 3.2b reveals subtle differences in the appearance of macrocycle centers. As the tautomer configuration dictates the electron delocalization pathways, one might consider to perform a bond-order analysis (based on measuring bond lengths and appearance[180]) to discriminate between $T_{\times}$ and $T_{\diamond}$. However, the "blurry" appearance of peripheral bonds and distortions due to electrostatic effects (vide infra) prevent an unambiguous identification.

Nonetheless, high resolution AFM images might contain information on the orientation of the hydrogen pairs. For example, some porphine dimers reveal "dark" diagonals in each subunit that align to form a "V-like" depression, spanning the dimer (see figure 3.2b and figure A5). These areas of contrast correspond to the two types of pyrroles and a correlation can be stablished to the electrostatic map of the dimers[171, 172]. This contrast is reminiscent of the dim Δf ring in the 8H-P tetramer, discussed above (figure 3.6f).

To clarify the tautomer configuration and to better understand the electronic structure of the 8H-P tetramer, we resort to DFT calculations. AFM images and d*I*/d*V* maps were simulated for models $T_{\times}$ and $T_{\diamond}$ and compared to the experimental data. Whereas the simulated AFM images based on model $T_{\times}$ (figure 3.6e) and model $T_{\diamond}$ (figure 3.6g) both reflect the tetramer skeleton and key features of the experimental image, relevant differences are discernible. The simulated image based on tautomer configuration $T_{\diamond}$ shows a dark contrast for rings 2 and a bright contrast for rings 3 and 1, nicely reflecting the experimental observations. In contrast, the simulation for configuration $T_{\times}$ shows similar brightness for rings 2 and 3, and thus fails in describing the experimental data in the area affected by the hydrogen positions. It is worth noting that the electrostatic map of structure $T_{\times}$ (figure 3.6c) has an even appearance while the corresponding map of $T_{\diamond}$ (figure 3.6d) has areas with clear differences that are correlated to the type of pyrrole due to the internal charge of the molecule[171, 172] and would favor the identification of the tetramer tautomer as structure $T_{\diamond}$. However, regarding the imaging of the COT moiety, the simulation based on configuration $T_{\times}$ matches size and shape better. For an 8H-P tetramer in gas phase, model $T_{\times}$ is energetically favored over $T_{\diamond}$. Including the Ag(100) support, the total energies of model $T_{\times}$ and $T_{\diamond}$ are very similar, with a slight preference for model $T_{\times}$ (75 meV, PBE0).

We found a good match with the experimental dI/dV maps acquired near the Fermi level for double degenerated LUMO+2/LUMO+3 DFT orbitals. One possibility to explain this match is to consider a significant charge transfer from the substrate to the molecule filling orbitals up to LUMO+2/LUMO+3. However, the DFT total energy calculations including the surface show only negligible charge transfer and the LUMO orbital of a free-standing molecule is located at a calculated energy of -4.06 eV with respect to the vacuum level, which is higher than the workfunction of the Ag(100) surface (~4.2 eV). Thus, the scenario considering transfer of several electrons to the molecule is very unlikely. Instead, this apparent contradiction in the energy position

of the visualized frontier molecular orbital can be explained if we consider that the tunneling process into the empty orbitals induces transition from neutral (Ψ_N) to charged (Ψ_{N+1}) state. This transition $\langle\Psi_{N+1}|\hat{c}^+|\Psi_N\rangle$ can be described by the concept of Dyson orbitals[181]. Therefore, the tunneling process may introduce additional reshuffling of the order of frontiers molecular orbitals. Indeed, the calculated Dyson orbital of a free-standing molecule reflecting the addition of a single electron resembles the LUMO+1 orbital obtained from DFT calculation. A as LUMO+1 and double degenerated LUMO+2/LUMO+3 orbitals are very close in energy (~0.6eV according to the DFT calculations), we may argue that the presence of underlying metallic substrate imposes different screening[182] of those orbitals causing their swap in the energy. Consequently, the LUMO+2/LUMO+3 orbitals will be visualized in dI/dV maps at lower energy.

Overall, the experiments reveal no relevant differences in the low-energy electronic structure of 8H-P and 4Zn-P tetramers adsorbed on Ag(100), a finding consistent with the filled d^{10} configuration of Zn centers in porphyrins. The calculated dI/dV maps also show no relevant differences between the $T_\diamond$ tautomer of 8H-P and 4Zn-P, whereas the $T_\times$ tautomer is distinct. Further 4M-P complexes, achieved either by combining selected M-P precursors or by controlled metalation of 8H-P (with one or several atomic species) on the surface[183], are expected to give access to tunable electronic, magnetic and catalytic properties not achievable with monomeric units.

We currently favor the interpretation of the nc-AFM images and dI/dV maps of the 8H-P tetramers to correspond the $T_\diamond$ tautomer. The simulated nc-AFM image (figure 3.6g) better describes the concentric pattern of the experimental one (figure 3.6f). Which is consistent with the electrostatic map and follows a similar pattern for some of the found dimers as previously explained. As for the dI/dV map the experimental results do not show two areas of contrast like the simulation for $T_\times$ in which the outer rim is much brighter than the center, while the simulation of $T_\diamond$ has a more even appearance.

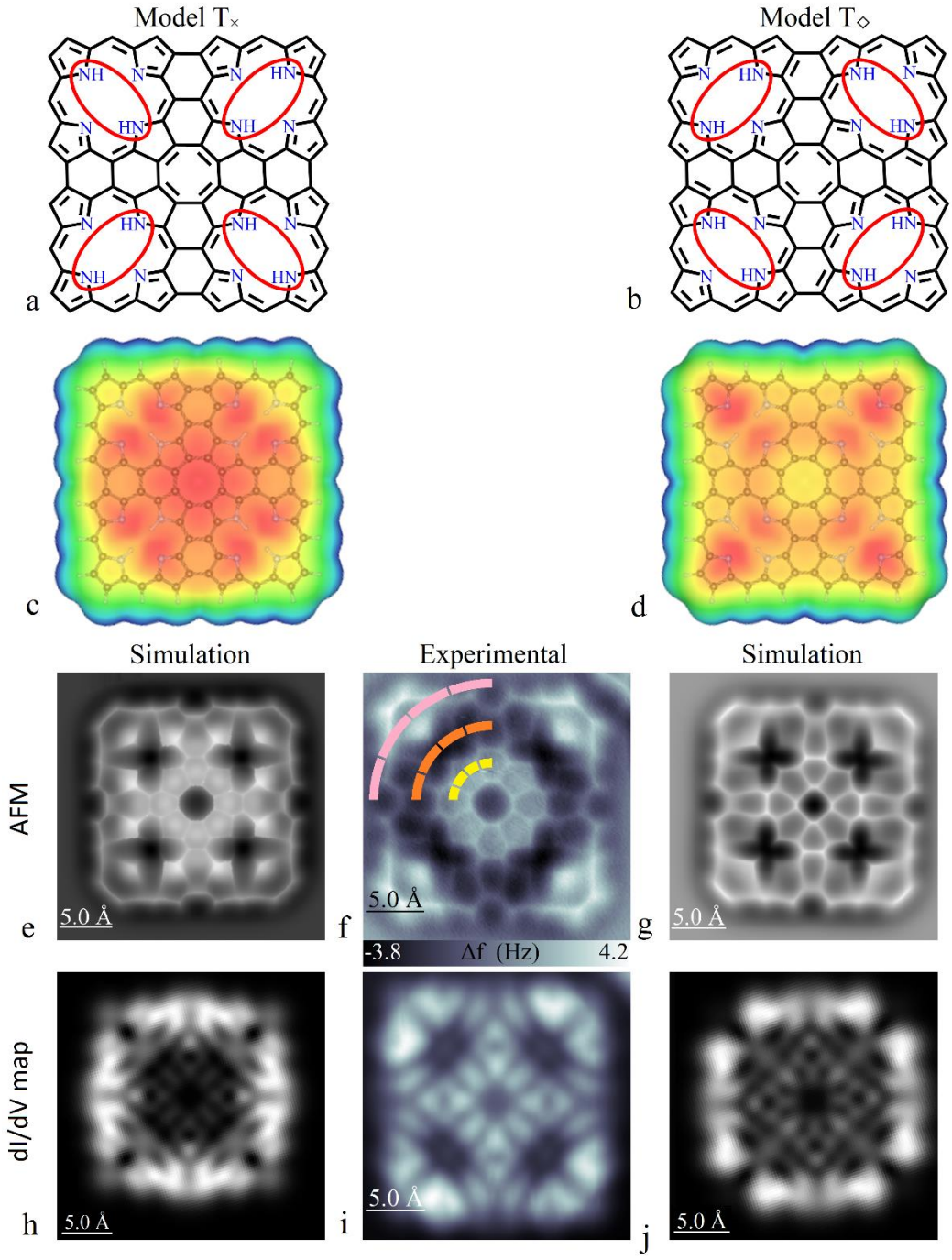

Figure 3.6 8H-P tetramer. a) and b) Respective schematic models of 8H-P tetramer in tautomer configuration $T_{\times}$ and $T_{\diamond}$. In a) and b), the red ellipses highlight the orientations of the central hydrogen pairs. c) and d) respective electrostatic maps for tautomers $T_{\times}$ and $T_{\diamond}$. e) Simulated AFM image based on structure $T_{\times}$. f) High-resolution experimental AFM image of 8H-P tetramer. The colored dashed quarter circles mark ring-like areas with distinct Δf contrast (see text for discussion). g) Simulated AFM image based on structure $T_{\diamond}$. h) Calculated *dI/dV* map for DFT orbitals LUMO+2 of tautomer $T_{\times}$. i) Experimental *dI/dV* map acquired at a bias voltage of -50 mV. j) Calculated *dI/dV* map for DFT degenerated orbitals LUMO+2 and LUMO+3 of tautomer $T_{\diamond}$.

3.5 Structural Details of the COT Moiety and Analysis of (Anti)Aromaticity

Next, we briefly address further structural details of the COT moiety and the adjacent rings. Figure 3.7a shows a high-resolution, Laplace-filtered AFM image of the central area of an 8H-P tetramer. This inner section is known in literature as tetraaza[8]circulene. Compared to the peripheral bonds, the eight rings constituting the COT show less distortions, allowing one to extract bond lengths from the AFM images. A table summarizing the relevant data is provided in the figure 3.7d. Distinct bonds are color-coded in figure 3.7a. Clearly, the data reveal a pronounced bond length alternation around the COT ring (see *β-β* bonds marked in red and white, respectively, in figure 3.7a), inducing D_{4h} symmetry with pronounced deviations from a perfect octagonal shape (D_{8h}), consistent with the structural model (figure 3.7b). Also unfunctionalized COT, adsorbed planar on Ag(100), was reported to show a four-fold symmetry in STM data[184]. More subtle variations are also discernible in the experimental AFM images (figure 3.7a). Whereas the two *α*-C–N bonds (dark/light blue) appear equivalent, the other bonds to the *α*-C show considerable differences in bond length and contrast, revealing an alternating pattern. Specifically, a long *α-β* bond (light green) goes in hand with a short *α-meso* bond (dark orange), with the opposite happening for a short *α-β* bond (dark green) and the adjacent *α-meso* bond (light orange). This effect is attributed to the adsorption configuration of the tetramers on the Ag(100) lattice, where bonds being equal for a gas phase structure sense a distinct atomic environment on the surface. This registry introduces chirality to the interfacial structure, as discussed before for 4Zn-P.

In an attempt to address the (anti)aromatic character of the 8H-P tetramer, the calculated anisotropy of the induced current density (ACID) (figure 3.6c and figure A6), was calculated for both tautomers. In the case of $T_{\times}$, the calculations show a clear antiaromatic COT center and four aromatic pyrroles in the corners (see figure A6). This conjugation character originates from the resonance structure with four Clar sextets which breaks the conjugation within each 2H-P. This can be seen also in the 2D ACID (figure A6) plots with aromatic corner pyrroles, slightly aromatic benzene rings around the COT and otherwise non-aromatic porphine units. The conjugation within the $T_{\diamond}$ tautomer exhibits a slightly different result. The COT is again antiaromatic, only now there is a seemingly aromatic periphery including 4n π-electrons (total of 60 electrons). The complete active space self-consistent field (CASSCF) calculations show that this tautomer has closed shell character in its ground state, discarding the idea of Baird aromaticity. By combining the results of ACID and bond lengths a possible explanation emerges. Figure 3.7c illustrates the final conjugation

pathway as an interference of four isolated 2H-P aromatic pathways and aromatic benzenes around the COT highlighted by green and cyan paths, respectively. Such combination causes the induced current density to appear as a global aromatic 4n periphery (blue pathway) which disobeys the known Hückel/Baird aromaticity rules and does not follow any resonance structure.

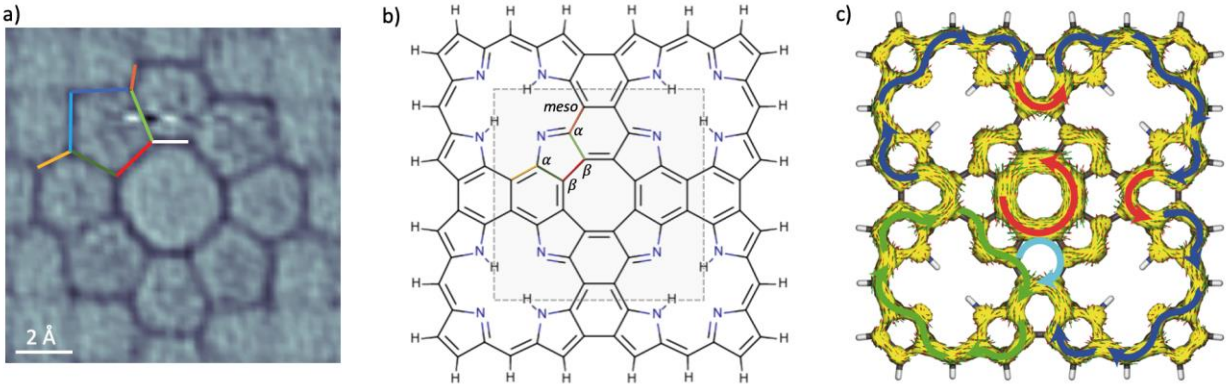

d)

	Measured bond length (Å)	
	8H-P	4Zn-P
ββ (white)	1.1	1.1
ββ (red)	1.7	1.5
αβ (low Δf, light green)	2.0	2.0
αβ (high Δf, dark green)	1.8	1.7
α-meso (dark orange)	1.1	0.9
α-meso (light orange)	1.2	1.1
α-nitrogen (dark blue)	1.9	1.7
α-nitrogen (light blue)	1.9	1.6

Figure 3.7 Structural and electronic properties. a) High-resolution AFM image (Laplace filtered) of the central area of an 8H-P tetramer including the rings forming the COT moieties. Distinct bonds are labeled by colored lines (see text for discussion). b) Chemical structure for tautomer $T_{\diamond}$ in a closed-shell configuration. The dashed gray square represents the area imaged in a). c) Plot of calculated π-ACID of $T_{\diamond}$ at isovalue of 0.05 a.u.

3.6 Conclusions

Dehydrogenative homocoupling on Ag(100) allows for the synthesis of regular two-dimensionally extended porphyrin structures, with the use of porphine precursors. Among the identified oligomeric structures are the square-type polymers that were the focus of this study. In the synthetic procedure we made use of porphines, the parent porphyrin compound that is peripherally unsubstituted, the inner core may be free-base or Zn-metalated.

The square tetramers are planar, structurally rigid as demonstrated by STM manipulation, and feature a central COT moiety. STS reveals a low-energy electronic structure that is dominated by contributions from distinct molecular orbitals, both for 8H-P and 4Zn-P tetramers, signaling that molecule-substrate interactions do not quench key molecular properties. No interfacial charge transfer occurs, based on theoretical modeling. Nonetheless, the registry to the substrate lattice induces subtle asymmetries in the apparent charge distribution and bond appearance, thus yielding a chiral adsorption structure. The accurate CASSCF calculations predict a closed-shell ground state and are a reminder that DFT-calculated orbital sequences might need to be taken with care, with electron transfer contributing in the STM measurement process. Importantly, the calculations confirm an antiaromatic COT moiety for both symmetric tautomer configurations of 8H-P, coexisting with aromatic ring currents in the porphine subunits. Thus, the square-type tetramers introduced in this work provide tectons combining aromatic and antiaromatic pathways and also highlight the challenges when applying the concept of aromaticity, developed for small monocyclic systems, to more intricate structures. The ambiguities in identifying tautomeric states are confirmed in this study, even though the combined experimental and simulated images (AFM, dI/dV) indicate that the 8H-P tetramers preferably occur in the $T_{\diamond}$ configuration at low temperature on Ag(100).

The synthetic approach can be applied to obtain tetramers with distinct metal centers, thus tailoring the resulting electronic, magnetic, and catalytic properties and opening prospects for molecular switching, axial ligation and complexation[165, 183]. For example, "metal-up" and "metal-down" switching processes, established for tetrapyrrole monomers[185, 186], should provide single-molecule switches with multiple addressable states. Furthermore, intramolecular coupling of magnetic moments and cooperative effects in ligation might be studied on these versatile tetramer model systems on the single molecule level.

The design of precursors tailored to provide square-type tetramers with high yield on coinage metal supports will help to realize the potential and applications that this study outlines on a model system. This way, ordered arrays of antiaromatic rings embedded in an aromatic molecular framework achieved by self-assembly and extended two-dimensional porphyrin sheets achieved by on-surface covalent synthesis come into reach.

Chapter 4 On-surface Synthesis and Characterization of Gulf-Type GNRs and NPG Structures

In this chapter we use the 4',5''-dibromo-1,1':2',1'':2'',1'''-quarterphenyl (dibromo quarterphenyl, DBQP) precursor in order to form well-defined gulf-type GNRs (3-CGNR-1-1, g-GNRs) and NPG structures in UHV conditions. The choice of the Au(111) surface as catalyst provides an on-surface reaction path with well-separated thermal windows that lead to a hierarchical control of the DBQP molecule transformation into oligomers, g-GNRs and NPG structures. Here we study the structures obtained in each step and their corresponding electronic properties. For this project a collaboration with the group of Dr. Aran Garcia Lekue from the Donostia International Physics Center (DIPC) was stablished, that provided us with density functional theory (DFT) calculations.

4.1 Introduction

The BU on-surface synthesis approach has been proposed as a means to achieve the construction of ever smaller components of ED. The GNR structures that have been obtained through the BU approach require chemical reactions activated by catalytic substrates, such as coinage metals (Au, Ag, and Cu). These on-surface reactions rely mostly on the Ullmann coupling and cyclodehydrogenation (graphitization)[55]. The Ullmann coupling consists of the deposition of halogenated compounds[187] (chiefly with bromine though not limited) on the reactive surface which is annealed so that a series of intermediate processes take place: at first dehalogenation which leaves a radical, second, the radical serves as the reactive site for the formation of an organometallic state C-M-C, the reaction finalizes once the C-C bond is formed[61, 188].

The electronic properties of GNRs are largely determined by their structural characteristics including their size and edge structure. For instance, armchair type GNRs can be obtained from 3',6'-dibromo-1,1':2'1''-terphenyl (DBTP)[189], 10,10'-dibromo-9,9'-bianthracene (DBBA)[55] or dibromo-perylene (DBP)[190]. Armchair GNRs can be laterally fused into wider GNRs[191], which results as another form of graphitization. Producing a GNR with an edge of the zig-zag type is significantly harder, only two precursors have been reported to produce a GNR that is uniform and has no further *outer* benzene rings[192, 193]. GNRs can display distinct structural features, such as phenyl rings that can also dehydrogenate and couple to the main structure or rings completed by

the dehydrogenation of other parts of the structure present in the precursor. Of relevance is that this external structures have an effect on the electronic features of the GNR when compared to the parent structure[49, 53, 194, 195].

Porous structures can be formed with adequate precursors, both graphene and GNRs can have different densities and forms of pores embedded in the structure. Porous graphene or nanoporous graphene (NPG) with uniform distribution of pores has been synthesized by on-surface chemistry methodologies via the lateral fusion of GNRs[49, 50, 52, 53]. GNR structures with pores already embedded in the native structure have been obtained[51, 196-198]. For GNRs to be employed in ED, the electronic properties need to be engineered[199, 200] and adequately structured pores have been theorized to turn graphene into a semiconductor of adequate qualities, something proven by lithography methodologies[201, 202].

Here, in this chapter we performed the synthesis and comprehensive characterization of the structure and electronic properties of a type of NPG with uniform distribution of pores. To this end we employed DBQP as precursor that follows the reaction steps as described, for an on-surface chemistry on UHV conditions setting. As can be observed in scheme 4.1, following deposition of DBQP on Au(111) the halogens are removed, leaving behind C radicals which in turn form organometallic structures and polymerize. The polymers finally become nanoribbons after undergoing a dehydrogenation/graphitization process[55, 59, 60, 190, 203-208]. The resulting GNRs may fuse laterally to form GNR networks (GNN), and in this case, also NPG.

Regardless of the chemical reaction utilized the end product can be made to have different structural features, such as those of figure 1.2. By comparing to the scheme 4.1, we can note that the edges of the GNR analyzed here have two features: it is of the *zig-zag* type (demarked by the thicker lines of scheme 4.1c) and also displays *gulfs*, limited by the 3 C atoms that complete a ring on the outer edge.

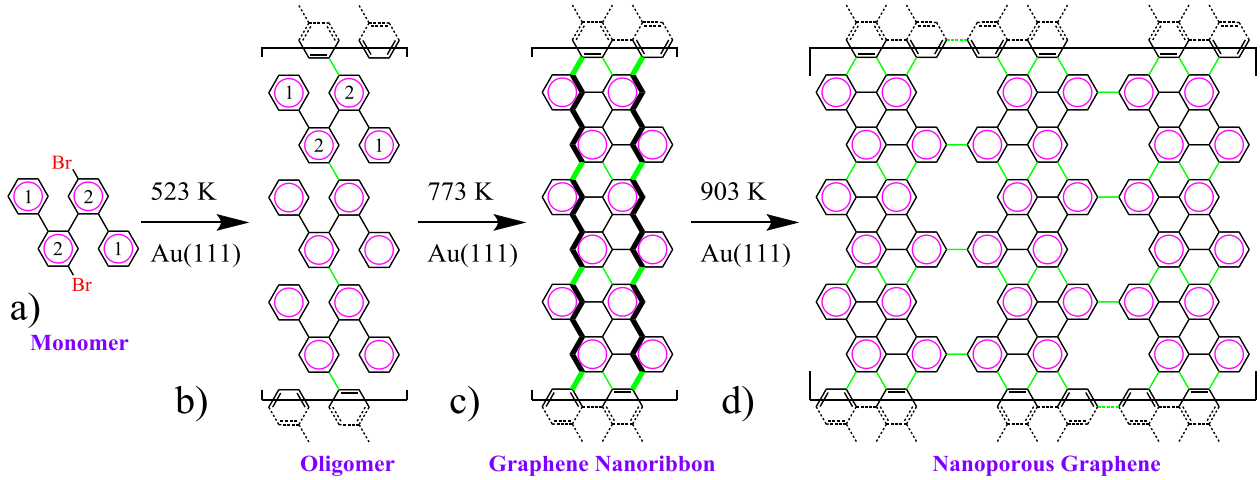

Scheme 4.1 On surface synthesis of gGNRs and NPG. a) DBQP monomer numbers, 1 and 2 denote two distinct positions on the monomers. b) Oligomer chains obtained after deposition at 523 K. c) gGNR are obtained after annealing at 773 K. d) NPG obtained by annealing at 873 K. *Kekule* structure drawing utilized not in an attempt of discussing aromaticity, but for the ease in visualization, in purple are marked the phenyl rings of the original monomer and in green the newly formed bonds between different monomers.

4.2 Polymerization and Graphitization of DBQP

The work of Kojima[50] served as reference for the procedures that follow, of importance is to state that we adapted the methodology to UHV conditions as the original work is performed by chemical vapor deposition (CVD, $1.33*10^{-5}$ bar). For the synthesis of oligomers (fig. 4.1a) the DBQP precursor was sublimated from a Knudsen cell heated to 423 K (150 °C) in UHV conditions (10^{-9} mbar), on a clean Au(111) substrate held at 523 K (250 °C), sublimation time of 60 seconds. The g-GNR was formed after annealing the sample at 773 K (500° C). To obtain NPG, DBQP was deposited for 75 seconds on the Au(111) substrate at 523 K, post annealed to 793 K (520 °C) for 1 minute and further annealed to 903 K (630 °C).

STM analysis was performed following the deposition of DBQP on Au(111) held at 523 K (oligomer phase). Since the average threshold temperature for C-C coupling on Au(111) is 463 K[209-211], the temperatures used and the periodicities measured from the STM data indicate that the product measured by STM are oligomers (figure 4.1b). From non-planar precursors, it is expected to observe protrusions due to the tilt of its components[46, 56, 59, 209]. An indication that the oligomer has been formed are the bright spots which are the tilted phenyl rings (rings labeled as 1 in monomer and oligomer in scheme 4.1). The average distance measured between the bright spots along the long axis (red line in figure 4.1a corresponds to graph 4.1b) is 0.72 nm. This is shorter

than the reported 0.76 nm (distance between C 3 and C 3´´, figure 4.1e)[212] for the more rigid *m*-terphenyl, and 0.78 nm (green line in figure 4.1a which corresponds to figure 4.1c). The termini of the oligomers were typically decorated, impeding proper characterization, however in the regions were the termini were protected, such as the one shown in figure 4.1f, we learn how the DBQP monomers are arranged in the polymers. With this information we can determine that contiguous oligomers have opposing prochiralities (see chemical models in figure 4.1a).

After obtaining this data, the g-GNR were analyzed. The same sample was annealed (773 K) as previously described to achieve the first of the two stages of graphitization. In figure 4.2a, we can observe that the once highly ordered oligomers are no longer present and the sample has become disordered. The morphology of the overall sample has changed, the *bright spots* previously described for the oligomer are no longer present (excluding the presence of amorphous organic material, purple arrow in figure 4.2a). The average measured height of several structures is 1.5 Å and the height profile differs from the oligomer (figure 4.2b). In figure 4.2c the topology of the g-GNR can be described as planar and has the alternating pattern that is expected[50]. The nc-AFM image (figure 4.2d) serves as the final confirmation of the successful cyclodehydrogenation, with the bonds between the different phenyl rings now evident. Visualized are 6 complete subunits, with the gulfs of one edge alternating positions with respect to the other.

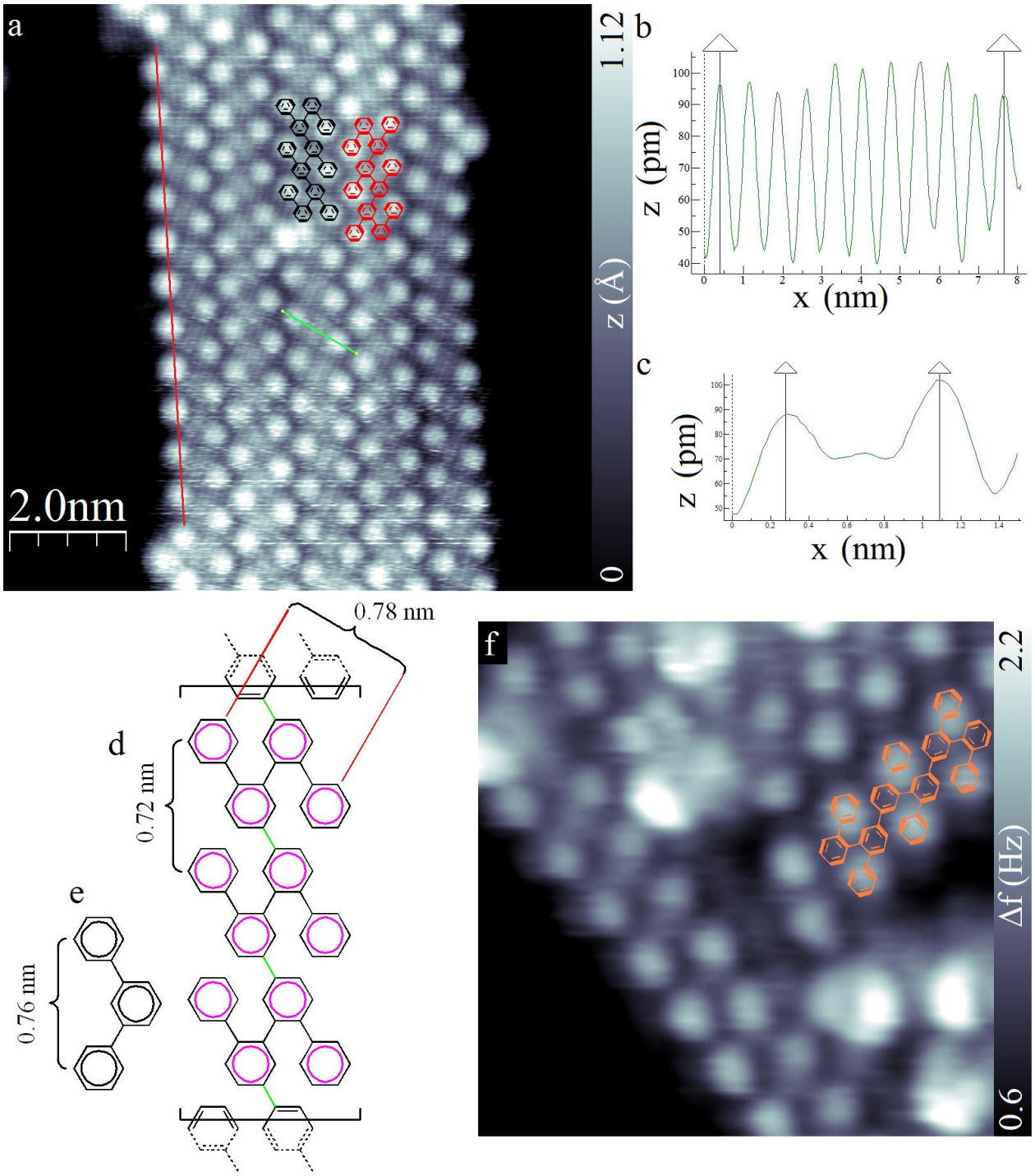

Figure 4.1 Structures of oligomers. a) STM image taken of 5 oligomer chains, H-π or π-π interactions are the likely cause for the parallel alignment (300 mV, 5 pA). b) Distance measured between spots of the phenyl rings, corresponding to the red line in *a*. c) Distance measured between the two phenyl rings that correspond to the green line in *a*. d) and e) Chemical models with the measured distances. f) STM image of the terminus of an oligomer with a partially superimposed chemical model (300 mV, 5 pA).

We can observe that straight sections comprised by 5 or more dehydrogenated DBQP subunits are scarce, the graphitized segments change direction with 120° angles, and not coincidentally this is the same angle for the bonds of the *meta* bonds as will be further explained in chapter 5.

Organometallic chains in references 210 and 213 would twist forming cyclic hexamers and higher cyclic structures at low *densities*, however at higher *concentrations* of monomers (and therefore oligomers) the lateral interactions between organometallic chains prevent them from twisting. This twisting motion is reported to not happen once C-C bonds are formed. As previously stated, deposition of DBQP on Au(111) was carried out with the substrate held at 523 K (250 °C), temperature at which the C-C covalent bond should be expected for Ullmann reactions[209]. Moreover, we can rule out an organometallic phase involved in the process due to the distances measured for the oligomers as was already discussed[214]. In this regard we can see more similarities with that which is reported in reference 215 (in the SI), in which the g-GNR synthetized in liquid phase also form similar defects. Interestingly enough, we never observed g-GNRs resting on top of one another as a result of a potential twisting motion, something that is treated on reference 216, in which predictions are made about overlapping segments of a *meta*-polyphenylene structure deposited on a surface.

The several types of defects and the chemistry that is theorized to be involved is treated with greater detail in chapter 5.

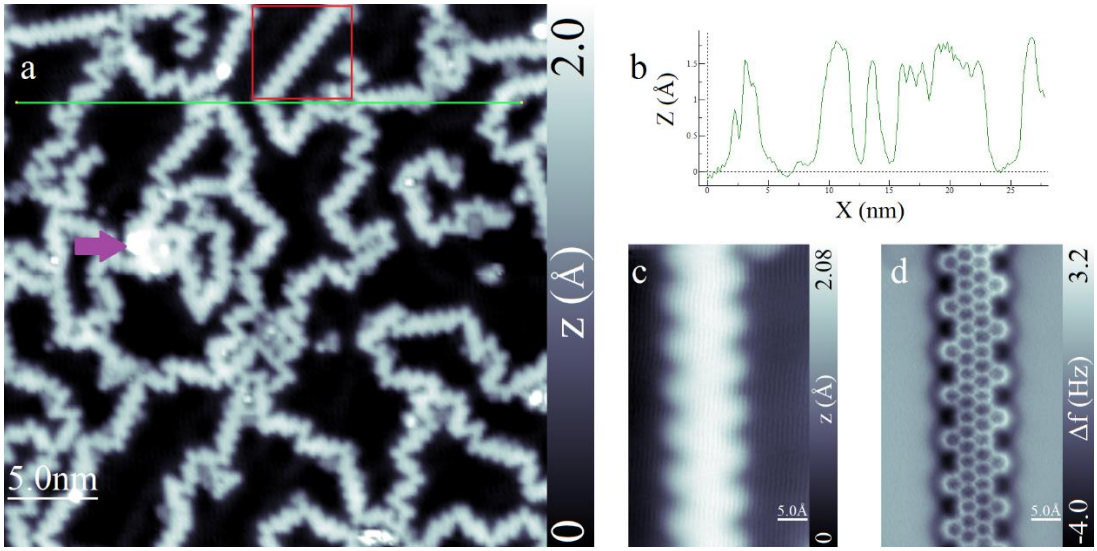

Figure 4.2 g-GNR structures. a) Large scale STM image taken of the sample with g-GNR (50 mV, 8 pA). b) Height measured along the green line in *a*. c) Close up STM image of the g-GNR segment in the red square in panel *a* (50 mV, 8 pA). d) nc-AFM with a CO decorated tip of a g-GNR.

The amount of g-GNRs is far too low, and rarely are the GNR segments parallel to each other. For these reasons the synthesis of NPG was carried out *de novo*. The deposition time of DBQP was increased expecting that higher coverages would prevent the twisting motion, and with it, decrease the amount of defects. In figure 4.3a can be observed other structures less organized with which the NPG coexist. Likewise, we can find regions where several g-GNR have fused laterally (figure 4.3b). Structural characterization was further supplemented with nc-AFM imaging (figure 4.3c). The NPG is well defined and the graphene lattice is unperturbed, apart from the pores. The values of 5.56 Å and 11.71 Å extracted from the nc-AFM image (figure 4.3d) are similar to those of the X-ray diffraction patterns of reported *kekulene* and *coronene* like structures[217, 218] (figure 4.3e) at equivalent positions. The measured distances of the NPG can only be explained by covalent links between g-GNRs via the outer most C position. The data confirms the synthesis of an atomically precise NPG.

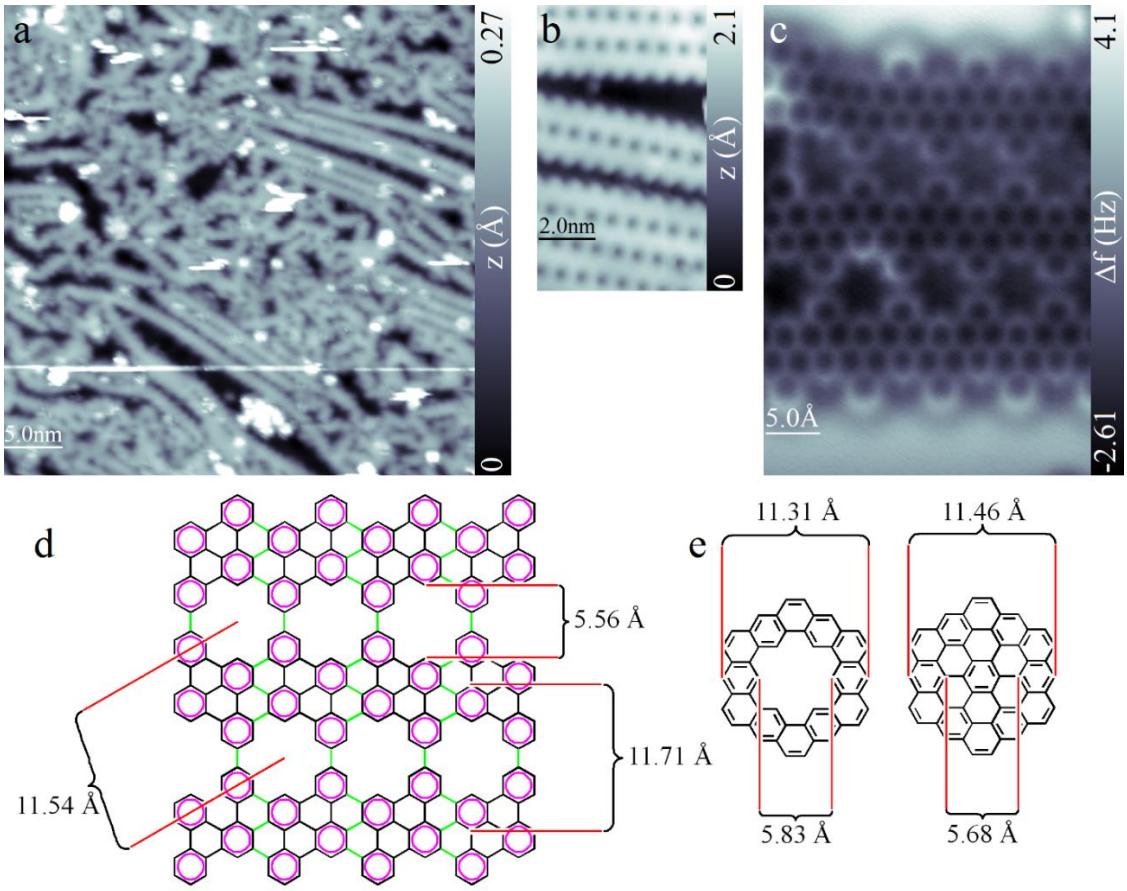

Figure 4.3 NPG structures. a) Large scale STM image taken of the sample with NPGs and other products of polymerization and graphitization of DBQP (100 mV, 6 pA). b) STM image of NPG of different width (100 mV, 6 pA). c) nc-AFM with a CO decorated tip of an NPG. d) Chemical

structure of an NPG with selected measured distances. e) Measured distances of *kekulene* and part of a *coronene* among two points that are comparable to those in the NPG.

4.3 Electronic Properties of g-GNRs

Next the electronic structure of the resulting GNR is addressed. To this end a series of dI/dV point spectra were taken at representative positions (gulf edge, outer phenyl edge, and GNR center in figure 4.4a)[219-222]. We find that scanning tunneling spectroscopy (STS) lineshapes significantly differ from that of the Au(111) substrate, which is practically featureless except for the surface state onset at -460 mV[223]. We can identify a very pronounced peak at 1.9 V that is most intense at the gulf positions, it is attenuated at the edge phenyls and appears very dim at the ribbon center. The local density of states (LDOS) is strongly asymmetric between occupied and unoccupied states. A series of peaks can still be identified between -1 and -1.5 V, located at the outer phenyl rings and gulfs. Such significant intensity variations between occupied and unoccupied states stems from the strongly varying tunneling probabilities for tunneling into or out of these states. At positive V the tunneling barrier height is effectively reduced, leading to an increased intensity, while increasing negative V, the barrier for tunneling from these states into the tip is successively increased[224].

To understand the nature of the STS peaks and capture the spatial distribution of the LDOS, constant-height dI/dV maps were acquired at selected energies (figure 4.4b). For the occupied region, the intensity is clearly localized at the lateral phenyl rings, appearing as two dots (-1.1 V) and winding along the edges (at -1.3 V and -1.5 V). In the unoccupied region (1.9 V and 2.1 V), a highly localized conductance feature is present at the gulfs. The DFT calculated band structure of the g-GNR is shown in figure 4.4d. It shows a wide bandgap semiconductor with a 1.84 eV gap. A quite symmetric band structure with dispersive and braiding bands can be seen for valence bands (VB) and conductance bands (CB) along the longitudinal axis (e.g. ΓY). These bands are non-dispersive in the perpendicular direction[211, 225]. An image potential state (IPS) band can also be identified at higher energies. Such IPS originates from the free-electron-like states that are confined at the vacuum side along the g-GNR edge[53, 226, 227]. Next, molecular orbitals are extracted for VB, VB-1, CB, CB+1 and IPS at the Γ point (figure 4.4d). While the VBs may reasonably resemble the experimental findings, the CBs are drastically different. Instead, the IPS shows orbitals located precisely at the gulfs and a good matching is obtained despite the large energy difference between the calculations and the experiment. Similar large energy differences were also observed in previous works on holey nanographenes, nanoporous networks and NPG[53, 226, 227]. For the case of

nanoporous networks the hybridization of the super atom molecular orbital (SAMO) with the Shockley surface states was tentatively proposed to cause its stabilization close to the Fermi energy.

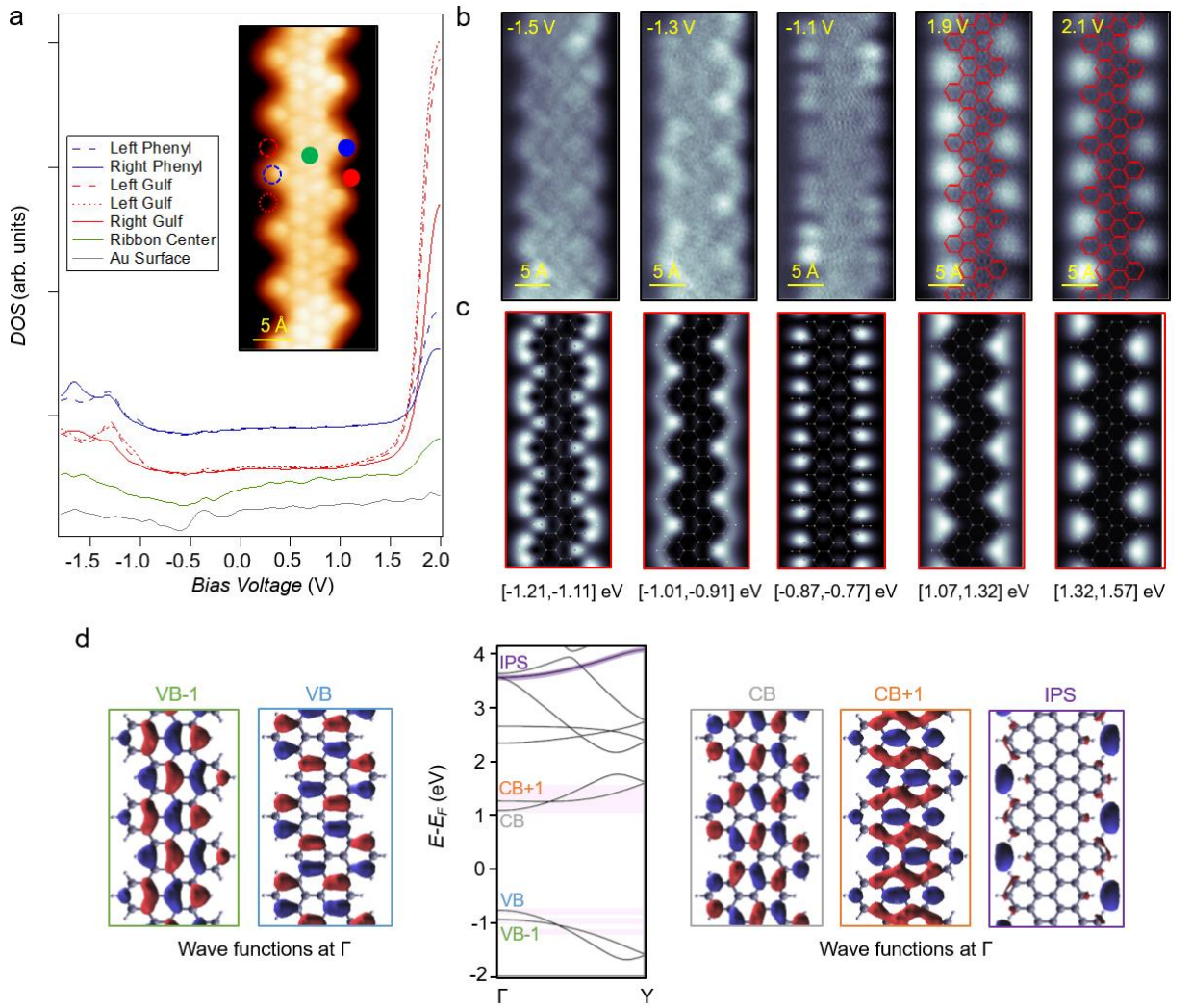

Figure 4.4 Electronic properties of the g-GNR. a) dI/dV point spectra (I= 100 pA; V_{onset}= 2 V, f= 289 Hz, V_{mod}= 30mV) acquired at right and left gulf positions (red), ribbon center (green) and right and left phenyls (blue). The onset of the VB and CB can be reasonably well identified, yielding a wide-bandgap of 2.8 V. High-resolution bond-resolved STM image (V= -8.3 mV) obtained by using a CO-functionalized tip in constant-height mode. b) Constant-height dI/dV maps acquired near the VB and CB frontier orbitals reveal a very rich substructure most prominently localized at the ribbon edges (f= 289 Hz, V_{mod}= 40mV). c) DFT simulated spatial distributions of the electron probability density ($|\Psi|^2$) at different energies close to the onsets of the VB and CB and acquired at a height of z= 5 Å away from the g-GNR plane. From left to right, the energy ranges extracted from the g-GNR band structure correspond to: (-1.21,-1.11) eV, (-1.01, 0.91) eV, (-0.87,-0.77) eV, (1.07, 1.32) eV and (1.32, 1.57) eV. d) DFT calculated band structures for the g-GNR showing dispersive and braiding VBs and CBs and a semiconducting gap of 1.84 eV. Frontier molecular orbitals, i.e., VB, VB-1, CB, CB+1 and IPS extracted at the Γ point.

To shed some light on this matter, additional DFT spatial electron probability density in the Tersoff-Hamann approximation of VB and CB. (figure 4.4c) was calculated. An energy integration of 100 meV and 250 meV were required for satisfactory matching occupied and unoccupied states respectively. A higher integration of the CBs could be attributed to a possible hybridization of CBs with Au(111)[191]. Therefore now we can confidently assign the frontier peaks at -1 V and 1.9 V to the onsets of VB and CBs. It is unlikely that IPS or SAMO states to be detected at such low bias voltages since they were observed beyond 3.7 V on graphene nanoflakes and C60 molecules on Au(111)[228, 229]. The bandgap size of the g-GNR is thus ~ 2.8 V and line dI/dV point spectra taken across both edges and ribbon center corroborate it (figure A7). Since the bandgap increases with decreasing GNR length[230], we verify these measurements on long enough g-GNRs whose properties should resemble the ones of an infinite ribbon and obtain a similar value (figure 4.5). The bandgap mismatch between theory and experiment can be attributed to the absence of a substrate in the calculations, as well as to the well-known limitation of DFT to accurately predict VB-CB gaps. These findings unambiguously correct the previous experimental assignment of 1.1 eV narrow-bandgap for the g-GNR/Au(111) system[50].

We further verify these CBs dI/dV maps on longer g-GNR segments (figure 4.5), even extending to bias voltages as high as 3 V (beyond which CO-tip and g-GNR integrity are compromised). All measurements show the same gulf confined quasi nanopore states. DFT spatial electron probability density ($|\Psi|^2$) simulations show that indeed all CBs (with atomic orbital origin) follow this pattern which is curiously almost identical to the one of IPS that appears at higher energies. Since the simulations are performed without the substrate, the Au surface state confinement is ruled out as their origin and can be unambiguously attributed to the CBs (figure A8 and A9).

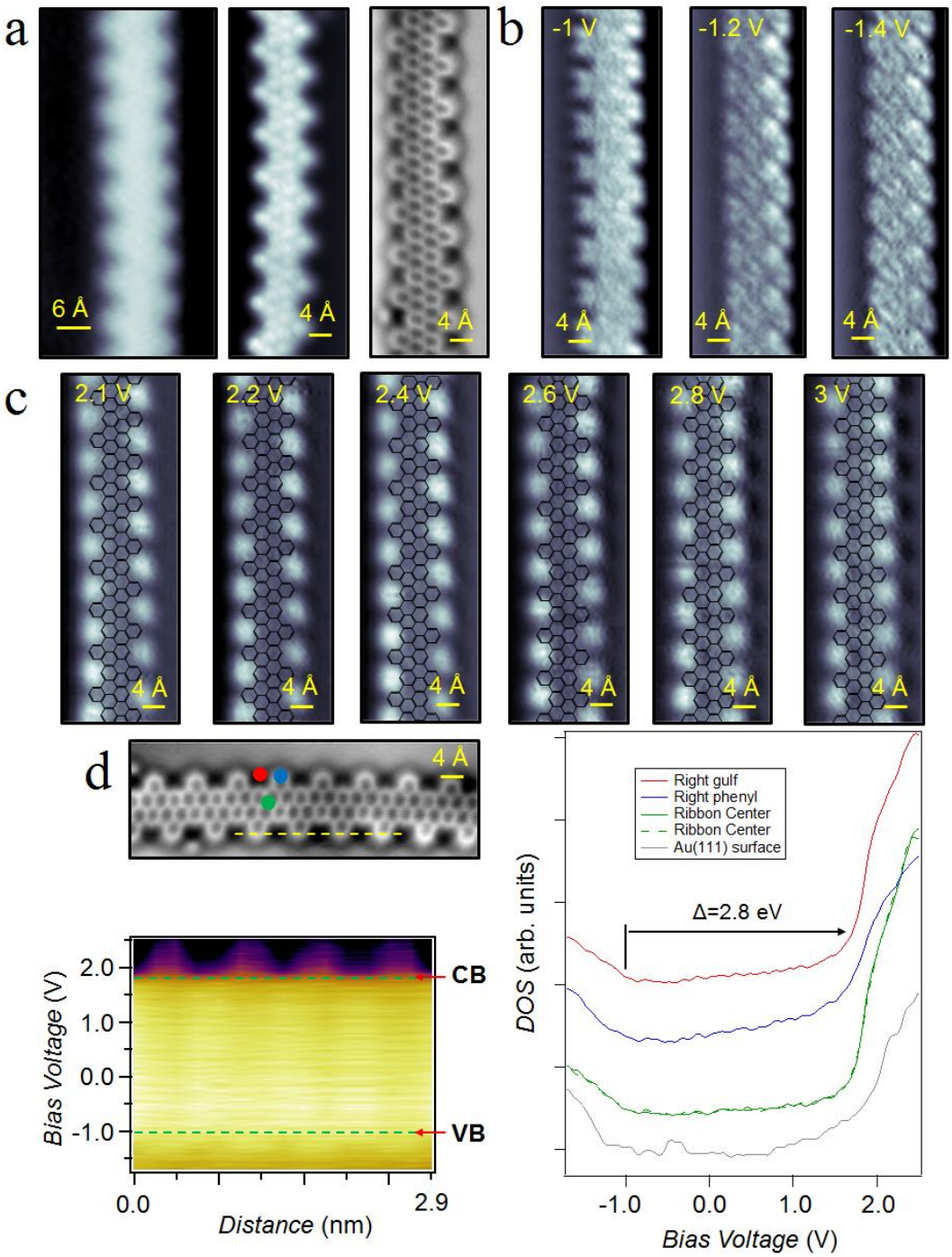

Figure 4.5 Electronic properties of an eight-unit cell long g-GNR. a) L-R, high-resolution STM (I= 10pA; V= 100mV), NC-AFM and BR-STM (V= 3mV) images of the g-GNR confirm its well-defined structure. b) and c) Set of dI/dV maps acquired for VBs and CBs. For the CBs the maps are extended up to 3 V, beyond which g-GNR and CO-tip integrity are compromised. d) LDOS intensity map corresponding to a line dI/dV point spectra (I= 100pA; V_{onset}= 2.5V; open feedback loop) acquired at one edge of the g-GNR and point spectra acquired at different positions of the g-GNR: gulf (red), edge phenyl (blue) and ribbon center (green). Despite the LDOS asymmetry, a 2.8 V wide-bandgap can be measured.

4.4 Electronic Properties of the NPG Structure

Similar to the g-GNR case, we perform dI/dV point spectroscopy at different representative positions of the NPG (figure 4.6a): nanopores (red), ribbon centers (blue) and edge gulf (green). The LDOS is again asymmetric (figure 4.6b) where a very intense peak can be seen at 2 V, located mainly at the nanopore centers (red spectra). The shoulder in the occupied region is again less intense but a peak can be clearly observed at -1 V at the NPG edge (green spectrum). The band gap is similar to the single g-GNR case (~2.7 V) and the small reduction is expected for coupled g-GNRs[53]. The onset of the VB seems to be pinned in energy at -1 V. This shows that the wide-bandgap is preserved upon the NPG formation and we correct the previous experimental assignment of a 1.14 eV narrow-bandgap NPG[50]. In order to study the spatial distribution of the LDOS, we perform constant-height dI/dV maps close to the VB and CB onsets. For the VBs (figure 4.6c), the intensity appears localized at the nanopore edges like a hexagonal ring pattern and at the NPG edge (-1 V and -1.2 V). Interestingly, the NPG edge behaves similarly to a g-GNR edge and the conductance features are identical to the ones observed in figure 4.4b (e.g., the double dot conductance features located at the phenyls for the VB). This corroborates that the VB is pinned in energy at -1 V. For the unoccupied region (figure 4.6d), now the intensity appears localized at the nanopores (resembling nanopore confined IPS or SAMO states) and gulfs at the NPG border (with less intensity than nanopores due to lack of inter-g-GNR coupling). Such nanopore conductance features have been observed in holey nanographenes[226, 231], molecular nanoporus networks[227] and NPGs[227] and they were assigned to LUMO, negative ion resonance (NIR), IPS or SAMO states. DFT calculations of the band structure confirm the semiconducting character of the NPG with a slighly reduced bandgap (1.63 eV) compared to the single g-GNR (1.84 eV, figure A10). The highly dispersive bands in both orthogonal directions of the NPG (along the g-GNRs ΓY and across ΓX) confirm the rather high electronic isotropy of this system in comparison to the more anisotropic NPGs (figure A10)[52, 53].

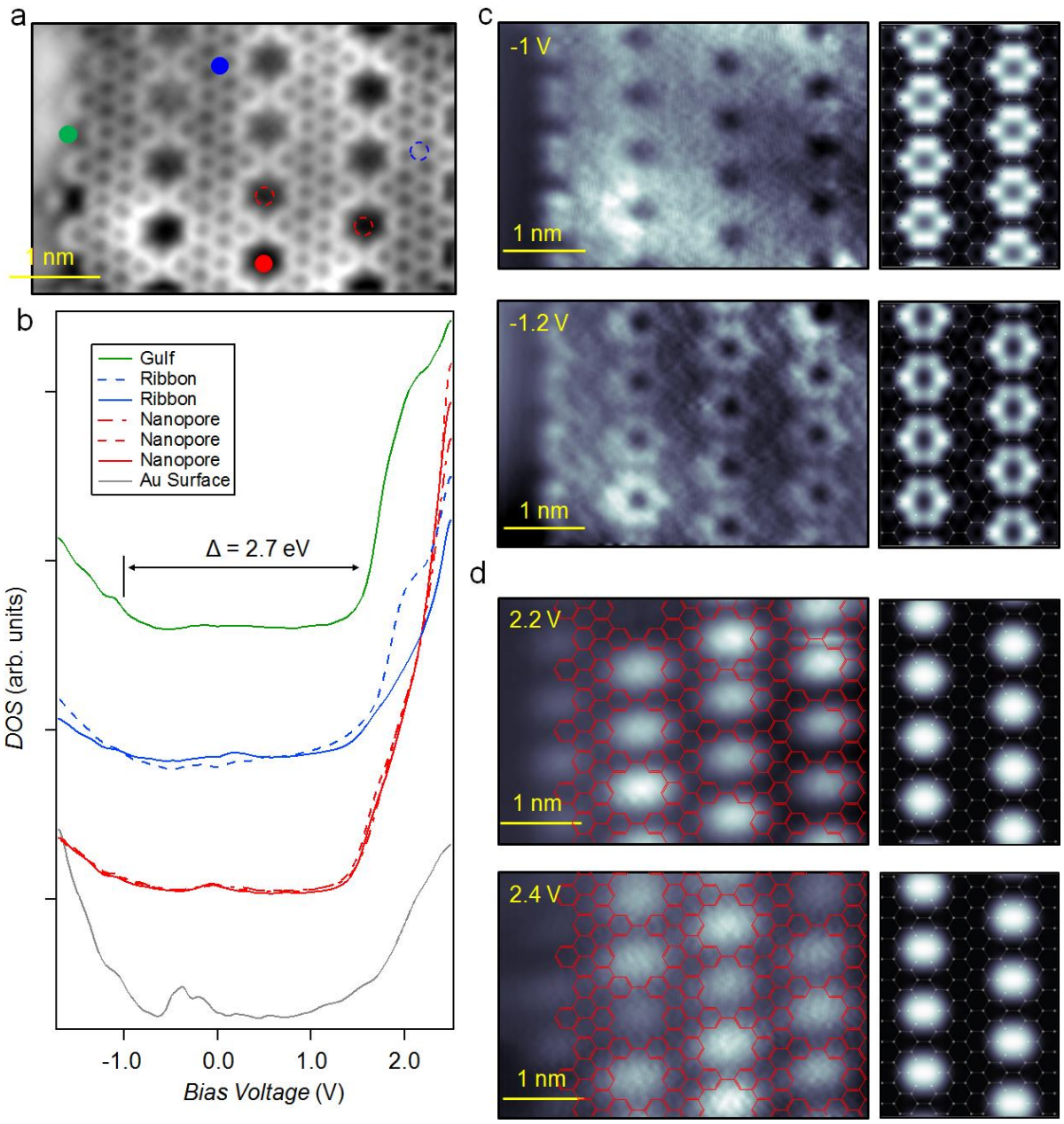

Figure 4.6 Electronic properties of a four g-GNR fused NPG (4-NPG) structure. a) nc-AFM image of a 4-NPG. The colored dots indicate the point spectroscopy positions. b) dI/dV point spectra (I= 70 pA; V= 2.5 V) acquired at different positions of the 4-NPG and Au(111) substrate (gray). Despite the weak intensity of the VB onset compared to the prominent CB (similar to the g-GNR case), a band gap of 2.7 V can be extracted. c) Constant height dI/dV maps acquired close to the onset of the VBs and their respective DFT spatial electron probability density ($|\Psi|^2$) simulations extracted from (-0.89,-0.69) eV and (-1.09,-0.89) eV ranges in the NPG band structure (figure A11). d) Constant height dI/dV maps acquired close to the onset of the CBs and their respective DFT spatial electron probability density ($|\Psi|^2$) simulations extracted from (1.17,1.42) eV and (1.42, 1.67) eV ranges in the NPG band structure.

Molecular orbitals extracted for the VBs and CBs at the Γ point show delocalized electronic wave functions over the entire structure and the formation of bonding and anti-bonding states at the g-GNR fusing positions (figure A10). While for the VBs the molecular orbitals may again reasonably resemble the experimental dI/dV maps, the CBs look drastically different. Only the IPS is in good agreement with the experiment but again, a high energy difference is apparent (>1.5 eV). Therefore, DFT calculations of the spatial distribution of the electron probability density ($|\Psi|^2$) are performed at z = 5 Å for the VBs and CBs (figure 4.6c and 4.6d). The hexagonal ring and dome-shape conductance features appearing around and inside the nanopores for the VBs and CBs respectively are perfectly reproduced. An energy integration of 200 meV and 250 meV is required for a satisfactory matching of occupied and unoccupied states respectively. Such CB nanopore states can be continuously observed in the experiment for voltages as high as 3.2 V (beyond which CO-tip and NPG integrity are compromised, figure 4.7) and in DFT until the intrinsic nanopore localized IPS is reached, which again shows a very similar pattern to the CBs (figure A11). In the experiment the IPS could not be probed, which is expected to appear beyond 3.7 V.

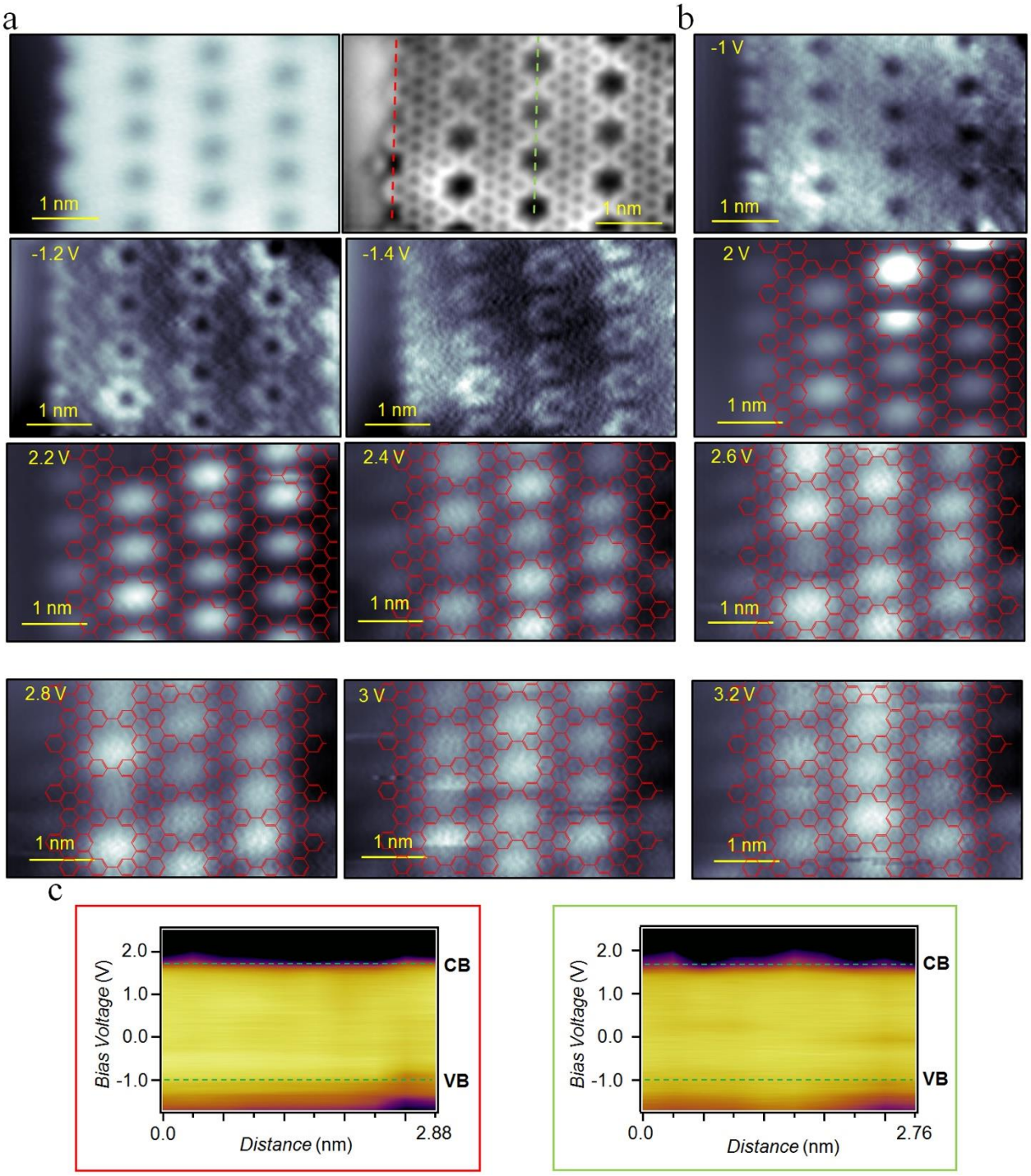

Figure 4.7 Electronic properties of a 4-NPG. a) High-resolution STM (I= 10pA; V= 100mV) and NC-AFM images of the 4-NPG. The 4-NPG is well-defined and the graphene lattice is unperturbed. b) Set of dI/dV maps acquired for VBs and CBs. For the CBs the dI/dV maps are measured as high as 3.2 V, beyond which NPG and CO-tip integrity are compromised. c) and d) correspond to LDOS intensity maps for dI/dV line spectra (I= 70pA; V onset = 2.5V; open feedback loop) acquired at the border and inside the NPG in accordance to the red and green color coded dashed lines in panel *a*.

4.5 Summary and Outlook

This chapter presented the structural characterization by STM and nc-AFM imaging of oligomers, g-GNR and NPG, all products of polymerization and graphitization of DBQP, as well as the electronic characterization of g-GNR and NPG.

The graphitization process to obtain g-GNR from DBQP on Au(111) in UHV conditions results in many defects. To obtain NPG the coverage has to be increased. Even then yield is low.

The electronic properties of g-GNR: wide bandgap semiconductor (2.8 eV). The dI/dV maps are well understood with DFT simulations of the spatial distribution of the electron probability density.

The electronic properties of NPG corresponds to a wide bandgap (2.7 eV), the VB is pinned at -1 V. The dI/dV maps are correctly understood again with DFT simulations.

The high conductance features observed in g-GNR gulfs and NPG pores in the unoccupied region originate from the different CBs. It is unlikely that they originate from IPS or SAMO states, as has been recently suggested in references 53 and 226.

Chapter 5 Defects of DBQP Polymer Products

This chapter shows the multiple defects after the synthesis of GNR and NPG with DBQP. Rational and chemically sound mechanisms for defect formation based on published literature of the chemistry of polyphenylene compounds are proposed.

5.1 Introduction

Bottom-up (BU) on-surface synthesis as a method to fabricate electronic devices from molecular GNR precursors has the advantage of being able to design the preferred structure/properties. Having accomplished the characterization of 3-CGNR-1-1 (g-GNR) in the previous chapter, we sought to establish the structure at the points in which the GNRs found would deviate from the expected results by undergoing (unexpected) side reactions. The evidence gathered with STM and AFM imaging techniques, indicated the presence of distinct motifs that were not formed by random polymerization. A comprehensive understanding of the synthetic pathway of analyzed GNR defects can help design precursors that yield less defects.

For ease of interpretation the chemical structures in schemes and figures were drawn making use of colors as depicted in figure 5.1. The DBQP monomer is expected to undergo two reactions, namely Ullmann coupling and dehydrogenation. The monomers that are determined to solely undergo these reactions are drawn in purple colored circles. The bonds between monomers are marked in green. If a monomer has undergone another reaction it is marked in red. Blue is used to mark sections for which we do not have enough information.

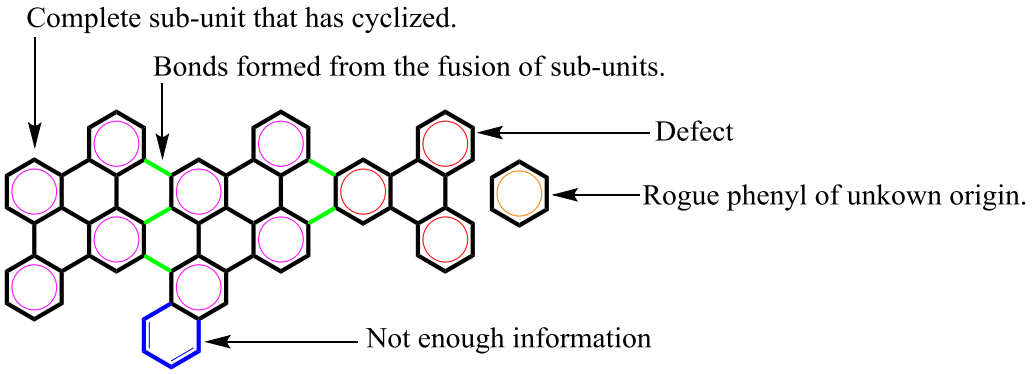

Figure 5.1 Color code used in this chapter. Clar sextets used for simplicity, not intended to discuss aromaticity. Purple rings represent the starting monomers. Red rings mark subunits product of decomposition. Blue rings/double bonds, AFM image does not offer enough information on. Green bonds are product of Ullmann coupling and cyclization between 2 monomers. Orange rings represent phenyl groups that are not part of the original monomer.

It is worth to briefly recapitulate the steps followed to obtain g-GNR and NPG (scheme 5.1). Upon deposition at room temperature on coinage metals brominated and iodinated monomers quickly undergo homolytic cleavage, thus creating a radical molecule. As the annealing temperature increases an organometallic (OM) C-M-C state appears, followed by the formation of C-C bonds[61]. Depending on the system there is an internal cyclodehydrogenation closing rings within the newly formed chain and lateral fusion of these new polymers may occur, these two steps are commonly referred as graphitization (scheme 5.1).

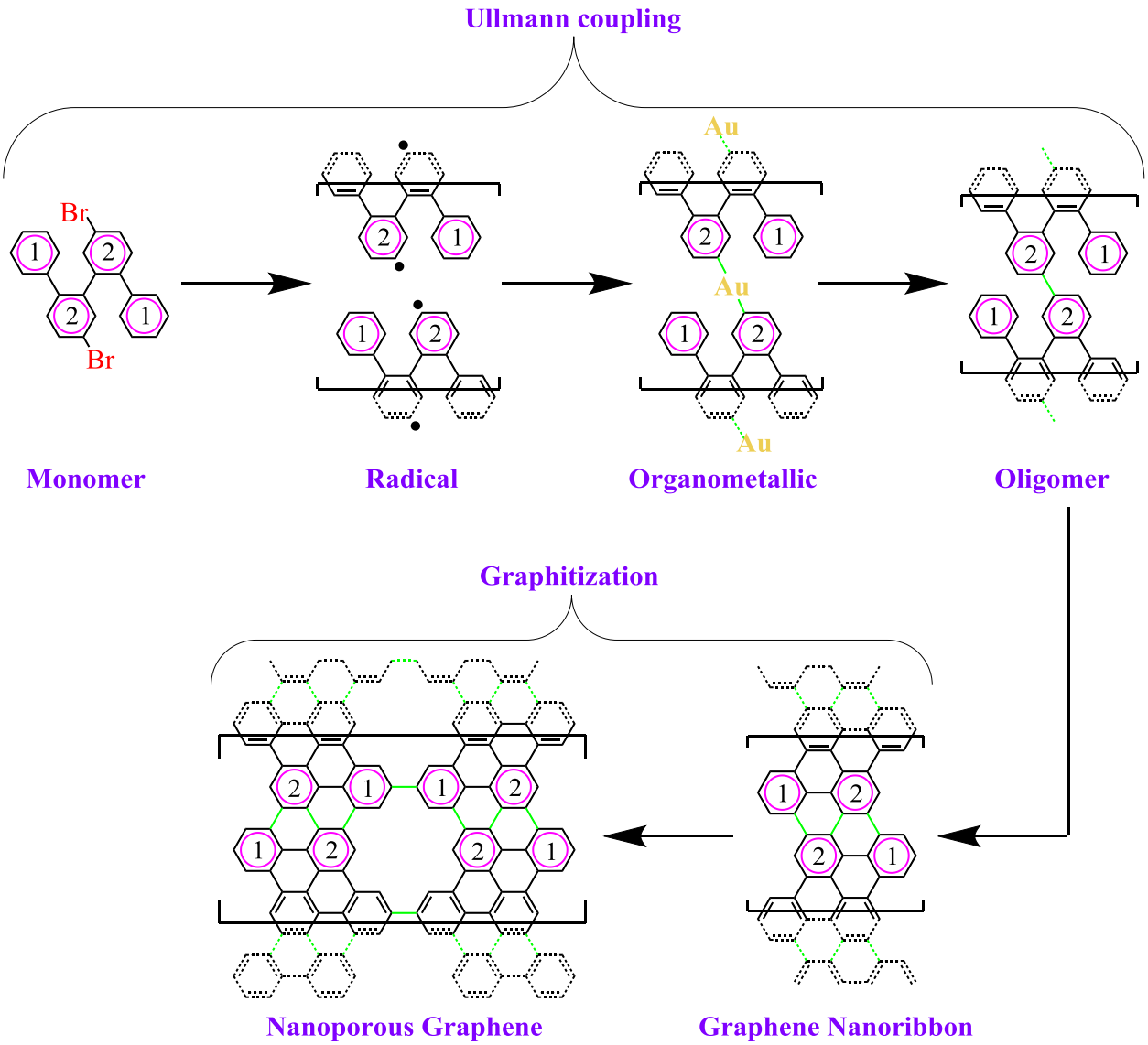

Scheme 5.1 General mechanism in the synthesis of g-GNR and NPG. Depicted are the various stages in the synthesis of NPG from DBQP, in order or thermal activation.

It is important to understand every step in the chemistry required in the synthesis of an NPG and the factors that need to be met. Upon deposition precursors with the same carbon backbone but different halogens have different diffusion rates due to passivation by the halogen itself, and as the annealing temperature increases polymers start to be formed and display similar behavior irrespective of the halogen of the precursor[56, 57]. The same carbon structure that serves as precursor can display different chemical routes and thus prefer different products by changing the substrate or even different products on the same substrate by changing parameters (e.g. temperature of deposition)[59, 205, 206]. A smart conclusion by Galeotti *et al.*, is that "*the halogen should not be considered a by-product, but rather an important parameter governing the on-surface Ullmann polymerization reaction"*[56]. For example, Br atoms remain on the surface long after the Ullmann coupling has taken place and while they do not play a role in the dehydrogenation process, it affects the interactions between the polymer and the substrate[232]. The organometallic phase is not entirely stable, atomic hydrogen can passivate this stage by breaking the C-metal-C bonds and replace with C-H bonds[233], likewise the presence of contaminants can lead to the same result[59]. Finally we can mention that during the graphitization process undesired products can be formed, such as *kinked* bonds with dibromo-perylene (DBP)[208], which results in the subunits binding at unintended positions in the form of a pentagon. Of consideration is the fact that once the reaction has finalized the UHV conditions necessary for SPM analysis, in equipment such as ours, prevents the termini of the GNR once occupied by halogens from reacting. These C positions remain available as reactive sites, and can be passivated either by capturing H atoms present in UHV or other reactants such as oxygen[168, 204].

Scheme 5.2 summarizes three types of dibromo-terphenyl molecules that have been used to produce GNRs. Two of them, namely 4,4''-dibromo-*para*-terphenyl (DBPT, scheme 5.2a)[189] and 3',6'-dibromo-1,1':2',1''-terphenyl (DBTP, scheme 5.2b)[191], undergo Ullmann coupling exclusively at antipodal positions, with the end product being a linear GNR. Two other dibromo-terphenyl molecules in which substituents are in *meta* positions, result in small oligomers of no relevance to this topic (scheme 5.2d monomeric structures)[234]. A third one, 4,4''-dibromo-meta-terphenyl (DMTP, scheme 5.2c) results in oligomers that describe a *zig-zag* with internal angles of 120° pattern due to the *meta* bonding of the precursor. This precursor can also form self-closing oligomers, reported are cyclic hexamers on Cu(111)[213], Ag(111)[210]. In the latter other longer self-closing oligomers are formed. The chemistry of DMTP on these substrates is different on Ag(111).

This mostly happens if at the organometallic stage the C-Ag bonds break and the monomers reassemble. If the C-C bond is formed, then the entire oligomer must rotate, with much higher energy restrictions. Worth noting is that the van der Waals force play a role, as with higher coverage this self-cyclization is reduced.

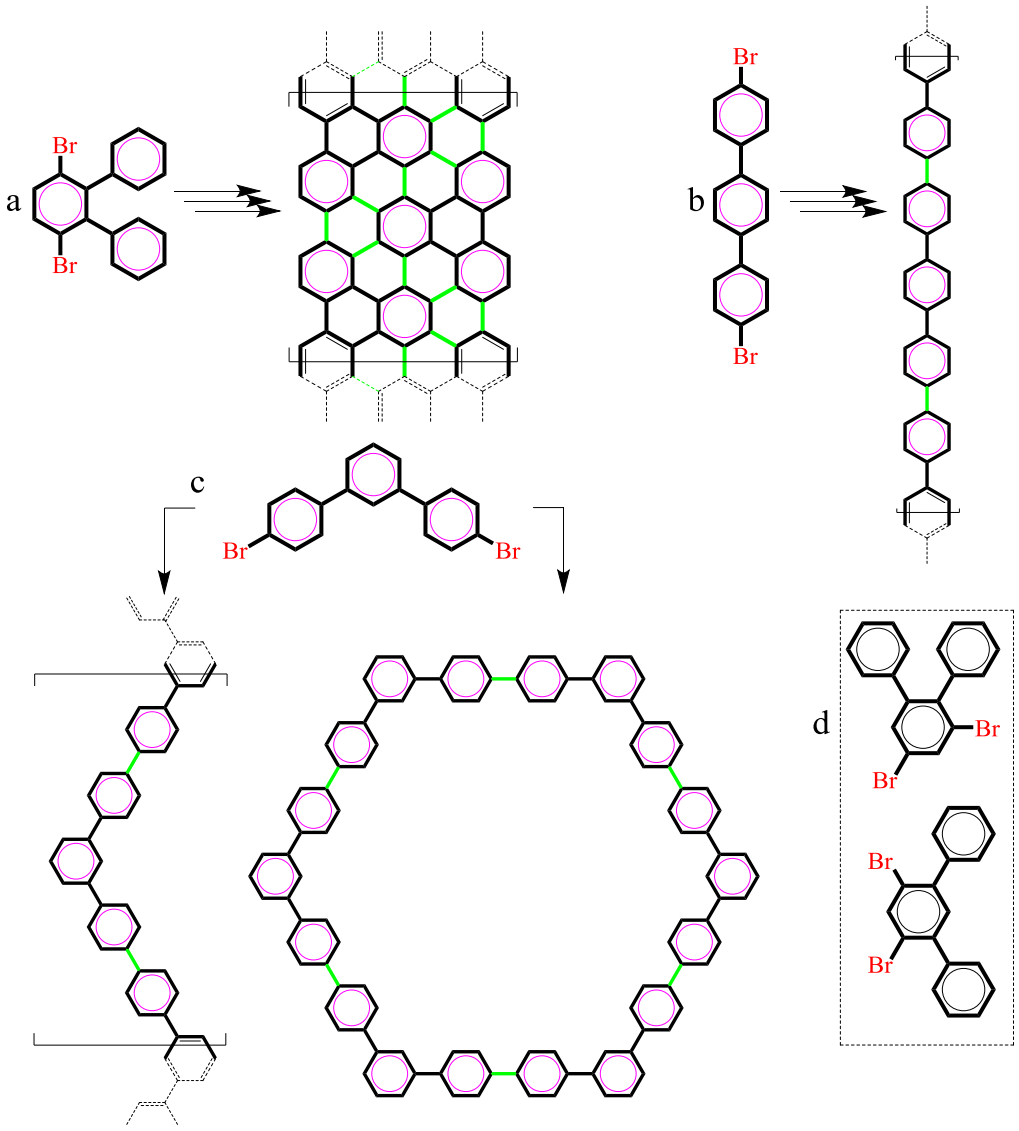

Scheme 5.2 *meta*-terphenyl precursors. a) DBPT monomer and resulting GNR. b) DBTP monomer and resulting oligomer. c) DMTP monomer and oligomers. d) Two different dibromo-terphenyl monomers that do not result in GNRs.

5.2 Types of Defects and Proposed Reaction Mechanisms

Defects were readily found on the surface of the sample after annealing to produce GNRs and NPGs, with eight very well defined motifs, seven of which can be explained by comparing the resulting structures with what is found in the literature of polyphenylene molecules and their

chemistry in solutions. These defects will be addressed in detail in sections 5.3 and 5.4. Here we highlight some general aspects of defects.

The prototypical g-GNR that results from the DBQP precursor is linear, with gulfs at its edges (as described on figure 1.3, schemes 4.1, and 5.1). The cyclodehydrogenation of DBQP, results in a dibenzo[fg,op]tetracene moiety (TT, figure 5.1e, also found in literature as dibenzo[fg,op]naphtacene). It is these moieties that aligned form the g-GNR. As seen on AFM images (figures 5.1a, 5.1c) and the respective molecular models (figures 5.1b and 5.1d), we can identify TT moieties that conform the g-GNR. At some locations at which the g-GNR features a 120° angle (elbow) a different moiety appears, being that of a triphenylene (TRP, figure 5.1f). We can also notice how at a TT moiety comprises an elbow, but it is not in the expected configuration for a GNR (figure 5.1b). Finally, we can identify a region in which three consecutive TRP structures are located (red arrow in figure 5.1d).

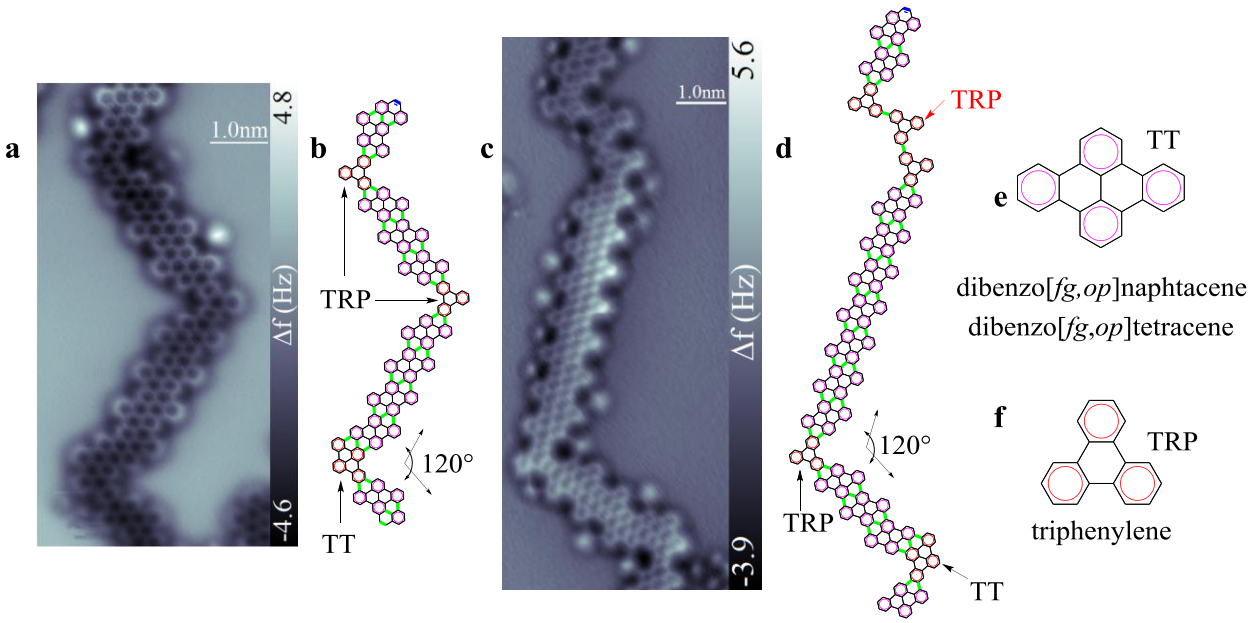

Figure 5.1 Types of defects found after the graphitization of DBQP oligomers into g-GNRs. a) and c) AFM image of a GNR with 3 turns. b) and d) corresponding chemical models of imaged GNRs *a* and *b*. e) chemical model of the dehydrogenated DBQP monomer. f) chemical model of triphenylene.

5.2.1 Triphenylene Moiety by Decomposition of DBQP

The presence of a TRP moiety can indicate the loss of a phenyl ring and/or a defective DBQP precursor. Of those two options we can rule out the presence of defective precursors. STM images of the oligomers are consistent with the expected result of a successful Ullmann coupling of DBQP monomers. STM imaging at the oligomeric stage would result in the absence of the bright spots that correspond to ring 1. Furthermore ring 2 is necessary for the Ullmann coupling to take place (scheme 5.1). Decomposition of polyphenylene molecules has been reported to take place in solid matrices with thermal treatment[235].

As noted before in section 5.1, terphenyl molecules with *meta* bonds, are capable of rotating, though it is primarily at the organometallic stage via the scission of the organometallic bonds (C-Ag-C), rotation is also possible once the oligomers (C-C bonds) have been formed.

The rotation at the central bond of a subunit helps to explain not only the change in angle, but it also helps to establish a mechanism that explains the loss of a phenyl ring. As seen on scheme 5.3, rings 1 and 1* come close after a rotation around the bond situated between phenyl rings 2. In this scenario ring 1* is close to the Au(111) substrate which catalyzes the next processes. Based on literature the mechanism involved could be an initial homolytic C-C bond cleavage (scheme 5.3a) (though current reports require a metal oxide interface)[236, 237], hydrogen transfer either as protons[235, 238, 239] or monoatomic hydrogen present on the surface[60, 240] (scheme 5.3b). All mechanisms are possible to coexist given the properties of Au and polyphenylene molecules.

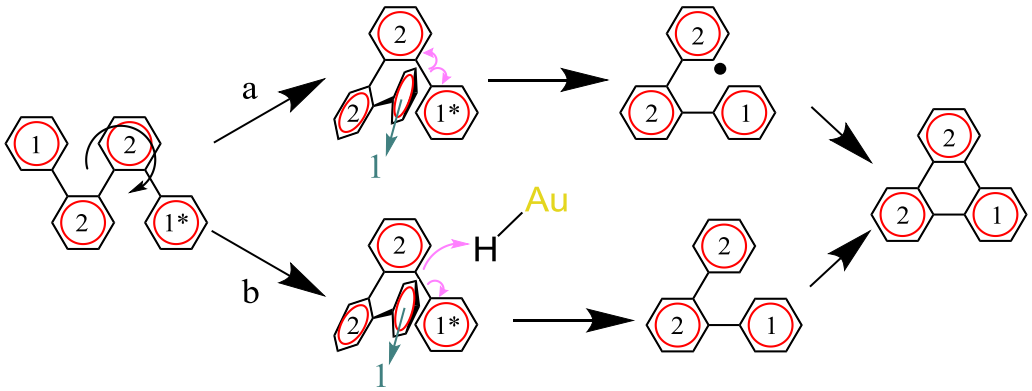

Scheme 5.3 DBQP phenyl cleavage. In the depicted mechanisms, the rings marked as 2 form the continuous chain of phenyl rings at the oligomer stage. Rings marked as 1 and 1* are those that comprise the outer most section of the gulf in the g-GNR. Once the rotation event has terminated, the Au(111) slab catalyzes the cleavage of the phenyl ring, as it is the only one capable of undergoing a chemical reaction.

5.2.2 Rearrangement by Initial Shift of Phenyl Ring

Similar to the previous reaction, we can see on scheme 5.4 that the leading step is a twist at the central bond within a subunit, this time however we can see that all four rings are present in the resulting GNR. This can be explained with a similar mechanism to the one postulated by Ormsby *et. al.*, when studying substituted quaterphenyl species[241, 242]. The replacement for the proton coming from the acid used in the solution, could be the Au slab which not only stabilizes radicals, it is also known to be a Lewis acid (as shown in the second and third step of scheme 5.4), with two reviews[243, 244] been published recently describing a plethora of reactions with mostly Au(I) as the reactive species. Similarly a rearrangement due to hydride removal could lead to this structure[245].

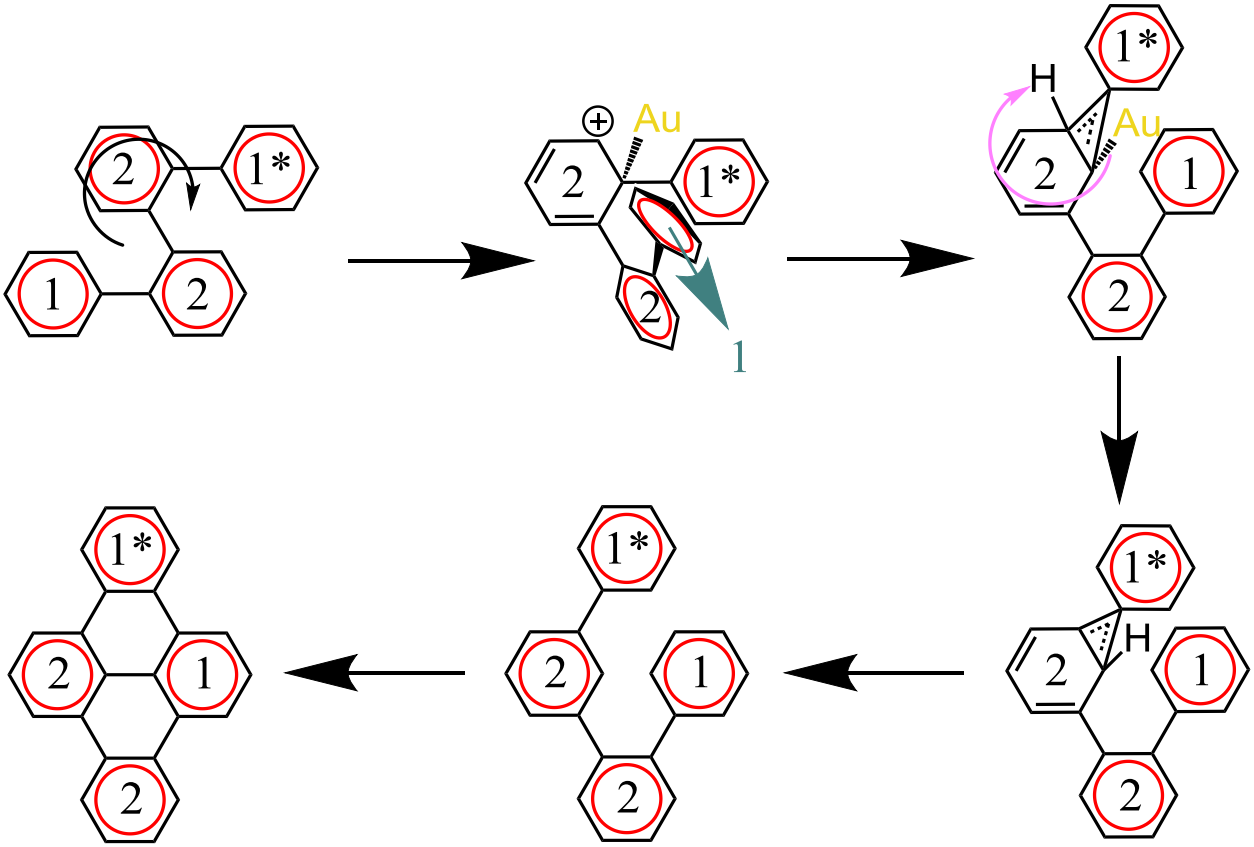

Scheme 5.4 DBQP phenyl rearrangement. In the depicted mechanism, the rings marked as 2 form the continuous chain of phenyl rings at the oligomer stage. Rings marked as 1 and 1* are those that comprise the outer most section of the gulf in the g-GNR. Notice that phenyl rings are connected through bonds at *ortho* positions from each other, once the rearrangement finalizes, phenyl ring 1* is in *meta* position with respect to the position of the bond between phenyl rings 2.

5.2.3 Elimination and Rearrangement by Initial Cyclization

A possibility that needs to be explored is the cyclization as the first step that takes place in the synthesis of the g-GNR.

Three main mechanisms have been postulated for the dehydrogenation of DBBA oligomers on Au(111)[246-248]. The mechanisms proposed in reference 246, have the dual elimination of H after cyclization. The main mechanism has the C atoms bend towards the surface and the two H atoms released as H. The minor mechanism has the release of both H atoms as H_2. Scheme 5.5a shows these two mechanisms applied to our system. Due to steric hindrance, the phenyl ring that now lays on top of another (phenyl rings 1 and 1* respectively) has no access to the Au(111) substrate which catalyzes the reaction. As such, ring 1* and ring 2 must be the one that form a cycle as depicted in scheme 5.5a. then the elimination of the phenyl ring can proceed in a concerted manner, in the form of benzene or the radicals of the phenyl group and H atom. A third mechanism is shown in scheme 5.5b (considered unlikely by the authors) requires the initial elimination of an H atom, followed by a stage in which the remaining H atom is shared by the anthryl units. Similarly, the H atom, which faces less impediment can lower to the Au(111) slab and the substrate catalyzes the H-C bond cleavage, the now free C atom can bind to phenyl rings 1 and 2 and in the next step eliminate the phenyl radical as depicted in scheme 5.5b.

In the reaction mechanisms proposed in references 247 and 248, the H atoms at the positions in which the anthryl units cyclize shift positions as depicted in scheme 5.5e. The two mechanisms involve an initial cyclization followed by H shift. Both mechanisms could explain the shift of the phenyl rings, and both have the same end product as seen on scheme 5.5c[247] and scheme 5.5d[248].

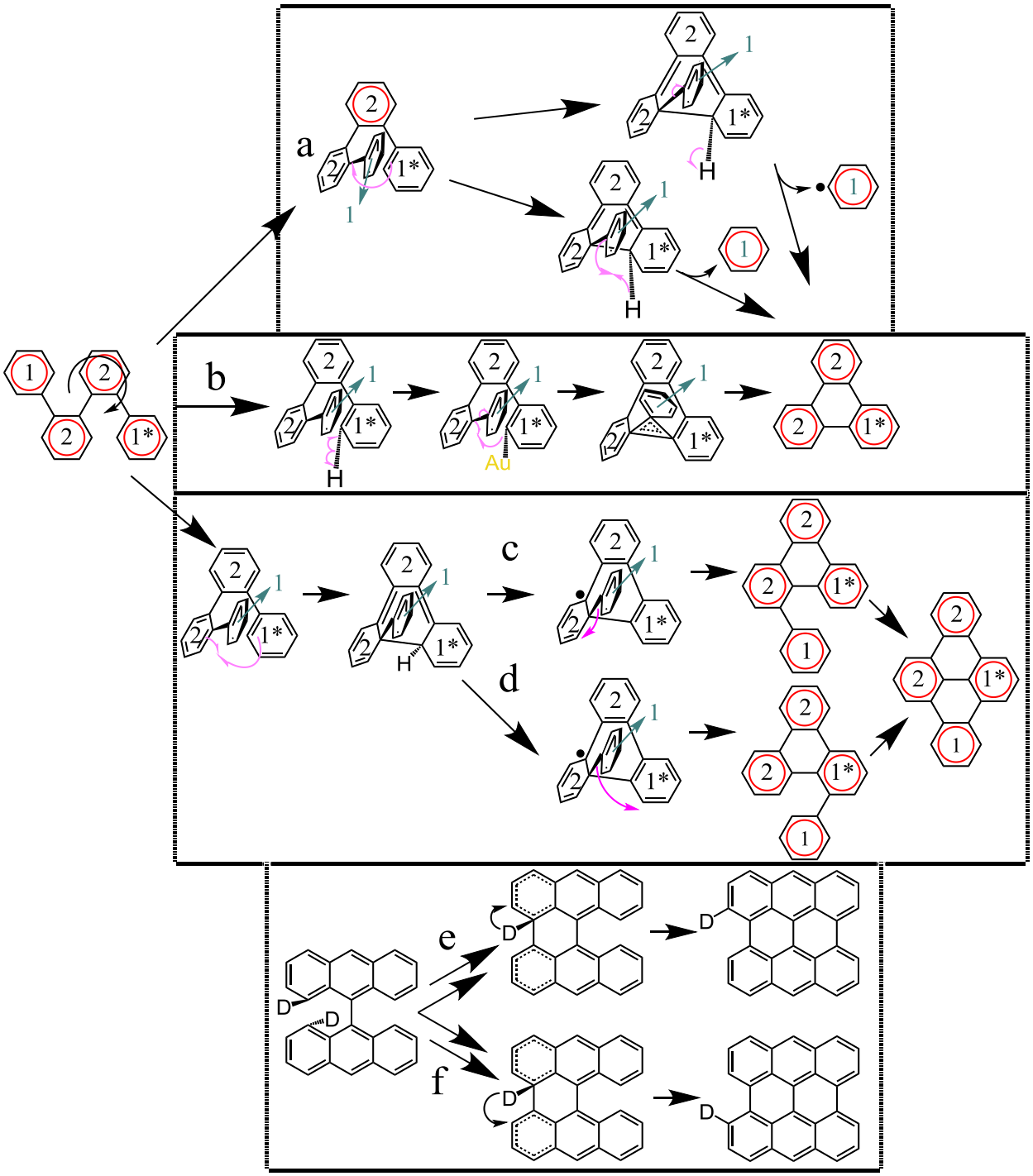

Scheme 5.5 Mechanisms with initial cyclization. a) Elimination of phenyl ring can be as a radical or as benzene. b) The elimination of the phenyl ring is preceded by an organometallic stage and an intermediate cyclization. c) and d) the H atom near the surface is cleaved and the phenyl ring shifts to the C atoms as marked, end product is the same. e) and f) though both mechanisms have the H atom marked as deuterium, reference 247 made no use of it, the use in this models is for clarity, only in reference 248 was the molecule marked with deuterium.

One more set of reactions that can create rearrangement and/or cleavage of phenyl groups are those reported for cycloarenes. These set of reactions are ruled out due to the impossibility of stablishing how a Diels-Alder reaction could take place with a phenyl ring overlapping another[249, 250].

5.3 g-GNR structures with defects

The previously described mechanisms can explain defects in the chemical structure. In this section some of the detailed mechanisms are applied to oligomers in different stages of graphitization. Defects are classified as motifs. Higher resolution images of the mechanisms that lead to the motifs A, B and C that follow will appear in the annex.

Motif A. The AFM image in scheme 5.6a shows the most commonly found defect in the synthesis of GNR with DBQP, consisting of a GNR with a change of direction that describes a 120° angle, the inflection point being a triphenylene moiety. As seen on scheme 5.5b, for a GNR to change direction describing a 120° angle the GNR has to rotate at the central bond of a DBQP subunit that has not undergone cyclodehydrogenation. In the mechanisms of scheme 5.6b are applied the previously described phenyl cleavage reactions (scheme 5.3) at the oligomeric stage. In these two possibilities (scheme 5.6b) the two immediate DBQP subunits that surround the DBQP that will become a TRP, have already undergone the process of dehydrogenation. The mechanism on scheme 5.6c depicts three stages of the twisting motion in which two contiguous DBQP subunit are not graphitized. The end result are two triphenylene moieties connecting by a single bond two g-GNRs segments. The flexibility of a chain with abundant single bonds would result on several phenyl rings offering steric hindrance and tension[210, 213, 215, 216, 251, 252], this is most relevant for motif E.

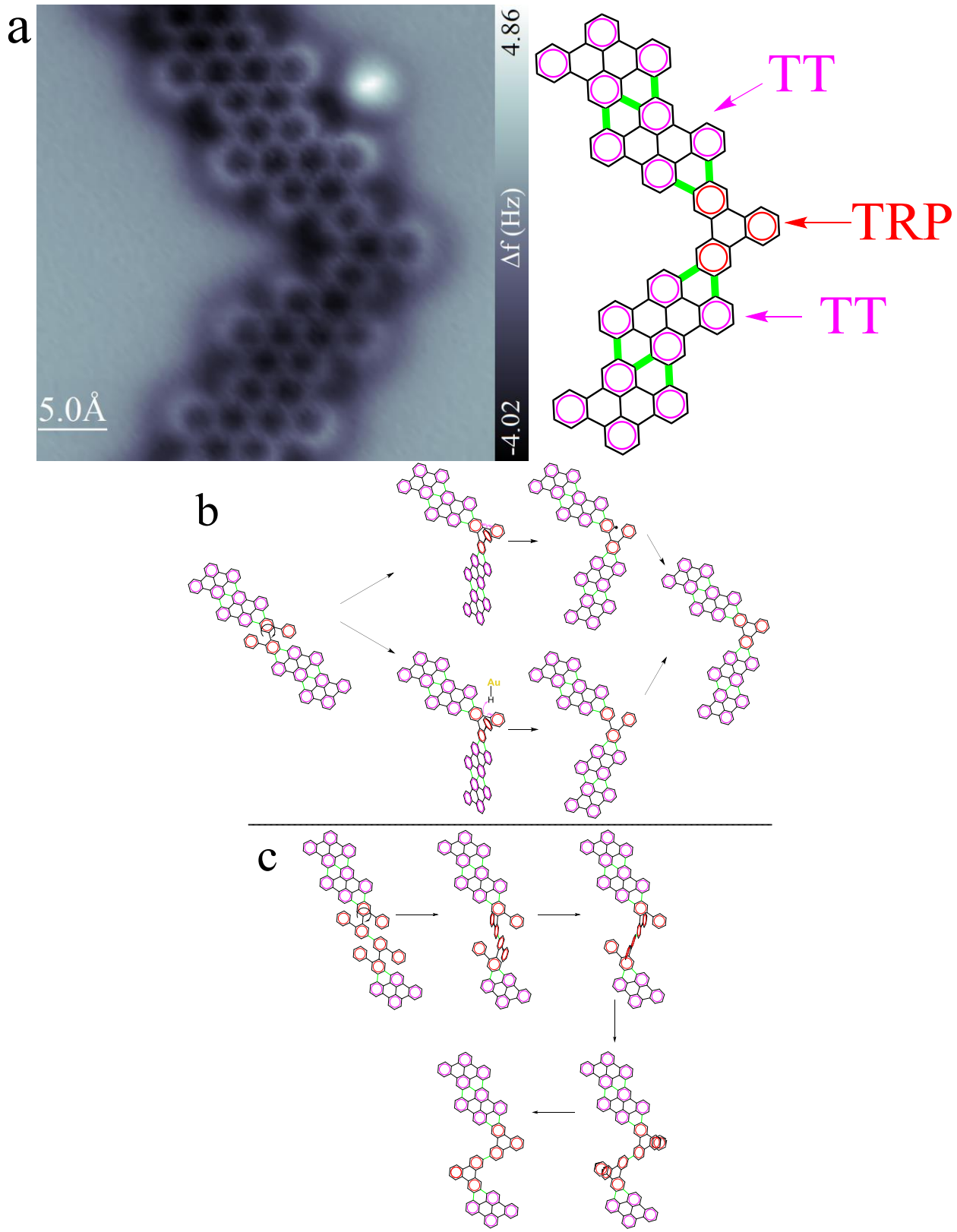

Scheme 5.6 GNR defect motif A. a) AFM image of defect A and chemical model. b) Two chemical pathways that lead to the loss of a phenyl ring, the upper one being homolytic and the lower one involving H transfer. c) Twisting motion involving two non-graphitized DBQP subunits.

Motif B. Just as motif A, the reaction mechanism shown in scheme 5.7b requires that the DBQP subunit at which the rotation event happens is located between two subunits that have cyclized. Secondary pathway of scheme 5.7c with rearrangement is proposed as an alternative, but this one requires multiple twists and not a single GNR that resembles the intermediary structures could be found.

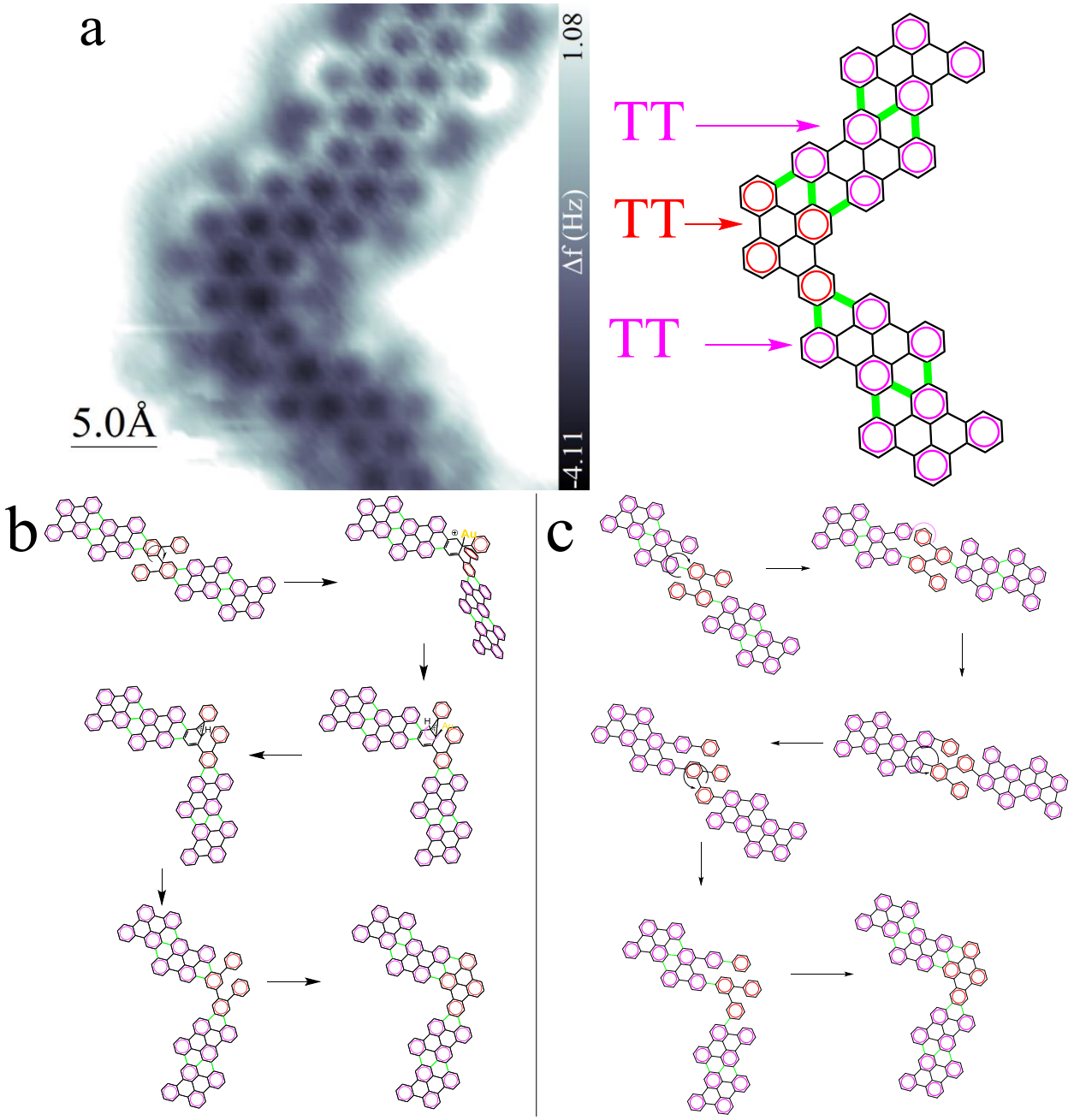

Scheme 5.7 GNR defect motif B. Defect with phenyl rearrangement. a) AFM image of defect B and its chemical model. Marked with red is the DBQP subunit that has undergone rearrangement. b) Single twist mechanism. c) Mechanism with 3 twists.

Motif C. As seen on the molecular model of AFM image of scheme 5.8a, a TRP moiety can be placed among complete TT moieties. In this defect the TRP moiety is not the sole means of contact between the two GNR segments.

The mechanism in scheme 5.8b depicts a GNR undergoing two twisting motions that generate structure C1, which corresponds to the imaged defect. It is worth to note that the first of these twisting events occurs at the bond in the middle of a DBQP subunit, and the second must happen at the bond between two different subunits.

An alternative mechanism seen in scheme 5.8c depicts the GNR segment that is twisting without the bond marked by the purple arrow. In this more flexible structure are depicted two twisting motions taking place at the same time. Such a mechanism could be explained by the lower interaction with either substrate or other polymers during the period of time in which the first twist takes place.

Finally, on scheme 5.8d we can see another way to arrange the TRP moiety. The retrosynthetic pathway leads to a structure in which only the section in the dotted box can be rationalized from a single g-GNR segment. The blue arrow indicates the C atom in which the Ullmann reaction should bind the two segments. Two more explanations would need that the segment in the dotted box was formed on the surface and eventually fused to the other segment and underwent a twisting motion at this new bond or simply fused in the manner in which it has been found.

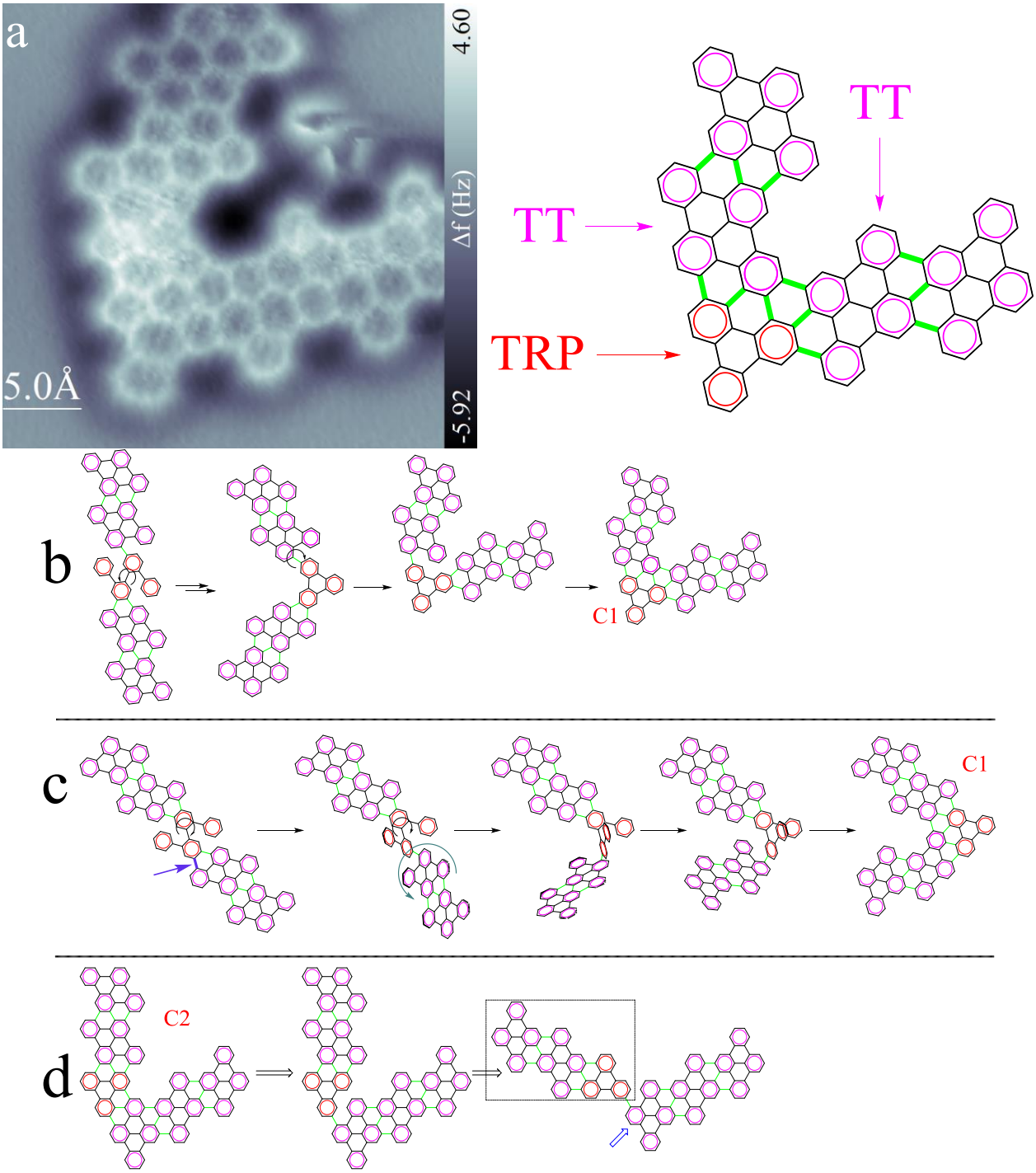

Scheme 5.8 GNR defect motif C. a) AFM image of defect C and its chemical model. b) This mechanism for motif C is considered to be the one that has taken place as can be rationalized from a single existing polymeric chain and requiring a single twist at the same defect. c) Similar to mechanism (*b*) it requires two twisting motions, d) Retrosynthetic pathway C2 cannot be rationalized from a single chain.

Motif D. This structure (scheme 5.9a) does not seem to be solely the result from a flipping event, rather it is the result of a rearrangement of the bonds of the chain or a linking between two g-GNR fragments. It is important to note that the second scenario would imply that the end of a well ordered g-GNR fused to a defect, but we never observed well preserved g-GNR end sections. Blue arrows indicate the Br positions in which the Ullmann products would bind.

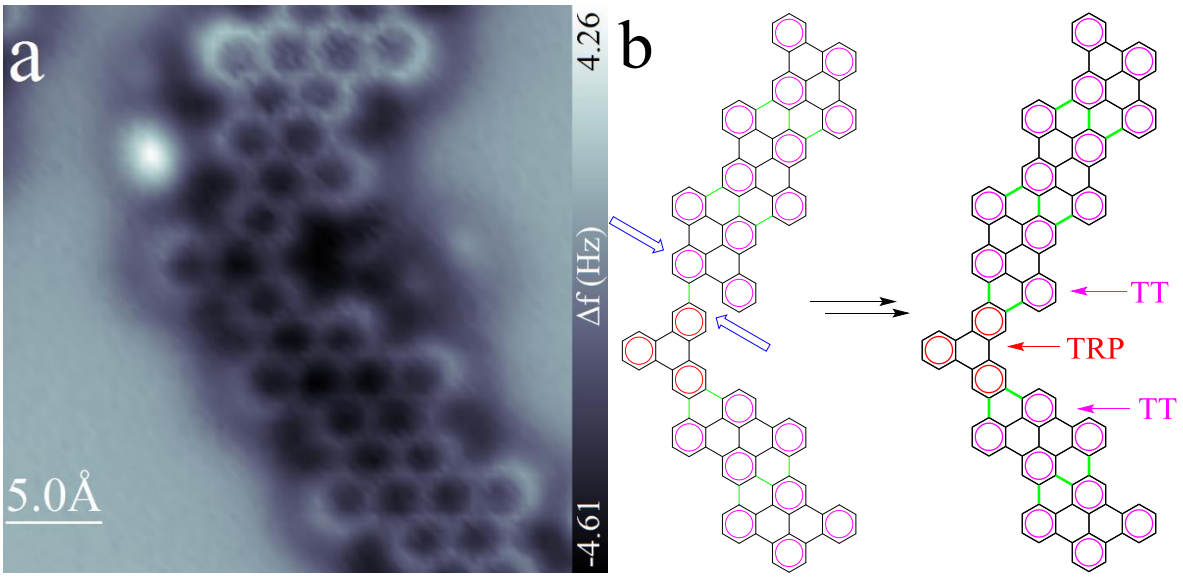

Scheme 5.9 GNR defect motif D. a) AFM image of defect D. b) Chemical model of motif D. The blue arrows point to the positions that would typically bind the two segments via Ullmann coupling.

Motif E. Multiple terphenyl structures were found to be coupled (figure 5.2a and 5.2b). These could be the result of broken DBQP subunits that eventually coalesced or the result of a flipping event at a section that is not flat, given the flexibility of such a chain that can result in the conditions favorable for the rings to overlap and have multiple C-C bonds break. Due to the ease of use of Universal Force Field[253] (UFF) in Avogadro[254], it was utilized to understand what can be expected of such an event (Section 5.5). The five adjacent DBQP subunits that have not planarized can overlap. Blue arrows indicate the position in which the bond between subunits should be when coming from the product of polymerization (figure 5.2c and figure 5.2d). A route similar to that depicted in scheme 5.6c is thought to have led to these polytriphenylene structures.

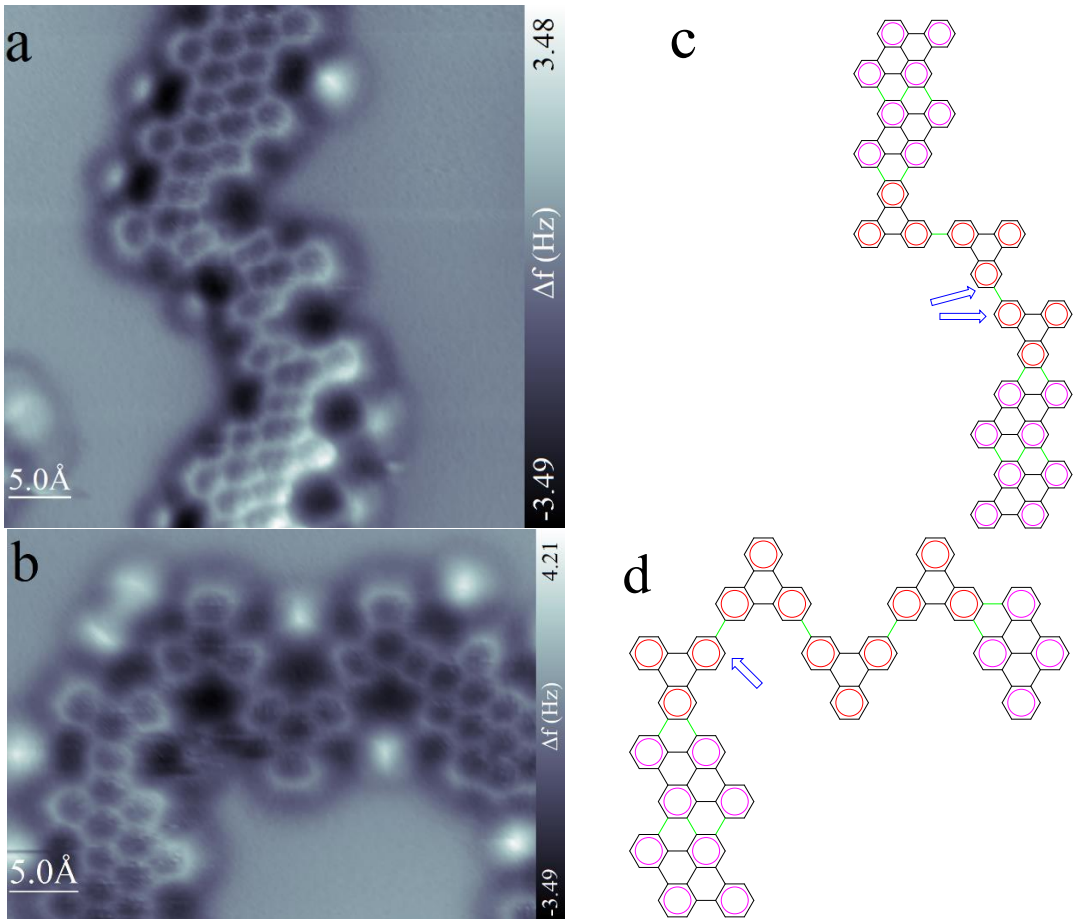

Figure 5.2 GNR defect motif E. a) and b) AFM images of two different sections with various terphenyls. c) and d) scheme of two terphenyl accumulations, the blue arrows indicate the C position where Br atoms where initially located.

Motif F. The structure (figure 5.3b) does not follow the alignment of a g-GNR product of the fusion of DBQP subunits, and the midsection did not bind through the C positions (blue arrows) that could have undergone an Ullmann reaction. A route similar to that depicted in scheme 5.6c is thought to have led to these polytriphenylene structures. In which the twisting motion took place at a position in which several monomers had not undergone the graphitization process.

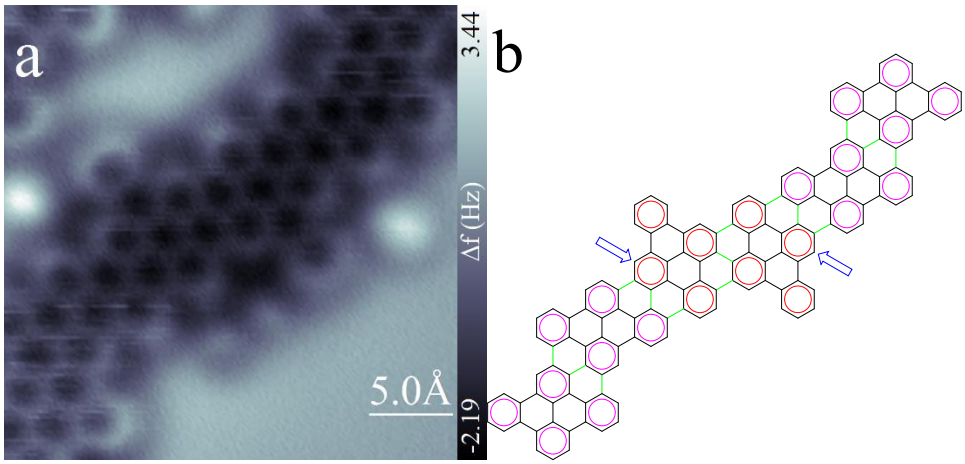

Figure 5.3 GNR motif F. Unlike the intended product which has a zig-zag edge, this section is of the armchair type. The blue arrows indicate the positions usually occupied by Br atoms. No mechanism could be rationalized.

Motif G. Literature on the decomposition of phenyl compounds indicates that rings rearrange resulting in larger polymers or in isomers[235]. We never observed GNR structures in which extra rings would be formed by an unknown carbon source or the presence of at least an extra carbon. Rather, we observed complete rings attached to the outer most position of the g-GNR (figure 5.4a), which further corroborates that in the previously described mechanisms we have C-C bond cleavage.

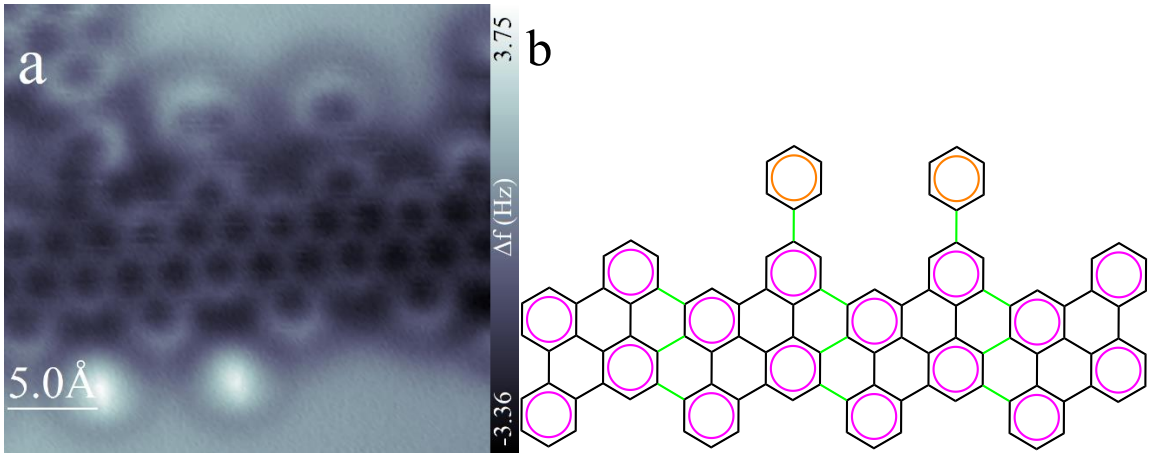

Figure 5.4 GNR defect G. a) AFM image of phenyl rings attached to the outer carbons of the rings that comprise a gulf. b) Chemical structure of defect G.

5.4 NPG Defects

Having analyzed the g-GNRs and the identified defects, we move to the NPGs. Only one defect of interest was found, in it, the 3 C atoms that comprise the outer edge seem to have migrated towards an adjacent ring, thus forming an indene moiety (figure 5.5b). The underlying mechanism might perhaps be understood to be similar to that of anthracene acidic isomerization to phenanthrene[255], but where in that isomerization the bonds that form and break result in a different arrangement of three adjacent benzene rings. In here we observe that a carbon favored the loss of an H atom and bonded to 3 carbons which also requires the loss of aromaticity. Though we cannot fully rationalize the presence of this structure, we find interesting that once more the structure found is comprised by a migration of elements already present in the previous stages.

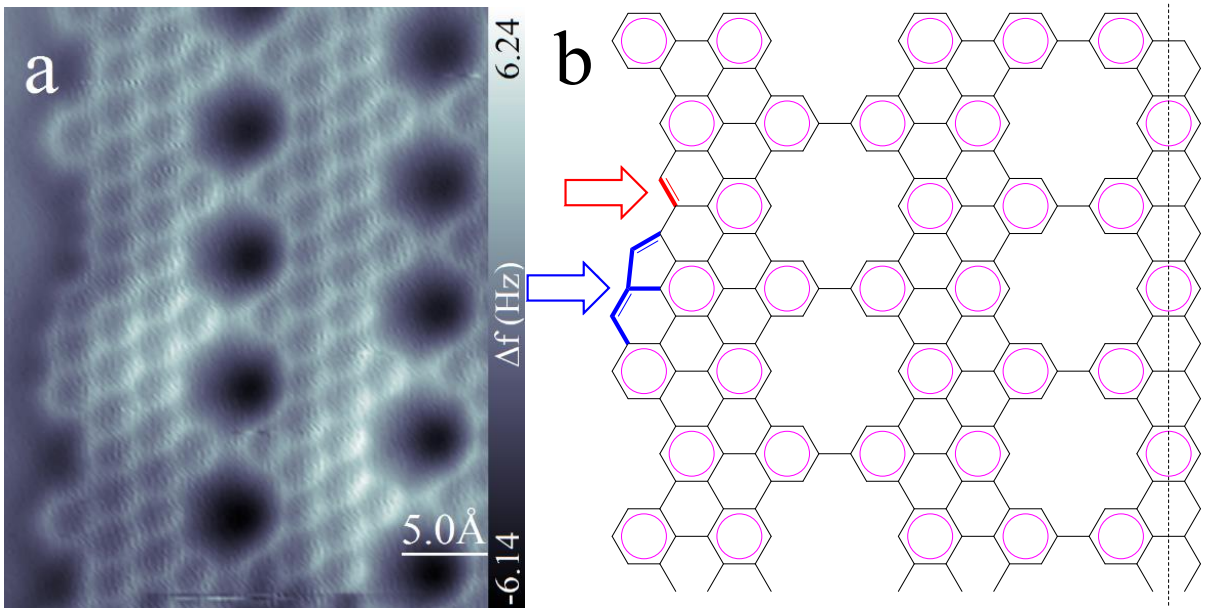

Figure 5.5 NPG defect. a) AFM image of NPG with a defect on the outer edge. b) Drawing of the same NPG, marked with a red arrow is a double bond and marked with blue arrow the section that is comprised by 2 rings normally not seen

5.5 The Twisting Motion at the Oligomeric Stage

As stated before, the measured length between phenyl rings averages that of the reported lengths measured from X-ray crystallography of *meta*-terphenyl molecules (chapter 4.2, figure 4.1). As such, it is considered that the twisting motion comes at the oligomer stage, not at an organometallic one. Previous reports on *meta*-linked polyphenyl molecules indicate that such an event is energetically unfavorable[210], with in-plane rotation at the labile organometallic stage being

the favored mechanism. Our results suggest that what they claim in reference 210 for DMTP does not hold for the DBQP case. This behavior is better understood by considering a partial desorption of the oligomer, with segments of said oligomer reaching the vacuum and entering a state similar to a gas phase. This is not unlike what has been theorized of alkanes on graphite[256, 257]. Other macromolecules that are mostly planar have been reported to desorb from Au(111). For example, for porphines desorption can be observed at 623 K (350 °C)[63], and 5,15-diphenylporphyrins desorbs at 383 K (110 °C)[258]. From these two examples we can see that the planar structure desorbs at higher temperatures even though it has a higher mass. This difference may be attributed to the non-planar structure of the molecules equipped with tilted terminal groups which reduces interaction to the substrate. Similarly, at the oligomeric stage we can see that the phenyl groups labeled as 1 are in a tilted position with respect to the substrate.

To help visualize the motion of the partially dehydrogenated DBQP oligomers, two models were made making use of UFF[253]. The first is a trimer on Au(111) (figure 5.6). The central DBQP subunit is partially dehydrogenated and allows the movement around the single bond between the two phenyl rings. In this images we can observe how a phenyl ring approaches the surface as the structure rotates and ends under the phenyl ring of the subunit that did not separate from the slab.

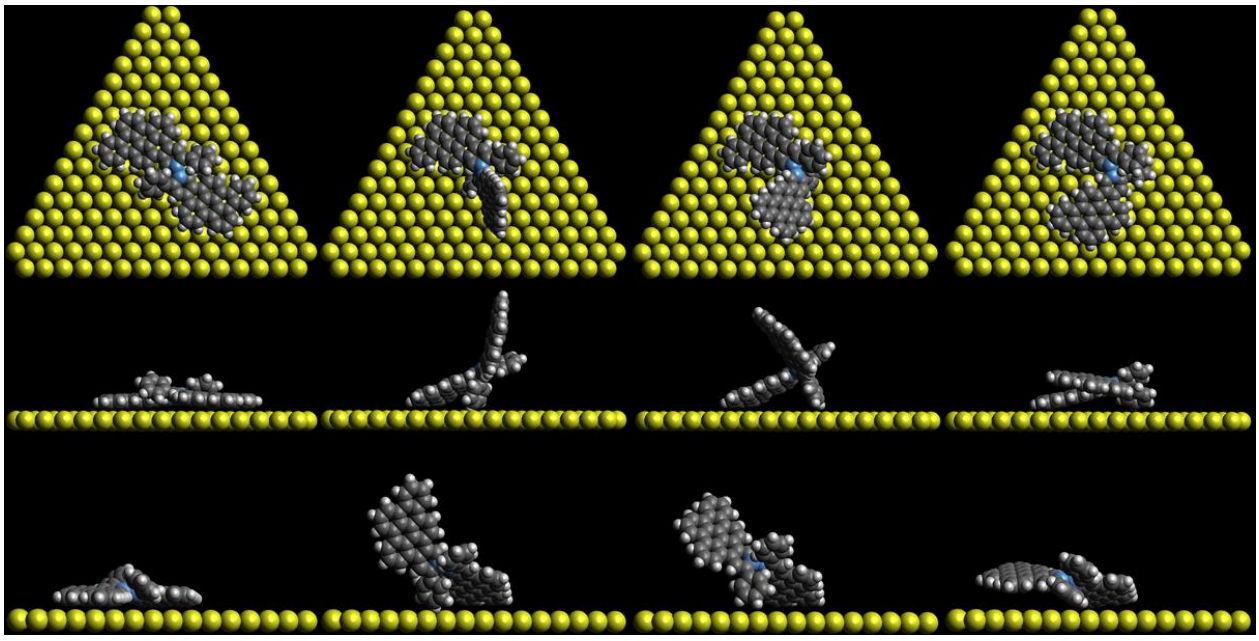

Figure 5.6 GNR twist motion. The sequence of events in the depicted twist motion is from left to right. The upper images are the top view, the mid and lower images are side views. Depicted in blue are the C atoms at which the structure rotates. Images produced by "fixing in place" the atoms of the Au(111) slab. Part of the structure is sequentially rotated and optimized at every step.

The second 3D model (figure 5.7c) is a chain of eleven DBQP subunits, in which a partially dehydrogenated DBQP is located between two that are fully graphitized (red and black respectively in figure 5.7a, and figure 5.7b). In this model the far left segment was modeled restricting lateral and vertical movements but allowing flexibility at the immediate partially graphitized DBQP. In this progression of images we can observe the vertical movement at the partially dehydrogenated central DBQP subunit. As the structure lifts up, the single bonds between the four segments serve as pivots, allowing for rotation. Of notoriety is that as the event progresses two phenyl groups accommodate beneath another and segment 4 has also been displaced but the direction has been preserved. A comparison can be made to a simple machine such as a slider crank, in which the larger segment, relative to the rotation center, planarized or otherwise, serves as anchor. The single bonds between the still non-dehydrogenated phenyl rings work as pivots and every segment as a connecting rod. Such scenario matches the description proposed for linear alkanes, in which segments attach and detach from the substrate[256, 257].

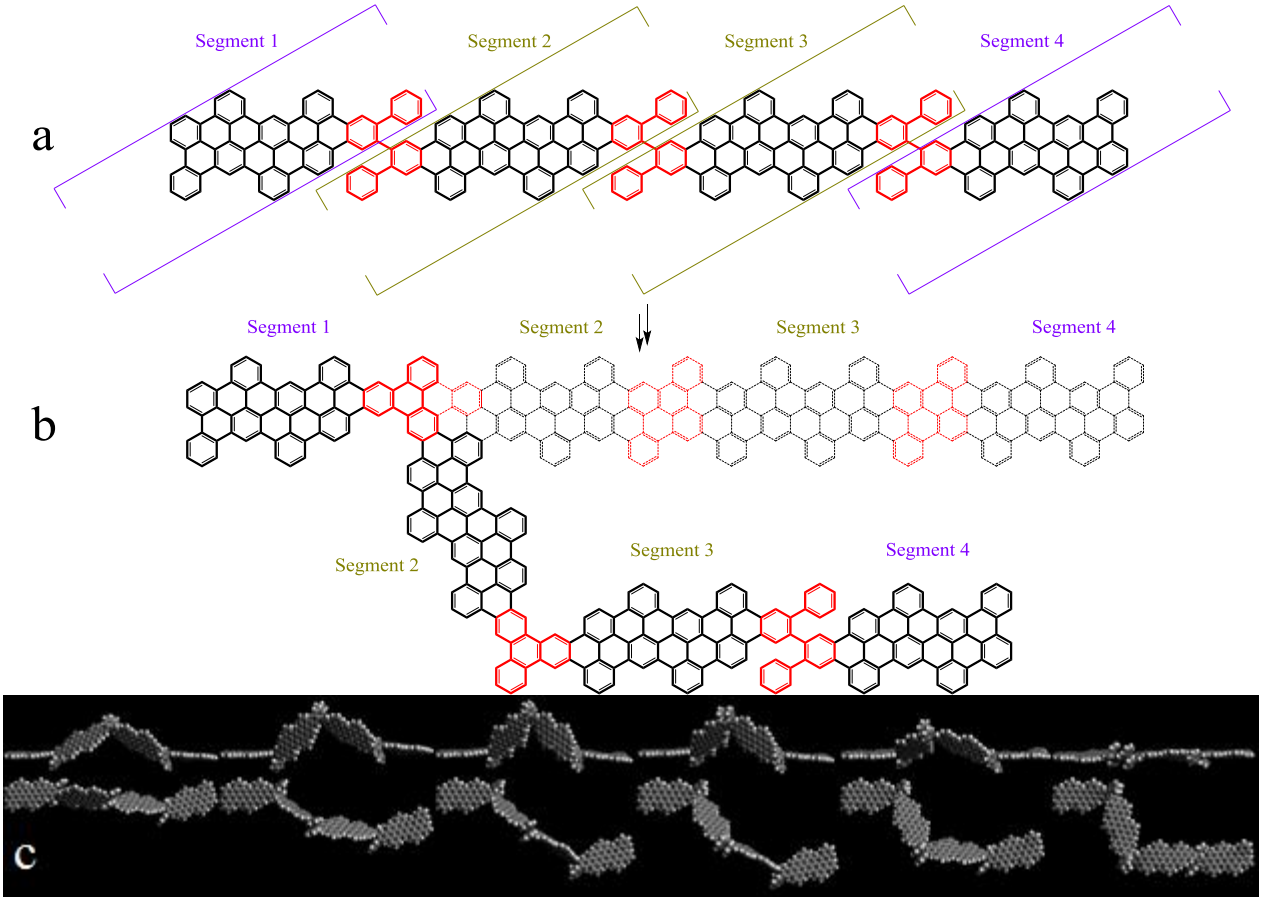

Figure 5.7 Lifting motion at a single point of a partially dehydrogenated GNR. a) Partially dehydrogenated GNR, comprised by eleven DBQP subunits, 3 of which are partially dehydrogenated (colored red), and dividing the structure in 4 segments. b) Same GNR after the twisting motion at two single bonds. Doted structure indicates the position the GNR would occupy had the twist not taken place. c) Side view and upper view of the 3D model of the same GNR structure at various stages of the twisting motion.

5.6 On-Surface Dehydrogenation and Scholl Reaction

We attribute the elimination and rearrangements to mechanical stress and steric hindrance that occurs with the overlapping of phenyl rings, as defects were only observed at the previously described elbows of the GNRs, and never in straight sections such as those of figure 5.8. The presence of a TRP moiety in a structure such as the one in figure 5.8a could be possible if the sole factor for elimination is the activation of the C-C bond by the Au(111) substrate. Rearrangements such as those of figure 5.8b should also exist if the only conditions were the presence of H atoms and/or Au activation of C-C bonds[245].

In published reviews of the Scholl reaction, the on-surface dehydrogenation of oligomers of GNR precursors has been equated to it[72, 259]. However, it is also stated that the Scholl reaction mechanism is not totally understood[72, 259, 260], and neither are all the factors involved in the various published rearrangements. In literature we found no reference of elimination of phenyl groups via Scholl reaction/oxidative coupling, with the sole exception being the report of decomposition of terphenyls in reference 235.

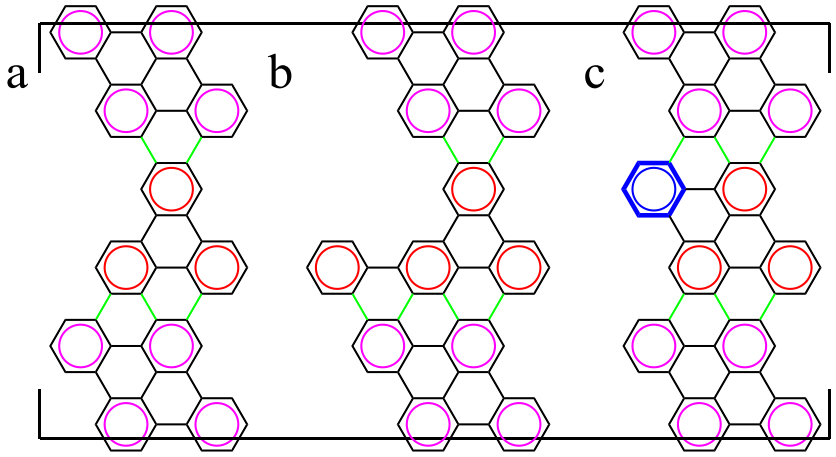

Figure 5.8 DBQP dehydrogenated polymer with a missing phenyl ring. a) GNR with a missing benzene ring. b) Straight GNR in which a phenyl ring underwent a [1,2] migration. c) GNR with the benzene ring marked in blue for comparison.

5.7 Summary and Outlook

In the following, the main conclusions are presented point by point.

(i) Characterization of the various motifs that resulted as side reactions of the process of graphitization of the DBQP oligomers. The chemical structures of seven types of GNR structural defect motifs were identified based on nc-AFM images, as well as a skeletal rearrangement of three C in a NPG edge.

(ii) Chemical reaction pathways were rationalized for the reactions of elimination and rearrangement of phenyl groups with which defect motifs can be explained.

(iii) The sample disorder at the graphitized stage was rationalized by the partial desorption and readsorption of the DBQP oligomer chain with subsequent dehydrogenation.

In order to better understand the chemistry behind the cleavage and migration of phenyl rings future experiments could employ other conditions such as:

(i) Lower coverage as to ensure the identification of isolated oligomer chains so that the effect of the twisting motion can better be understood.

(ii) Lower annealing temperatures of the graphitization state as to possibly locate sections that have twisted, but not yet planarized.

(iii) Effect of other gases that may increase the pressure. In the few images presented in the work of Kojima[50] few if any defects are present. A reason for this could be that the higher pressure prevented the oligomers from desorbing from the substrate.

With the myriad of possible overlapping structures that can possibly be created it is then important to understand why some are more prevalent than others, this information can then be used to tailor GNR precursors to improve synthesis GNR or to change the skeletal structure as to help understand the chemistry (e.g. use of methoxy groups)[241].

There are 3 polyphenyl molecules with a *meta* linkage that have been used to create GNR with gulf-type edges, DBQP[50], dibromo-sexiphenyl (DBSP)[50, 252] and dibromo-octaphenyl (DBOP)[261]. Of these, the first two have proven to form GNR with the third one failing to polymerize. To expand the information on gulf-type GNRs and the NPG structures that result from their fusion, DBSP can be utilized to continue this line of research.

In this work it is being proven that at low concentrations the polymer can undergo several types of reactions. If the described mechanisms are proven true, certain parallelisms can be made to the RNA cleavage[262] process, in which a natural polymer undergoes self-catalysis with the use of metal ions.

Chapter 6 Conclusions and Perspectives

In this work we were demonstrating the successful bottom-up on-surface synthesis and characterization of three types of macromolecules, namely porphine square tetramers (free-base and its zinc functionalized derivative), g-GNR and NPG. The characterization was performed with low temperature SPM tools providing high resolution. Structural characterization via STM and nc-AFM, characterization of electronic properties was done by means of STS.

The dehydrogenative homocoupling of porphines was exploited to synthetize covalent nano-architectures of regular structure. Coexisting with oligomers of various sizes we achieved for the first time the square-like tetramers. Lateral manipulation was complimentary to the imaging procedures, as a means to test structural integrity of the covalent bonds between the porphine macrocycles. Two species of porphine monomers were utilized, a free-base and a zinc metalated derivative. The dI/dV maps reveal no differences in the low energy electronic structure between the two species as predicted by DFT calculations. Even though there is no charge transfer from the Ag(100) substrate and the two types of tetramers, these display asymmetric charge distributions. Calculations predict that the COT moiety has antiaromatic character for both highly symmetric 8H-P tautomers, while the periphery shows a complete different behavior, with the $T_{\times}$ tautomer being aromatic at the corners and tautomer $T_{\diamond}$ having an outer aromatic pathway of 60 electrons.

A protocol to obtain g-GNR and NPG from DBQP in UHV conditions was established. A comprehensive structural characterization was performed not only for g-GNR and NPG, it was also carried out for the oligomer stage. The dehydrogenation of the DBQP oligomers to obtain g-GNR results in many defects. To improve the synthesis of NPG, the coverage at the oligomer stage has to increase to reduce the probability of generating defects during the dehydrogenation. Even then the yield is low. The electronic properties of g-GNR: wide bandgap semiconductor (2.8 eV). The dI/dV maps are well understood with DFT simulations of the spatial distribution of the electron probability density. The electronic properties of NPG: wide bandgap (2.7 eV), the VB is pinned at -1 V. The dI/dV maps are correctly understood again with DFT simulations. The high conductance features observed in g-GNR gulfs and NPG pores in the unoccupied region originate from the different conduction bands. It is unlikely that they originate from IPS or SAMO states, as has been recently suggested in references 53 and 226.

We performed the atomic-scale structural characterization of seven distinct defects that result from the graphitization of the DBQP oligomers. Chemical reaction pathways were rationalized in order to explain how the defects came to be. These can be relevant to tailor GNR precursors to improve the synthesis of GNR, additionally other precursors may help to better understand our findings. We currently consider a partial desorption of the oligomers to be the root of the problem, further experiments were proposed to test this assumption.

In order to improve our knowledge of g-GNRs and NPGs, other precursors could be employed in further experiments. The precursor dibromo-sexiphenyl (DBSP)[50, 252] has been employed successfully for the synthesis of g-GNR.

List of Publications

Riss, A.; Richter, M.; Perez Paz, A.; Wang, X.; Raju, R.; He, Y.; Ducke, J.; Corral, E.; Seufert, K.; Garnica, M.; Rubio, A.; Barth, J. V.; Narita, A.; Müllen. K.; Berger, R.; Feng, X.; Palma, C.; Auwärter, W. Polycyclic aromatic chains on metals and insulating layers by repetitive [3+2] cycloadditions. *Nat Commun*. **2020**. 11, 1490.

Cao, N.; Riss, A.; Corral-Rascon, E.; Meindl, A.; Auwärter, W.; Senge, M. O.; Ebrahimi, M.; Barth, J. V. Surface-confined formation of conjugated porphyrin-based nanostructures on Ag(111). *Nanoscale*. **2021**. 13, 19884.

Cao, N.; Björk, J.; Corral, E.; Chen, Z.; Ruben, M.; Senge, M.; Barth, J. V. Riss, A. The role of aromaticity in the cyclization and polymerization of alkyne-substituted porphyrins on Au(111). *Submitted*

Corral-Rascon, E.; Riss, A.; Matěj, A.; Wiengarten, A.; Mutombo, P.; Soler, D.; Jelinek, P.; Auwärter, W. On-Surface Synthesis of Square–Type Porphyrin Tetramers with Central Antiaromatic Cyclooctatetraene Moiety. *Submitted*

Piquero-Zulaica, I.; Corral-Rascon, E.; De Cerio, X.; Riss, A.; Garcia-Lekue, A.; Kherelden, M.; El-Fattah, Z. M. A.; Patel.; K.; Kojima, T.; Seufert, K.; Sakaguchi, H.; Auwärter, W.; Barth, J. V. Molecular-Orbital Decay Induced Edge and Pore States in Nanoribbons and Nanoporous graphene Structures. *In preparation*

Appendix

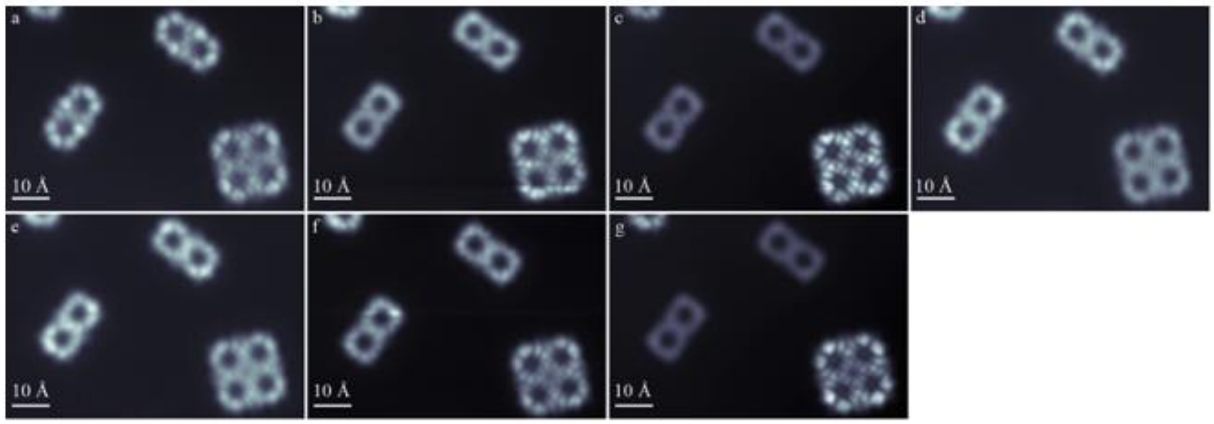

Figure A1. 4Zn-P tetramer dI/dV maps at different bias voltages. The bias values used when recording these images are as follows, a) -700 mV, b) -150 mV, c) -50 mV, d) 50 mV, e) 150 mV, f) 250 mV, g) 350 mV. The top panels include both a tetramer and dimers for comparison. The bottom panels show enlarged images of the tetramer only.

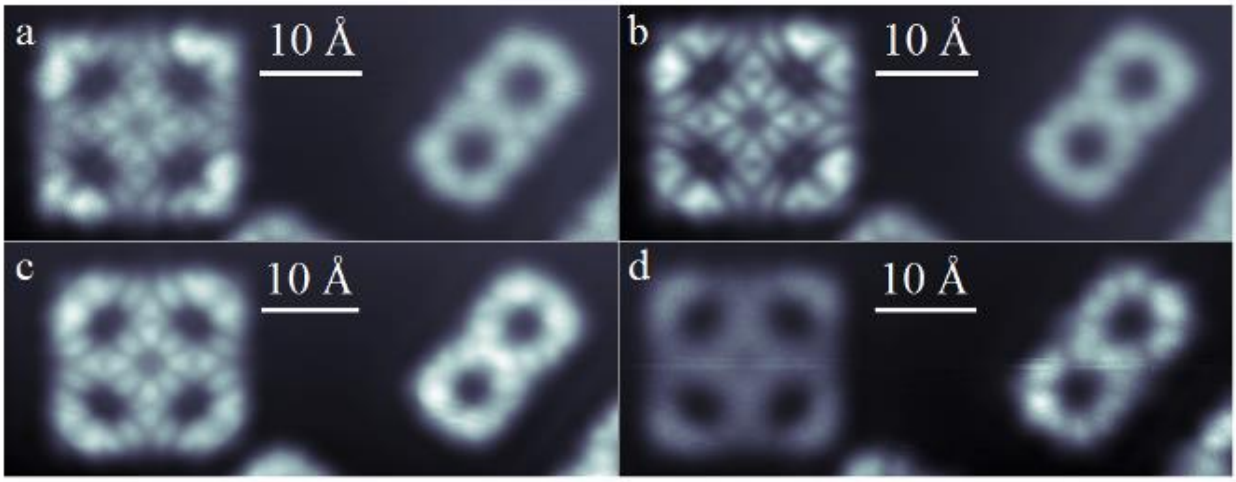

Figure A2. 8H-P tetramer dI/dV maps. The bias values used when recording these images are as follows, a) -250 mV, b) -50 mV, c) 50 mV, d) 250mV. The top panels include both a tetramer and a dimer for comparison. The bottom panels show enlarged images of the tetramer only.

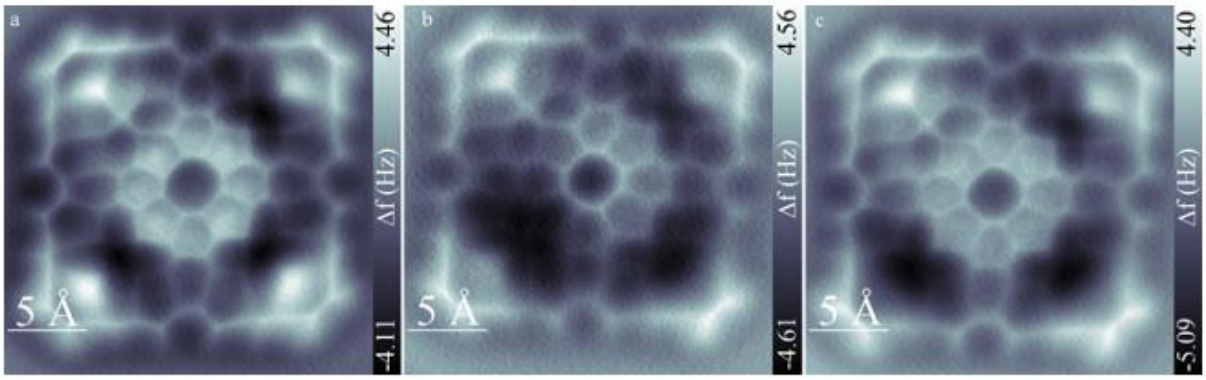

Figure A3. 8H-P tetramer after voltage pulse. a) AFM image of a pristine tetramer, b) and c) AFM image of the same tetramer after applying a series of voltage pulses. Note the contrast modification in rings 1 and 3.

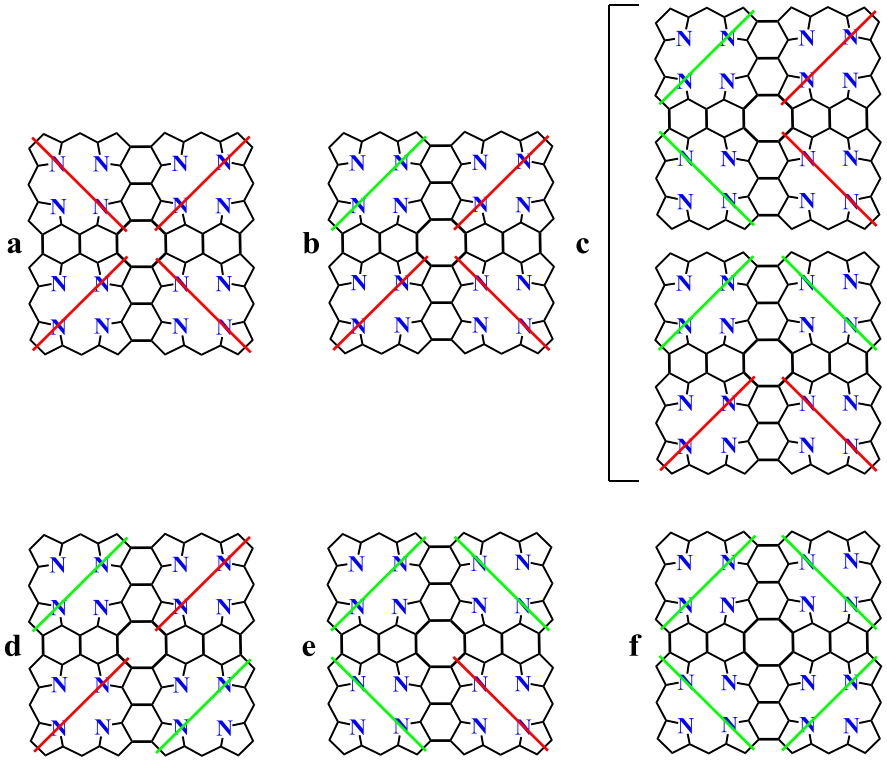

Figure A4. Possible tautomers of 8H-P. Green and red lines represent the positions of the inner H atoms. In the depicted structures the H atoms are shifted one monomer at a time. a) and f) Corresponding to structures $T_{\times}$ and $T_{\diamond}$. b) and e) There are in total four of each of these tautomers. c) After an initial shift from one monomer, which can be equivalent to structures b) or e), a contiguous monomer can shift resulting in a product equivalent those shown. Two more equivalent structures exist. d) Similar to the previous case, the monomer opposite to that which has changed can shift. One more equivalent tautomer exist.

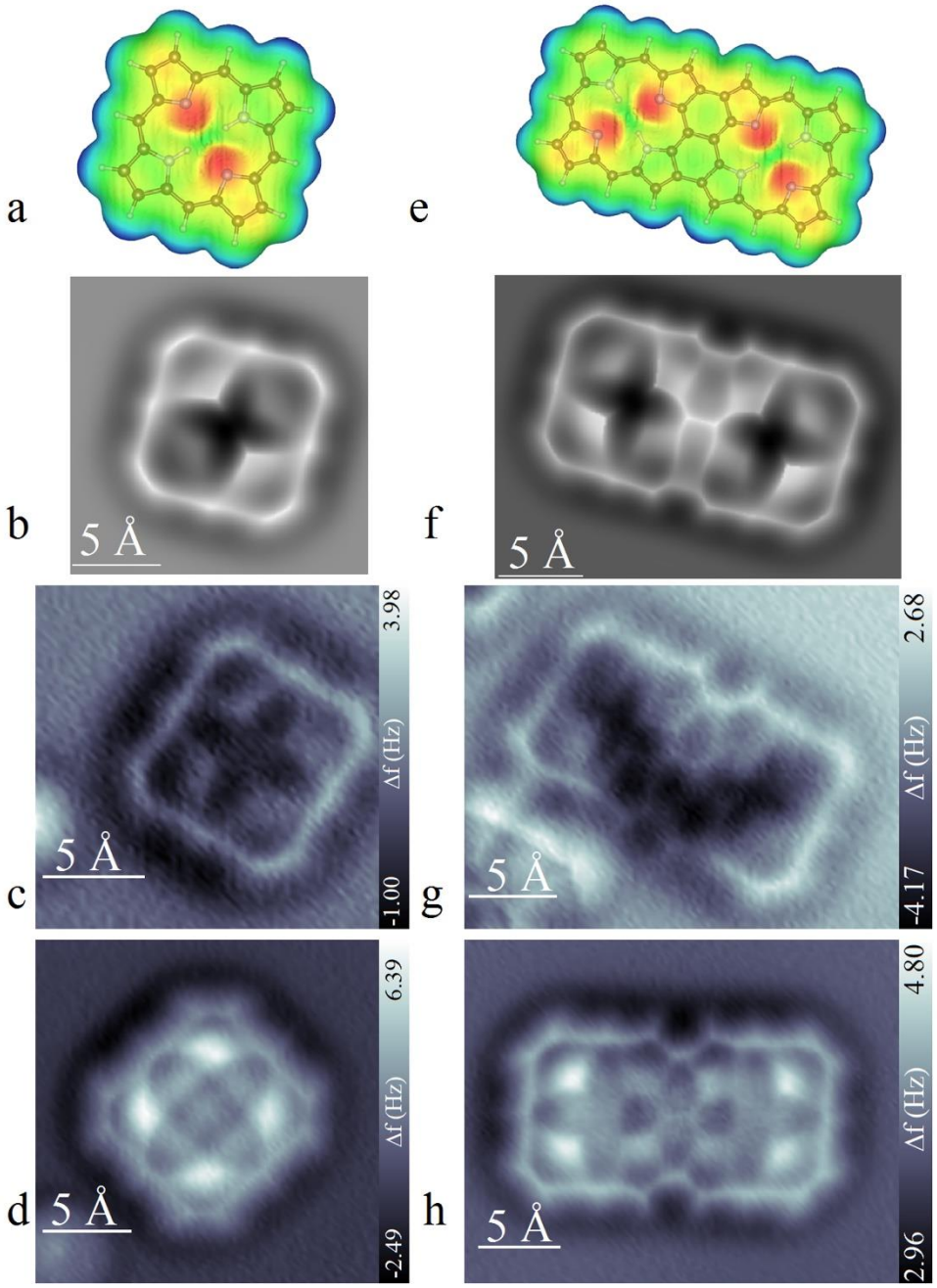

Figure A5. 2H-P monomer and 4H-P dimer electrostatic map, simulated AFM image and experimental AFM images. a), and e) electrostatic maps. b), and f) Simulated AFM images with CO tip with charge of -1. Note the two-fold symmetry in each porphine unit induced by the position of the inner hydrogen pair in the theoretical data, reminiscent of the "V-like" contrast in the bottom right experimental AFM image of a dimer. c), d), g), and h) experimental AFM images.

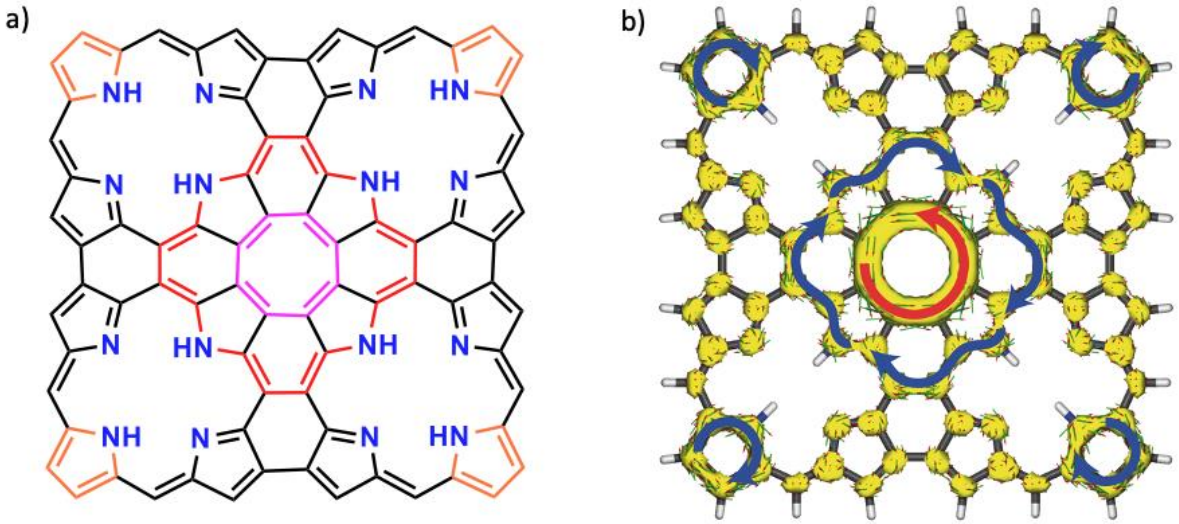

Figure A6. Structure and ACID for the T× 8H-P Tetramer. Three delocalization pathways can be derived from the ACID plot. Inner antiaromatic COT (purple), aromatic tetraaza[8]circulene outer rim (red), and aromatic outer corner pyrrole (orange).

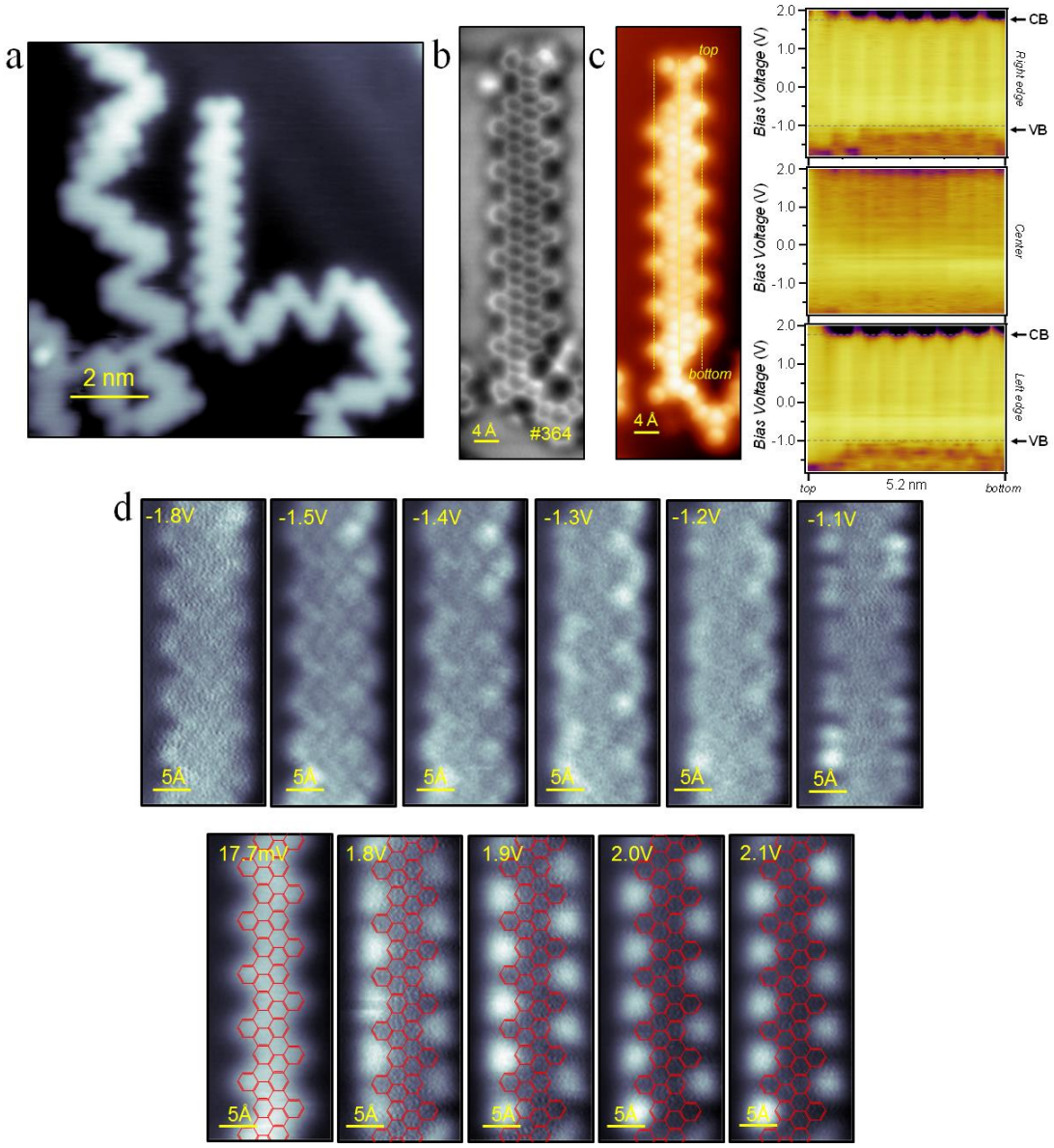

Figure A7. Electronic properties of a six-unit. a) Overview STM image (50 mV, 12 pA), with a g-GNR segment surrounded by defective GNR segments. b) nc-AFM image of the g-GNR segment highlighting its well-defined structure and triphenylene terminations at both sides. c) br-STM image (8.3 mV) and LDOS intensity maps of line dI/dV point spectra acquired at both edges and center of the g-GNR (2 V_{onset}, 100 pA). The onsets of VB and CB can be clearly identified and a 2.8 V wide bandgap is obtained. d) Set of dI/dV maps acquired for VBs, within the gap and CBs.

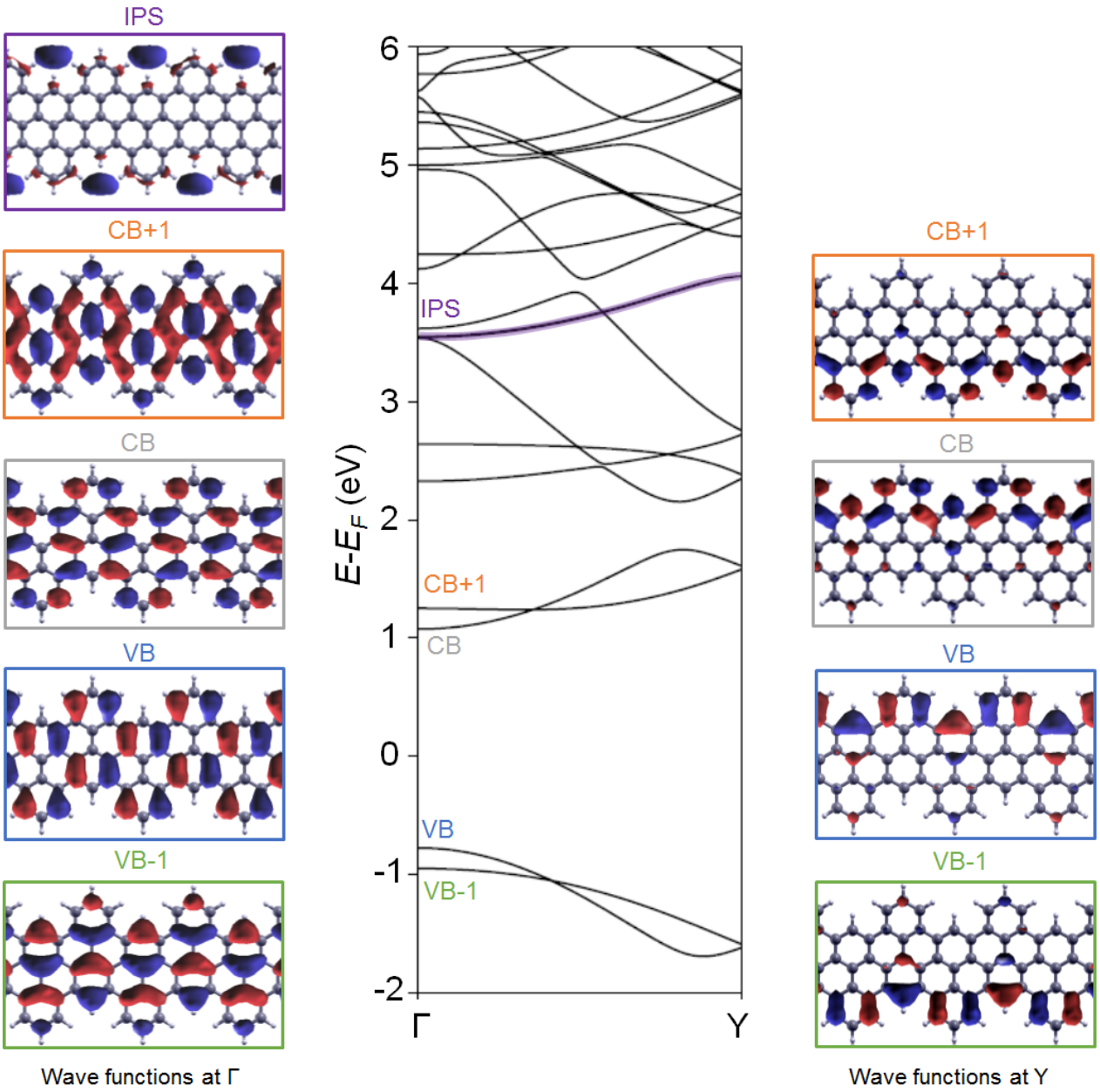

Figure A8. DFT calculated band structure for the g-GNR showing dispersive and braiding VBs and CBs and a semiconducting gap of 1.84 eV. Image potential states (IPS) are identified at higher energies. Such free electron-like IPS are confined at the vacuum side along the g-GNR edge. Frontier molecular orbitals for VB-1, VB, CB and CB+1 extracted at the Γ and Y points and molecular orbitals for the IPS extracted at the Γ point. The IPS is the only one that shows wave functions intrinsically confined at the gulfs.

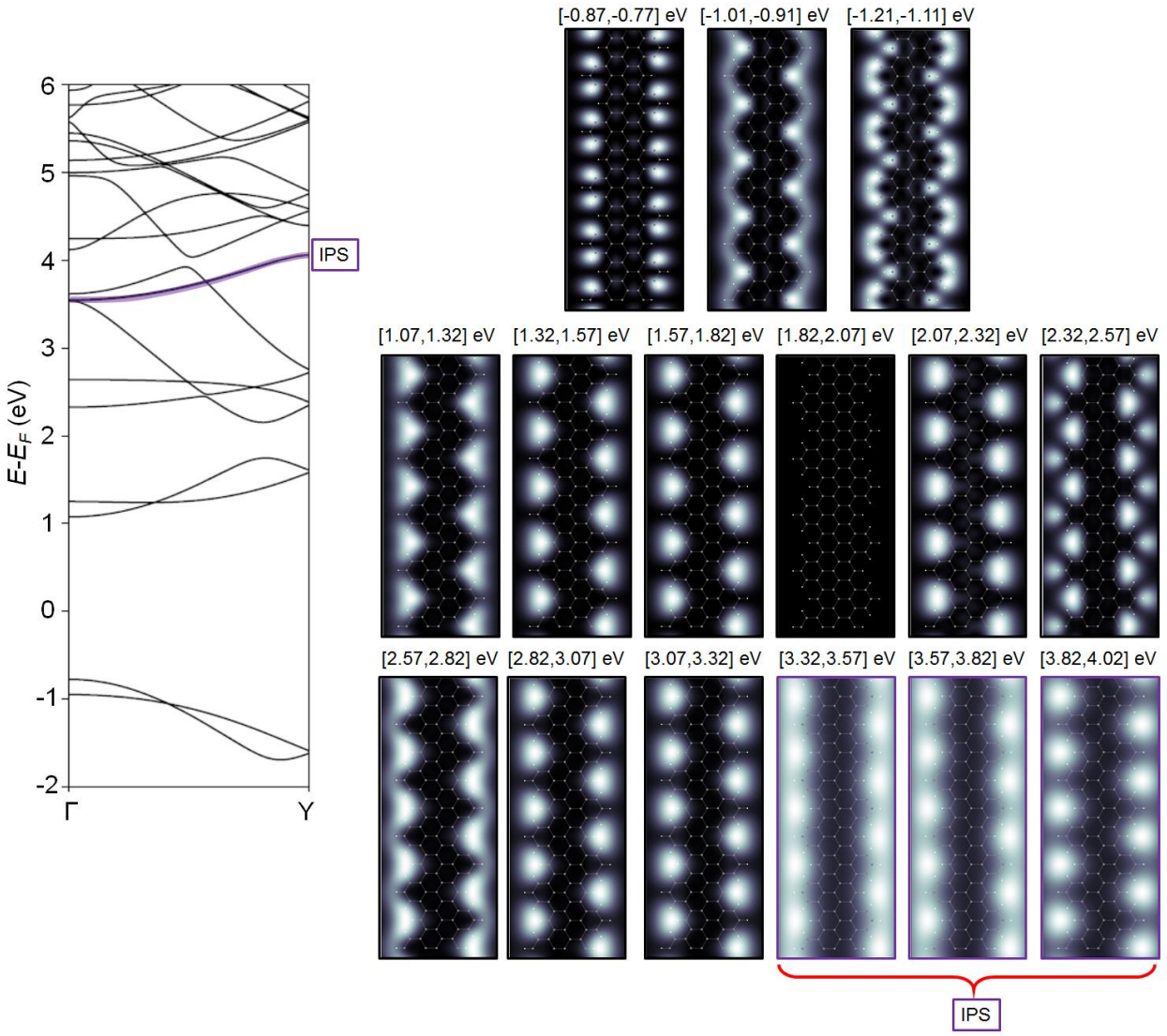

Figure A9. DFT spatial distribution of the electron probability density of the g-GNRs extracted at a height of z=5 Å. An energy integration of 100 meV and 250 meV is chosen for occupied and unoccupied states respectively. The VBs show conductance features localized at the phenyl rings (appearing as two dots) and winding along the edges. All the CBs show conductance features confined at the gulf regions, which resemble the conductance features of IPS.

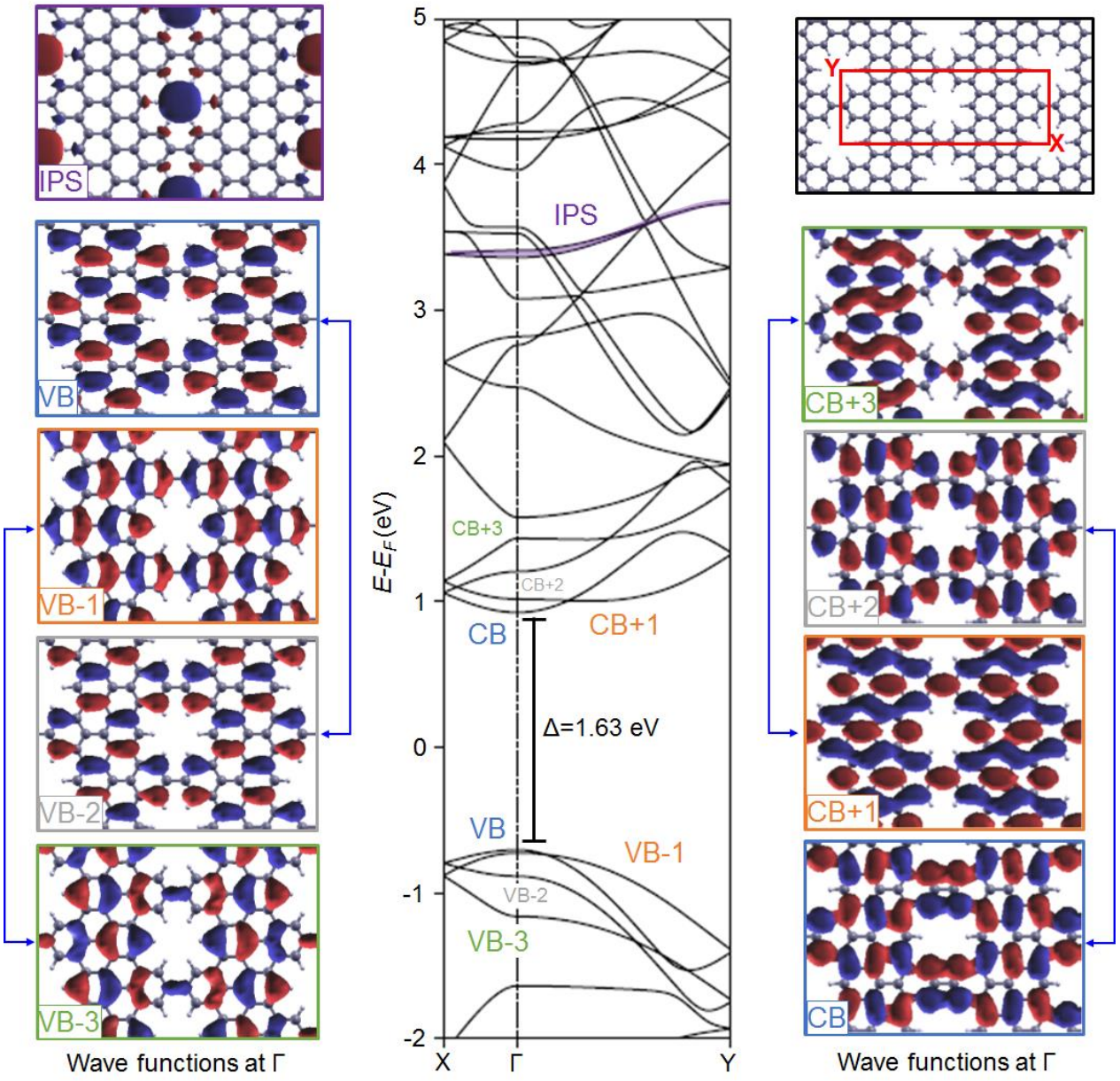

Figure A10. DFT calculated band structures for the NPG showing dispersive VBs and CBs in both longitudinal and transversal directions (i.e., ΓY and ΓX directions) and a semiconducting gap of 1.63 eV. Frontier molecular orbitals, i.e., VB-3, VB-2, VB-1, VB, CB, CB+1, CB+2 and CB+3, as well as IPS extracted at the Γ point. Bonding and antibonding states are clearly observable at the bridge positions (g-GNRs fusing point). The IPS orbitals are the only ones that appear intrinsically confined at the nanopores.

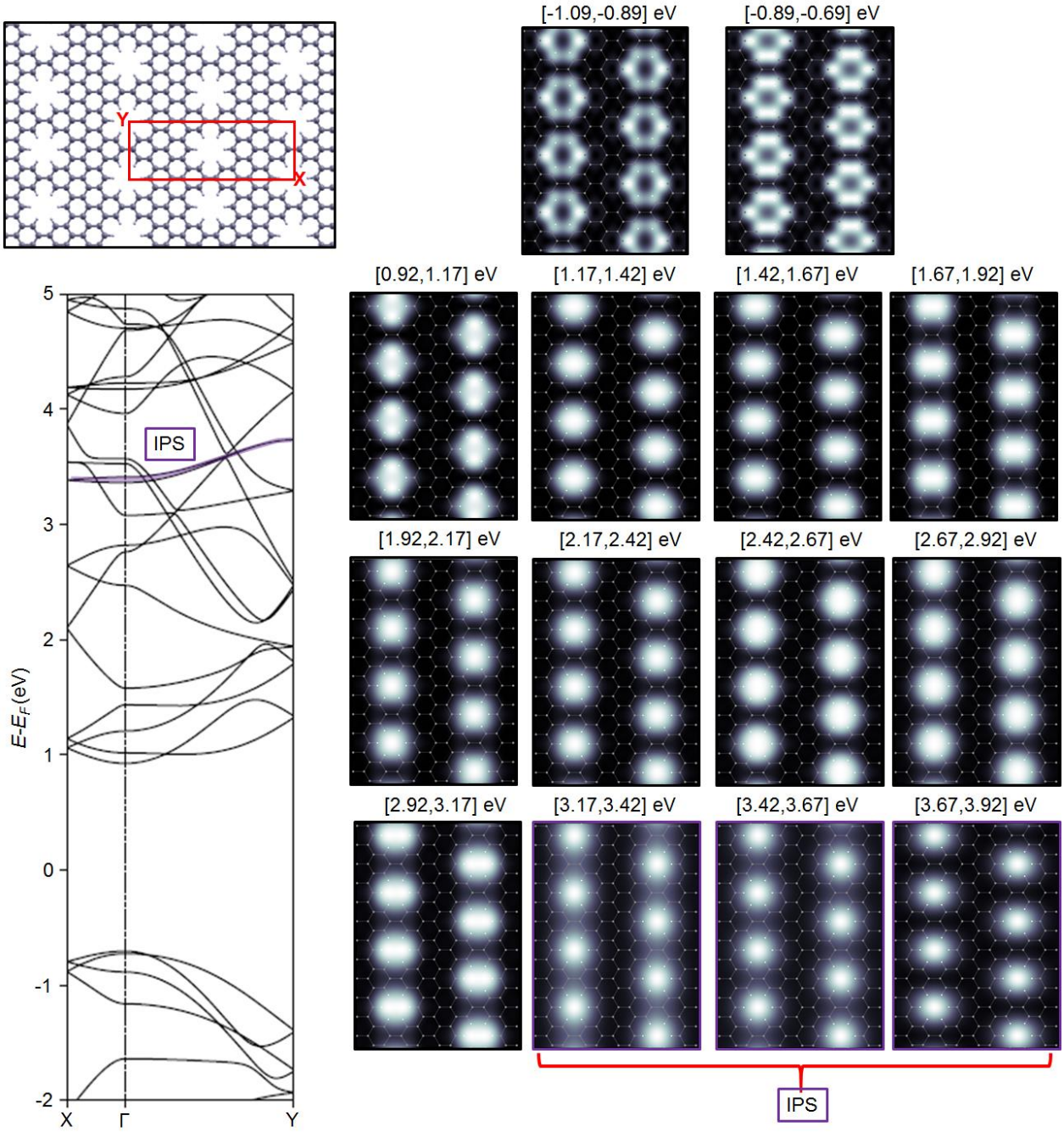

Figure A11. DFT spatial distribution of the electron probability density of the NPGs extracted at a height of z=5 Å. An energy integration of 200 meV and 250 meV is chosen for occupied and unoccupied states respectively. The VBs show conductance features localized around the nanopores (appearing as hexagonal rings). All the CBs show conductance features confined at the nanopores, which strongly resemble the conductance features of IPS.

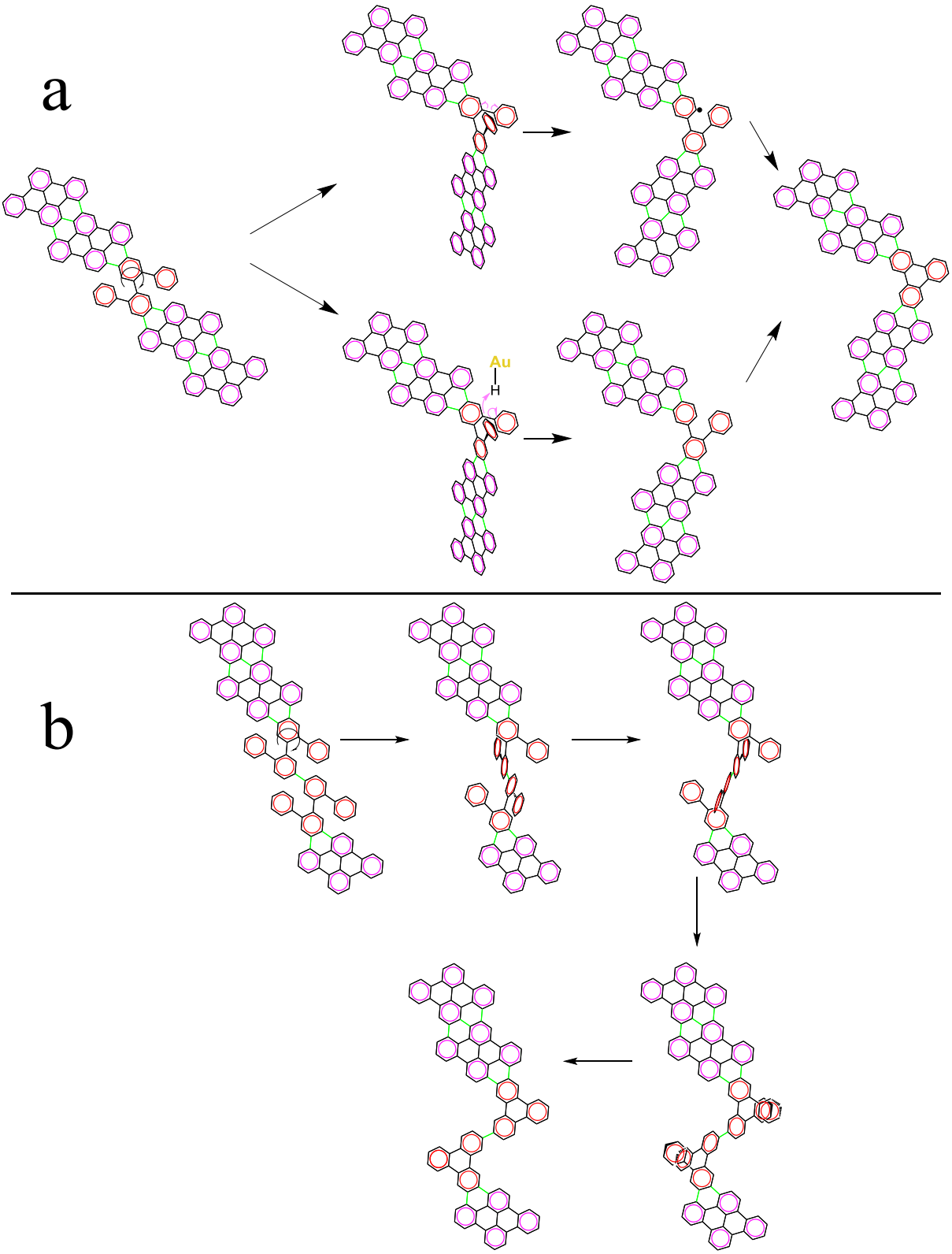

Figure A12. GNR defect motif A. a) Two chemical pathways that lead to the loss of a phenyl ring, the upper one being homolytic and the lower one involving H transfer. b) Twisting motion involving two non-graphitized DBQP subunits.

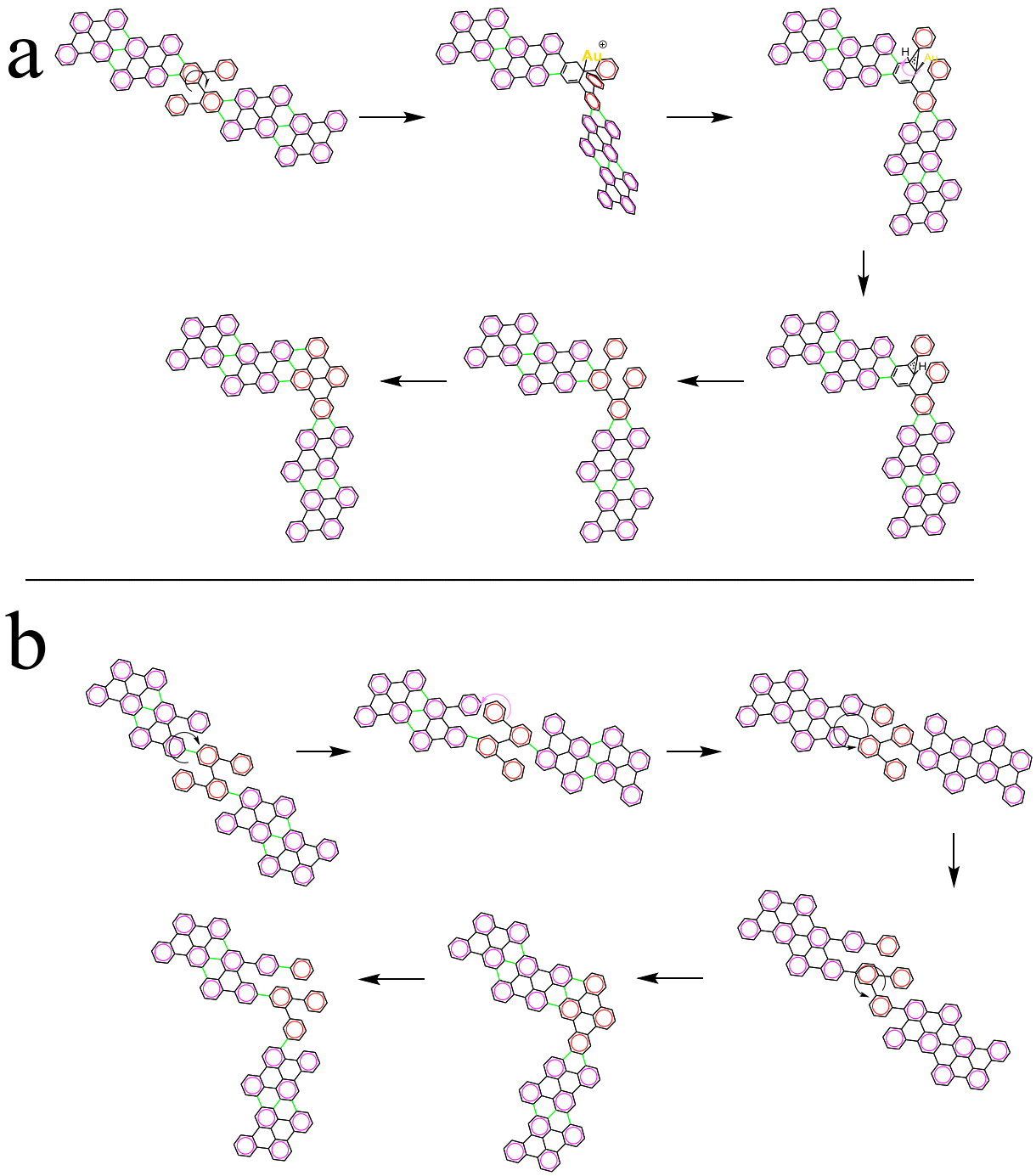

Figure A13. GNR defect motif B. Defect with phenyl rearrangement. Marked with red is the DBQP subunit that has undergone rearrangement. a) Single twist mechanism. b) Mechanism with 3 twists.

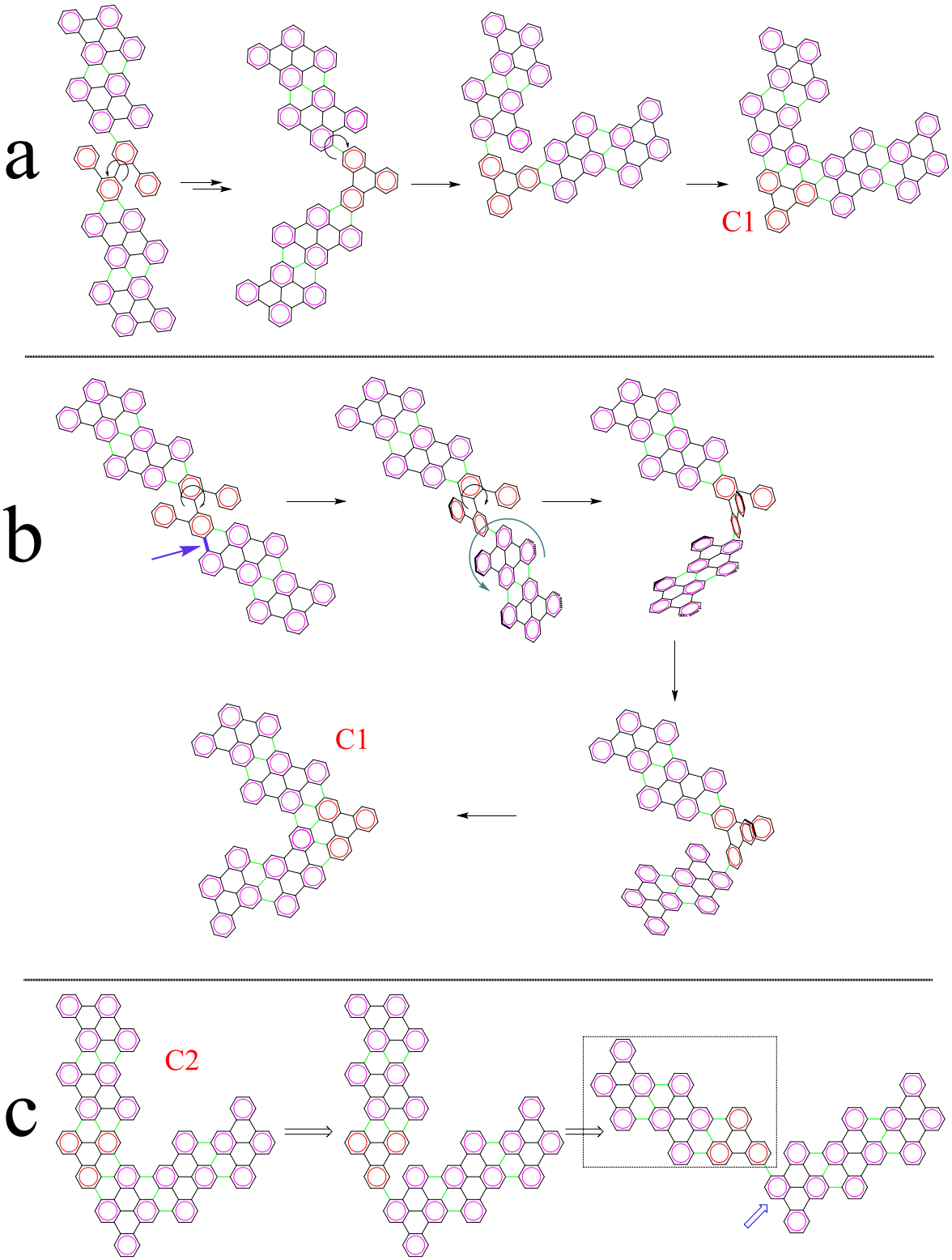

Figure A14. GNR defect motif C. a) This mechanism for motif C is considered to be the one that has taken place as can be rationalized from a single existing polymeric chain and requiring a single twist at the same defect. b) Similar to mechanism (*a*) it requires two twisting motions, c) Retrosynthetic pathway C2 cannot be rationalized from a single chain.

References

1. Den, W.; Chen, C.-H.; Luo, Y.-C., Revisiting the water-use efficiency performance for microelectronics manufacturing facilities: Using Taiwan's Science Parks as a case study. *Water-Energy Nexus* **2018,** *1* (2), 116-133.
2. Moore, G. E., Cramming more components onto integrated circuits, Reprinted from Electronics, volume 38, number 8, April 19, 1965, pp.114 ff. *IEEE Solid-State Circuits Society Newsletter* **2006,** *11* (3), 33-35.
3. Kumar, S., Fundamental Limits to Moore's Law. *arXiv e-prints* **2015**, arXiv:1511.05956.
4. Hsu, E.; Barmak, K.; West, A. C.; Park, A.-H. A., Advancements in the treatment and processing of electronic waste with sustainability: a review of metal extraction and recovery technologies. *Green Chemistry* **2019,** *21* (5), 919-936.
5. Grant, K.; Goldizen, F. C.; Sly, P. D.; Brune, M.-N.; Neira, M.; van den Berg, M.; Norman, R. E., Health consequences of exposure to e-waste: a systematic review. *The Lancet Global Health* **2013,** *1* (6), e350-e361.
6. Li, E. Y.; Marzari, N., Conductance Switching and Many-Valued Logic in Porphyrin Assemblies. *The Journal of Physical Chemistry Letters* **2013,** *4* (18), 3039-3044.
7. Lee, S. U.; Belosludov, R. V.; Mizuseki, H.; Kawazoe, Y., The Role of Aromaticity and the π-Conjugated Framework in Multiporphyrinic Systems as Single-Molecule Switches. *Small* **2008,** *4* (7), 962-969.
8. Tsai, M.-C.; Wang, C.-L.; Lin, C.-Y.; Tsai, C.-L.; Yen, H.-J.; You, H.-C.; Liou, G.-S., A novel porphyrin-containing polyimide for memory devices. *Polymer Chemistry* **2016,** *7* (16), 2780-2784.
9. Dakhlaoui, H.; Almansour, S.; Belhadj, W.; Wong, B. M., Modulating the conductance in graphene nanoribbons with multi-barriers under an applied voltage. *Results in Physics* **2021,** *27*, 104505.
10. Geng, Z.; Hähnlein, B.; Granzner, R.; Auge, M.; Lebedev, A. A.; Davydov, V. Y.; Kittler, M.; Pezoldt, J.; Schwierz, F., Graphene Nanoribbons for Electronic Devices. *Annalen der Physik* **2017,** *529* (11), 1700033.
11. Ghasemi, S.; Moth-Poulsen, K., Single molecule electronic devices with carbon-based materials: status and opportunity. *Nanoscale* **2021,** *13* (2), 659-671.
12. Tour, J. M., Top-Down versus Bottom-Up Fabrication of Graphene-Based Electronics. *Chemistry of Materials* **2014,** *26* (1), 163-171.
13. Eigler, D. M.; Schweizer, E. K., Positioning single atoms with a scanning tunnelling microscope. *Nature* **1990,** *344* (6266), 524-526.
14. Gross, L.; Mohn, F.; Moll, N.; Liljeroth, P.; Meyer, G., The Chemical Structure of a Molecule Resolved by Atomic Force Microscopy. *Science* **2009,** *325* (5944), 1110-1114.
15. Khalifeh, S., 1 - INTRODUCTION TO POLYMERS FOR ELECTRONIC ENGINEERS. In *Polymers in Organic Electronics*, Khalifeh, S., Ed. ChemTec Publishing: 2020; pp 1-31.
16. Sun, S. D., L., *Introduction to Organic Electronic and Optoelectronic materials and Devices*. 2nd edition ed.; CRC Press: 2016.
17. Shirota, Y.; Kageyama, H., 1 - Organic materials for optoelectronic applications: Overview. In *Handbook of Organic Materials for Electronic and Photonic Devices (Second Edition)*, Ostroverkhova, O., Ed. Woodhead Publishing: 2019; pp 3-42.
18. IUPAC. Compendium of Chemical Terminology, 2nd ed. (the "Gold Book"). Compiled by A. D. McNaught and A. Wilkinson. Blackwell Scientific Publications, Oxford (1997). Online version (2019-) created by S. J. Chalk. ISBN 0-9678550-9-8. https://doi.org/10.1351.
19. Khan, Q. U.; Begum, N.; Khan, K.; Rauf, M.; Zhan, Y., Novel Porphyrin–Perylene diimide for ultrafast high-performance resistive memory devices. *Organic Electronics* **2022,** *103*, 106453.

20. Michalak, R. J.; Ying-Hao, K.; Nash, F. D.; Szep, A.; Caffey, J. R.; Payson, P. M.; Haas, F.; McKeon, B. F.; Cook, P. R.; Brost, G. A.; Jingdong, L.; Jen, A. K. Y.; Dalton, L. R.; Steier, W. H., High-speed AJL8/APC polymer modulator. *IEEE Photonics Technology Letters* **2006,** *18* (11), 1207-1209.
21. Xin, N.; Guan, J.; Zhou, C.; Chen, X.; Gu, C.; Li, Y.; Ratner, M. A.; Nitzan, A.; Stoddart, J. F.; Guo, X., Concepts in the design and engineering of single-molecule electronic devices. *Nature Reviews Physics* **2019,** *1* (3), 211-230.
22. Sun, L.; Diaz-Fernandez, Y. A.; Gschneidtner, T. A.; Westerlund, F.; Lara-Avila, S.; Moth-Poulsen, K., Single-molecule electronics: from chemical design to functional devices. *Chemical Society Reviews* **2014,** *43* (21), 7378-7411.
23. Zwick, P.; Dulić, D.; van der Zant, H. S. J.; Mayor, M., Porphyrins as building blocks for single-molecule devices. *Nanoscale* **2021,** *13* (37), 15500-15525.
24. Braun, J.; Koecher, M.; Schlabach, M.; Wehrle, B.; Limbach, H.-H.; Vogel, E., NMR Study of the Tautomerism of Porphyrin Including the Kinetic HH/HD/DD Isotope Effects in the Liquid and the Solid State. *Journal of the American Chemical Society* **1994,** *116* (15), 6593-6604.
25. Braun, J.; Schwesinger, R.; Williams, P. G.; Morimoto, H.; Wemmer, D. E.; Limbach, H.-H., Kinetic H/D/T Isotope and Solid State Effects on the Tautomerism of the Conjugate Porphyrin Monoanion. *Journal of the American Chemical Society* **1996,** *118* (45), 11101-11110.
26. Liljeroth, P.; Repp, J.; Meyer, G., Current-Induced Hydrogen Tautomerization and Conductance Switching of Naphthalocyanine Molecules. *Science* **2007,** *317* (5842), 1203-1206.
27. Sperl, A.; Kröger, J.; Berndt, R., Controlled Metalation of a Single Adsorbed Phthalocyanine. *Angewandte Chemie International Edition* **2011,** *50* (23), 5294-5297.
28. Auwärter, W.; Seufert, K.; Bischoff, F.; Ecija, D.; Vijayaraghavan, S.; Joshi, S.; Klappenberger, F.; Samudrala, N.; Barth, J. V., A surface-anchored molecular four-level conductance switch based on single proton transfer. *Nature Nanotechnology* **2012,** *7* (1), 41-46.
29. Mugarza, A.; Lorente, N.; Ordejón, P.; Krull, C.; Stepanow, S.; Bocquet, M. L.; Fraxedas, J.; Ceballos, G.; Gambardella, P., Orbital Specific Chirality and Homochiral Self-Assembly of Achiral Molecules Induced by Charge Transfer and Spontaneous Symmetry Breaking. *Physical Review Letters* **2010,** *105* (11), 115702.
30. Kügel, J.; Sixta, A.; Böhme, M.; Krönlein, A.; Bode, M., Breaking Degeneracy of Tautomerization—Metastability from Days to Seconds. *ACS Nano* **2016,** *10* (12), 11058-11065.
31. Kügel, J.; Leisegang, M.; Bode, M., Imprinting Directionality into Proton Transfer Reactions of an Achiral Molecule. *ACS Nano* **2018,** *12* (8), 8733-8738.
32. Bischoff, F.; Seufert, K.; Auwärter, W.; Joshi, S.; Vijayaraghavan, S.; Écija, D.; Diller, K.; Papageorgiou, A. C.; Fischer, S.; Allegretti, F.; Duncan, D. A.; Klappenberger, F.; Blobner, F.; Han, R.; Barth, J. V., How Surface Bonding and Repulsive Interactions Cause Phase Transformations: Ordering of a Prototype Macrocyclic Compound on Ag(111). *ACS Nano* **2013,** *7* (4), 3139-3149.
33. Wiengarten, A.; Seufert, K.; Auwärter, W.; Ecija, D.; Diller, K.; Allegretti, F.; Bischoff, F.; Fischer, S.; Duncan, D. A.; Papageorgiou, A. C.; Klappenberger, F.; Acres, R. G.; Ngo, T. H.; Barth, J. V., Surface-assisted dehydrogenative homocoupling of porphine molecules. *Journal of the American Chemical Society* **2014,** *136*, 9346-9354.
34. Noori, M.; Aragonès, A. C.; Di Palma, G.; Darwish, N.; Bailey, S. W. D.; Al-Galiby, Q.; Grace, I.; Amabilino, D. B.; González-Campo, A.; Díez-Pérez, I.; Lambert, C. J., Tuning the electrical conductance of metalloporphyrin supramolecular wires. *Scientific Reports* **2016,** *6* (1), 37352.
35. Aragonès, A. C.; Darwish, N.; Saletra, W. J.; Pérez-García, L.; Sanz, F.; Puigmartí-Luis, J.; Amabilino, D. B.; Díez-Pérez, I., Highly Conductive Single-Molecule Wires with Controlled Orientation by Coordination of Metalloporphyrins. *Nano Letters* **2014,** *14* (8), 4751-4756.
36. Liu, Z.-F.; Wei, S.; Yoon, H.; Adak, O.; Ponce, I.; Jiang, Y.; Jang, W.-D.; Campos, L. M.; Venkataraman, L.; Neaton, J. B., Control of Single-Molecule Junction Conductance of Porphyrins via a Transition-Metal Center. *Nano Letters* **2014,** *14* (9), 5365-5370.

37. El Abbassi, M.; Zwick, P.; Rates, A.; Stefani, D.; Prescimone, A.; Mayor, M.; van der Zant, H. S. J.; Dulić, D., Unravelling the conductance path through single-porphyrin junctions. *Chemical Science* **2019,** *10* (36), 8299-8305.
38. Aragonès, A. C.; Martín-Rodríguez, A.; Aravena, D.; Puigmartí-Luis, J.; Amabilino, D. B.; Aliaga-Alcalde, N.; González-Campo, A.; Ruiz, E.; Díez-Pérez, I., Tuning Single-Molecule Conductance in Metalloporphyrin-Based Wires via Supramolecular Interactions. *Angewandte Chemie International Edition* **2020,** *59* (43), 19193-19201.
39. Castro-Cruz, H. M.; Arias-Aranda, L. R.; Farfán, N.; Xochitiotzi-Flores, E.; Macías-Ruvalcaba, N. A., Elucidating the Electroreduction Mechanism of the Monoprotonated Octaethylporphyrin. A Comparative Study with the Diprotonated Octaethyl- and meso-Tetraphenyl-porphyrins. *Journal of The Electrochemical Society* **2020,** *167* (15), 155507.
40. Inisan, C.; Saillard, J.-Y.; Guilard, R.; Tabard, A.; Le Mest, Y., Electrooxidation of porphyrin free bases: fate of the π-cation radical. *New Journal of Chemistry* **1998,** *22* (8), 823-830.
41. Maher, A. G.; Liu, M.; Nocera, D. G., Ligand Noninnocence in Nickel Porphyrins: Nickel Isobacteriochlorin Formation under Hydrogen Evolution Conditions. *Inorganic Chemistry* **2019,** *58* (12), 7958-7968.
42. Li, J.; Merino-Díez, N.; Carbonell-Sanromà, E.; Vilas-Varela, M.; de Oteyza, D. G.; Peña, D.; Corso, M.; Pascual, J. I., Survival of spin state in magnetic porphyrins contacted by graphene nanoribbons. *Science Advances* **2018,** *4* (2), eaaq0582.
43. Perkins, W.; Fischer, F. R., Inserting Porphyrin Quantum Dots in Bottom-Up Synthesized Graphene Nanoribbons. *Chemistry – A European Journal* **2017,** *23* (70), 17687-17691.
44. Mol, J. A.; Lau, C. S.; Lewis, W. J. M.; Sadeghi, H.; Roche, C.; Cnossen, A.; Warner, J. H.; Lambert, C. J.; Anderson, H. L.; Briggs, G. A. D., Graphene-porphyrin single-molecule transistors. *Nanoscale* **2015,** *7* (31), 13181-13185.
45. Lörtscher, E., Wiring molecules into circuits. *Nature Nanotechnology* **2013,** *8* (6), 381-384.
46. Houtsma, R. S. K.; de la Rie, J.; Stöhr, M., Atomically precise graphene nanoribbons: interplay of structural and electronic properties. *Chemical Society Reviews* **2021,** *50* (11), 6541-6568.
47. Yano, Y.; Mitoma, N.; Ito, H.; Itami, K., A Quest for Structurally Uniform Graphene Nanoribbons: Synthesis, Properties, and Applications. *The Journal of Organic Chemistry* **2020,** *85* (1), 4-33.
48. Wang, D.; Lu, X.; Arramel; Yang, M.; Wu, J.; Wee, A. T. S., On-Surface Synthesis of Variable Bandgap Nanoporous Graphene. *Small* **2021,** *17* (42), 2102246.
49. Tenorio, M.; Moreno, C.; Febrer, P.; Castro-Esteban, J.; Ordejón, P.; Peña, D.; Pruneda, M.; Mugarza, A., Atomically Sharp Lateral Superlattice Heterojunctions Built-in Nitrogen-doped Nanoporous Graphene. *Advanced Materials* **2022,** *n/a* (n/a), 2110099.
50. Kojima, T.; Nakae, T.; Xu, Z.; Saravanan, C.; Watanabe, K.; Nakamura, Y.; Sakaguchi, H., Bottom-Up On-Surface Synthesis of Two-Dimensional Graphene Nanoribbon Networks and Their Thermoelectric Properties. *Chemistry – An Asian Journal* **2019,** *14* (23), 4400-4407.
51. Cheng, S.; Su, X.; Gan, F.; Shen, C.; Qiu, H.; Tao, K.; Yu, P., Stepwise On-Surface Synthesis of Porous Carbon Nanoribbons with Notched Zigzag Edges. *The Journal of Physical Chemistry C* **2020,** *124* (1), 756-763.
52. Jacobse, P. H.; McCurdy, R. D.; Jiang, J.; Rizzo, D. J.; Veber, G.; Butler, P.; Zuzak, R.; Louie, S. G.; Fischer, F. R.; Crommie, M. F., Bottom-up Assembly of Nanoporous Graphene with Emergent Electronic States. *Journal of the American Chemical Society* **2020,** *142* (31), 13507-13514.
53. Moreno, C.; Vilas-Varela, M.; Kretz, B.; Garcia-Lekue, A.; Costache Marius, V.; Paradinas, M.; Panighel, M.; Ceballos, G.; Valenzuela Sergio, O.; Peña, D.; Mugarza, A., Bottom-up synthesis of multifunctional nanoporous graphene. *Science* **2018,** *360* (6385), 199-203.
54. Mutlu, Z.; Jacobse, P. H.; McCurdy, R. D.; Llinas, J. P.; Lin, Y.; Veber, G. C.; Fischer, F. R.; Crommie, M. F.; Bokor, J., Bottom-Up Synthesized Nanoporous Graphene Transistors. *Advanced Functional Materials* **2021,** *31* (47), 2103798.

55. Cai, J.; Ruffieux, P.; Jaafar, R.; Bieri, M.; Braun, T.; Blankenburg, S.; Muoth, M.; Seitsonen, A. P.; Saleh, M.; Feng, X.; Müllen, K.; Fasel, R., Atomically precise bottom-up fabrication of graphene nanoribbons. *Nature* **2010,** *466* (7305), 470-473.
56. Galeotti, G.; Di Giovannantonio, M.; Lipton-Duffin, J.; Ebrahimi, M.; Tebi, S.; Verdini, A.; Floreano, L.; Fagot-Revurat, Y.; Perepichka, D. F.; Rosei, F.; Contini, G., The role of halogens in on-surface Ullmann polymerization. *Faraday Discussions* **2017,** *204* (0), 453-469.
57. Bronner, C.; Marangoni, T.; Rizzo, D. J.; Durr, R. A.; Jørgensen, J. H.; Fischer, F. R.; Crommie, M. F., Iodine versus Bromine Functionalization for Bottom-Up Graphene Nanoribbon Growth: Role of Diffusion. *The Journal of Physical Chemistry C* **2017,** *121* (34), 18490-18495.
58. Jacobse, P. H.; van den Hoogenband, A.; Moret, M.-E.; Klein Gebbink, R. J. M.; Swart, I., Aryl Radical Geometry Determines Nanographene Formation on Au(111). *Angewandte Chemie International Edition* **2016,** *55* (42), 13052-13055.
59. Simonov, K. A.; Generalov, A. V.; Vinogradov, A. S.; Svirskiy, G. I.; Cafolla, A. A.; McGuinness, C.; Taketsugu, T.; Lyalin, A.; Mårtensson, N.; Preobrajenski, A. B., Synthesis of armchair graphene nanoribbons from the 10,10'-dibromo-9,9'-bianthracene molecules on Ag(111): the role of organometallic intermediates. *Scientific Reports* **2018,** *8* (1), 3506.
60. Thussing, S.; Flade, S.; Eimre, K.; Pignedoli, C. A.; Fasel, R.; Jakob, P., Reaction Pathway toward Seven-Atom-Wide Armchair Graphene Nanoribbon Formation and Identification of Intermediate Species on Au(111). *The Journal of Physical Chemistry C* **2020,** *124* (29), 16009-16018.
61. Zint, S.; Ebeling, D.; Schlöder, T.; Ahles, S.; Mollenhauer, D.; Wegner, H. A.; Schirmeisen, A., Imaging Successive Intermediate States of the On-Surface Ullmann Reaction on Cu(111): Role of the Metal Coordination. *ACS Nano* **2017,** *11* (4), 4183-4190.
62. Senkovskiy, B. V.; Nenashev, A. V.; Alavi, S. K.; Falke, Y.; Hell, M.; Bampoulis, P.; Rybkovskiy, D. V.; Usachov, D. Y.; Fedorov, A. V.; Chernov, A. I.; Gebhard, F.; Meerholz, K.; Hertel, D.; Arita, M.; Okuda, T.; Miyamoto, K.; Shimada, K.; Fischer, F. R.; Michely, T.; Baranovskii, S. D.; Lindfors, K.; Szkopek, T.; Grüneis, A., Tunneling current modulation in atomically precise graphene nanoribbon heterojunctions. *Nature Communications* **2021,** *12* (1), 2542.
63. Seufert, K.; McBride, F.; Jaekel, S.; Wit, B.; Haq, S.; Steiner, A.; Poli, P.; Persson, M.; Raval, R.; Grill, L., Porphine Homocoupling on Au(111). In *The Journal of Physical Chemistry C*, American Chemical Society: 2019; Vol. 123, pp 16690-16698.
64. Floris, A.; Haq, S.; In't Veld, M.; Amabilino, D. B.; Raval, R.; Kantorovich, L., Driving Forces for Covalent Assembly of Porphyrins by Selective C–H Bond Activation and Intermolecular Coupling on a Copper Surface. *Journal of the American Chemical Society* **2016,** *138* (18), 5837-5847.
65. Dyer, M. S.; Robin, A.; Haq, S.; Raval, R.; Persson, M.; Klimeš, J., Understanding the Interaction of the Porphyrin Macrocycle to Reactive Metal Substrates: Structure, Bonding, and Adatom Capture. *ACS Nano* **2011,** *5* (3), 1831-1838.
66. Hanke, F.; Haq, S.; Raval, R.; Persson, M., Heat-to-connect: Surface commensurability directs organometallic one-dimensional self-assembly. In *ACS Nano*, 2011; Vol. 5, pp 9093-9103.
67. Hanke, F.; Haq, S.; Raval, R.; Persson, M., Heat-to-Connect: Surface Commensurability Directs Organometallic One-Dimensional Self-Assembly. *ACS Nano* **2011,** *5* (11), 9093-9103.
68. Haq, S.; Hanke, F.; Dyer, M. S.; Persson, M.; Iavicoli, P.; Amabilino, D. B.; Raval, R., Clean coupling of unfunctionalized porphyrins at surfaces to give highly oriented organometallic oligomers. In *Journal of the American Chemical Society*, 2011; Vol. 133, pp 12031-12039.
69. Xiang, F.; Gemeinhardt, A.; Schneider, M. A., Competition between Dehydrogenative Organometallic Bonding and Covalent Coupling of an Unfunctionalized Porphyrin on Cu(111). *ACS Nano* **2018,** *12* (2), 1203-1210.
70. Seufert, K.; McBride, F.; Jaekel, S.; Wit, B.; Haq, S.; Steiner, A.; Poli, P.; Persson, M.; Raval, R.; Grill, L., Porphine Homocoupling on Au(111). *The Journal of Physical Chemistry C* **2019,** *123* (27), 16690-16698.

71. Sun, Q.; Mateo, L. M.; Robles, R.; Lorente, N.; Ruffieux, P.; Bottari, G.; Torres, T.; Fasel, R., Bottom-up Fabrication and Atomic-Scale Characterization of Triply Linked, Laterally π-Extended Porphyrin Nanotapes**. In *Angewandte Chemie - International Edition*, 2021; Vol. 60, pp 16208-16214.
72. Jassas, R. S.; Mughal, E. U.; Sadiq, A.; Alsantali, R. I.; Al-Rooqi, M. M.; Naeem, N.; Moussa, Z.; Ahmed, S. A., Scholl reaction as a powerful tool for the synthesis of nanographenes: a systematic review. *RSC Advances* **2021,** *11* (51), 32158-32202.
73. Binnig, G.; Rohrer, H., Scanning tunneling microscopy. *Surface Science* **1983,** *126* (1), 236-244.
74. Binnig, G.; Rohrer, H.; Gerber, C.; Weibel, E., Surface Studies by Scanning Tunneling Microscopy. *Physical Review Letters* **1982,** *49* (1), 57-61.
75. Binnig, G.; Quate, C. F.; Gerber, C., Atomic Force Microscope. *Physical Review Letters* **1986,** *56* (9), 930-933.
76. Giessibl Franz, J., Atomic Resolution of the Silicon (111)-(7×7) Surface by Atomic Force Microscopy. *Science* **1995,** *267* (5194), 68-71.
77. Peng, J.; Guo, J.; Ma, R.; Jiang, Y., Water-solid interfaces probed by high-resolution atomic force microscopy. *Surface Science Reports* **2022,** *77* (1), 100549.
78. Giessibl, F. J., Advances in atomic force microscopy. *Reviews of Modern Physics* **2003,** *75* (3), 949-983.
79. Giessibl, F. J., AFM's path to atomic resolution. *Materials Today* **2005,** *8* (5), 32-41.
80. Giessibl, F. J., Principle of NC-AFM. In *Noncontact Atomic Force Microscopy*, Morita, S.; Wiesendanger, R.; Meyer, E., Eds. Springer Berlin Heidelberg: Berlin, Heidelberg, 2002; pp 11-46.
81. Giessibl, F. J., Principles and Applications of the qPlus Sensor. In *Noncontact Atomic Force Microscopy: Volume 2*, Morita, S.; Giessibl, F. J.; Wiesendanger, R., Eds. Springer Berlin Heidelberg: Berlin, Heidelberg, 2009; pp 121-142.
82. Morita, S.; Giessibl, F. J.; Sugawara, Y.; Hosoi, H.; Mukasa, K.; Sasahara, A.; Onishi, H., Noncontact Atomic Force Microscopy and Its Related Topics. In *Springer Handbook of Nanotechnology*, Bhushan, B., Ed. Springer Berlin Heidelberg: Berlin, Heidelberg, 2004; pp 385-411.
83. Voigtländer, B., Technical Aspects of Atomic Force Microscopy. In *Atomic Force Microscopy*, Voigtländer, B., Ed. Springer International Publishing: Cham, 2019; pp 35-67.
84. Chen, C. J., *Introduction to scanning tunneling microscopy [electronic resource] / C. Julian Chen*. Oxford University Press: New York, 1993.
85. Meyer, E.; Hug, H. J.; Bennewitz, R., Introduction to Scanning Probe Microscopy. In *Scanning Probe Microscopy: The Lab on a Tip*, Meyer, E.; Hug, H. J.; Bennewitz, R., Eds. Springer Berlin Heidelberg: Berlin, Heidelberg, 2004; pp 1-13.
86. Meyer, E.; Hug, H. J.; Bennewitz, R., Introduction to Scanning Tunneling Microscopy. In *Scanning Probe Microscopy: The Lab on a Tip*, Meyer, E.; Hug, H. J.; Bennewitz, R., Eds. Springer Berlin Heidelberg: Berlin, Heidelberg, 2004; pp 15-44.
87. Meyer, E.; Hug, H. J.; Bennewitz, R., Force Microscopy. In *Scanning Probe Microscopy: The Lab on a Tip*, Meyer, E.; Hug, H. J.; Bennewitz, R., Eds. Springer Berlin Heidelberg: Berlin, Heidelberg, 2004; pp 45-95.
88. Tersoff, J.; Hamann, D. R., Theory and Application for the Scanning Tunneling Microscope. *Physical Review Letters* **1983,** *50* (25), 1998-2001.
89. Tersoff, J.; Hamann, D. R., Theory of the scanning tunneling microscope. *Physical Review B* **1985,** *31* (2), 805-813.
90. Bardeen, J., Tunnelling from a Many-Particle Point of View. *Physical Review Letters* **1961,** *6* (2), 57-59.
91. Selloni, A.; Carnevali, P.; Tosatti, E.; Chen, C. D., Voltage-dependent scanning-tunneling microscopy of a crystal surface: Graphite. *Physical Review B* **1985,** *31* (4), 2602-2605.
92. Feenstra, R. M., Scanning tunneling spectroscopy. *Surface Science* **1994,** *299-300*, 965-979.

93. Stroscio, J. A.; Feenstra, R. M.; Fein, A. P., Electronic Structure of the Si(111)2*1 Surface by Scanning-Tunneling Microscopy. *Physical Review Letters* **1986,** *57* (20), 2579-2582.
94. Stroscio, J. A.; Feenstra, R. M.; Fein, A. P., Imaging electronic surface states in real space on the Si(111) 2×1 surface. *Journal of Vacuum Science & Technology A* **1987,** *5* (4), 838-841.
95. Ducke, J.; Riss, A.; Pérez Paz, A.; Seufert, K.; Schwarz, M.; Garnica, M.; Rubio, A.; Auwärter, W., Layered Insulator/Molecule/Metal Heterostructures with Molecular Functionality through Porphyrin Intercalation. *ACS Nano* **2018,** *12* (3), 2677-2684.
96. Mohn, F.; Gross, L.; Moll, N.; Meyer, G., Imaging the charge distribution within a single molecule. In *Nature Nanotechnology*, Nature Publishing Group: 2012; Vol. 7, pp 227-231.
97. Fatayer, S.; Albrecht, F.; Zhang, Y.; Urbonas, D.; Peña, D.; Moll, N.; Gross, L., Molecular structure elucidation with charge-state control. In *Science*, 2019; Vol. 365, pp 142-145.
98. Pérez, R.; Štich, I.; Payne, M. C.; Terakura, K., Surface-tip interactions in noncontact atomic-force microscopy on reactive surfaces: Si(111). *Physical Review B* **1998,** *58* (16), 10835-10849.
99. Dürig, U.; Züger, O.; Pohl, D. W., Observation of metallic adhesion using the scanning tunneling microscope. *Physical Review Letters* **1990,** *65* (3), 349-352.
100. Loppacher, C.; Bammerlin, M.; Guggisberg, M.; Schär, S.; Bennewitz, R.; Baratoff, A.; Meyer, E.; Güntherodt, H. J., Dynamic force microscopy of copper surfaces: Atomic resolution and distance dependence of tip-sample interaction and tunneling current. *Physical Review B* **2000,** *62* (24), 16944-16949.
101. Zhang, X.-J., Van der Waals Forces. In *Encyclopedia of Tribology*, Wang, Q. J.; Chung, Y.-W., Eds. Springer US: Boston, MA, 2013; pp 3945-3947.
102. Hamaker, H. C., The London—van der Waals attraction between spherical particles. *Physica* **1937,** *4* (10), 1058-1072.
103. Saint Jean, M.; Hudlet, S.; Guthmann, C.; Berger, J., Van der Waals and capacitive forces in atomic force microscopies. *Journal of Applied Physics* **1999,** *86* (9), 5245-5248.
104. Kantorovich, L. N.; Foster, A. S.; Shluger, A. L.; Stoneham, A. M., Role of image forces in non-contact scanning force microscope images of ionic surfaces. *Surface Science* **2000,** *445* (2), 283-299.
105. Burnham, N. A.; Colton, R. J.; Pollock, H. M., Work-function anisotropies as an origin of long-range surface forces. *Physical Review Letters* **1992,** *69* (1), 144-147.
106. de la Torre, B.; Švec, M.; Foti, G.; Krejčí, O.; Hapala, P.; Garcia-Lekue, A.; Frederiksen, T.; Zbořil, R.; Arnau, A.; Vázquez, H.; Jelínek, P., Submolecular Resolution by Variation of the Inelastic Electron Tunneling Spectroscopy Amplitude and its Relation to the AFM/STM Signal. *Physical Review Letters* **2017,** *119* (16), 166001.
107. Hapala, P.; Švec, M.; Stetsovych, O.; van der Heijden, N. J.; Ondráček, M.; van der Lit, J.; Mutombo, P.; Swart, I.; Jelínek, P., Mapping the electrostatic force field of single molecules from high-resolution scanning probe images. *Nature Communications* **2016,** *7* (1), 11560.
108. Gross, L.; Schuler, B.; Pavliček, N.; Fatayer, S.; Majzik, Z.; Moll, N.; Peña, D.; Meyer, G., Atomic Force Microscopy for Molecular Structure Elucidation. *Angewandte Chemie International Edition* **2018,** *57* (15), 3888-3908.
109. Fatayer, S.; Albrecht, F.; Zhang, Y.; Urbonas, D.; Peña, D.; Moll, N.; Gross, L., Molecular structure elucidation with charge-state control. *Science* **2019,** *365* (6449), 142-145.
110. Jelínek, P., High resolution SPM imaging of organic molecules with functionalized tips. *Journal of Physics: Condensed Matter* **2017,** *29* (34), 343002.
111. Giessibl, F. J.; Hembacher, S.; Herz, M.; Schiller, C.; Mannhart, J., Stability considerations and implementation of cantilevers allowing dynamic force microscopy with optimal resolution: the qPlus sensor. *Nanotechnology* **2004,** *15* (2), S79-S86.
112. Giessibl, F. J., A direct method to calculate tip–sample forces from frequency shifts in frequency-modulation atomic force microscopy. *Applied Physics Letters* **2000,** *78* (1), 123-125.

113. Welker, J. I., E.; Giessibl, F. J., Analysis of force-deconvolution methods in frequency-modulation atomic force microscopy. *Beilstein J. Nanotechnol.* **2012,** *3*.
114. Sader, J. E.; Jarvis, S. P., Accurate formulas for interaction force and energy in frequency modulation force spectroscopy. *Applied Physics Letters* **2004,** *84* (10), 1801-1803.
115. Hapala, P.; Ondráček, M.; Stetsovych, O.; Švec, M.; Jelínek, P., Simultaneous nc-AFM/STM Measurements with Atomic Resolution. In *Noncontact Atomic Force Microscopy: Volume 3*, Morita, S.; Giessibl, F. J.; Meyer, E.; Wiesendanger, R., Eds. Springer International Publishing: Cham, 2015; pp 29-49.
116. Giessibl, F. J., The qPlus sensor, a powerful core for the atomic force microscope. *Review of Scientific Instruments* **2019,** *90* (1), 011101.
117. Giessibl, F. J., High-speed force sensor for force microscopy and profilometry utilizing a quartz tuning fork. *Applied Physics Letters* **1998,** *73* (26), 3956-3958.
118. Giessibl, F. J., Atomic Force Microscopy on Its Way to Adolescence. *AIP Conference Proceedings* **2003,** *696* (1), 60-67.
119. Bischoff, F. Scanning probe microscopy studies of surface confined molecules and (metal-organic) nanostructures. Ph.D. Thesis, Technische Universität München, München, 2018.
120. VAb Vakuum-Anlagenbau GmbH, Marie-Curie-Straße 11, 25337 Elmshorn, Germany.
121. Createc Fischer & Co. GmbH, Industriestr. 9, 74391 Erligheim, Germany.
122. Newport Corporation, 1791 Deere Avenue, Irvine, California 92606, USA.
123. Pfeiffer Vacuum GmbH, Berliner Strasse 43, 35614 Asslar, Germany.
124. Leybold GmbH, Bonner Str. 498, 50968 Köln, Germany. .
125. SPECS GmbH, Voltastrasse 5, 13355 Berlin, Germany.
126. Stanford Research Systems, Inc., 1290-D Reamwood Avenue, Sunnyvale, CA 94089, USA.
127. Yamamura, Y.; Tawara, H., ENERGY DEPENDENCE OF ION-INDUCED SPUTTERING YIELDS FROM MONATOMIC SOLIDS AT NORMAL INCIDENCE. *Atomic Data and Nuclear Data Tables* **1996,** *62* (2), 149-253.
128. Schmid, M. Simple Sputter Yield Calculator. https://www.iap.tuwien.ac.at/www/surface/sputteryield.
129. GmbH., S., Useful Information and Facts about the Practice of Sputtering. **2018**.
130. SPECS, *Ion Source IQE 10 and IQE 11 Manual 1.3*. 2007.
131. Liebig, A.; Hapala, P.; Weymouth, A. J.; Giessibl, F. J., Quantifying the evolution of atomic interaction of a complex surface with a functionalized atomic force microscopy tip. *Scientific Reports* **2020,** *10* (1), 14104.
132. Hapala, P.; Temirov, R.; Tautz, F. S.; Jelínek, P., Origin of High-Resolution IETS-STM Images of Organic Molecules with Functionalized Tips. *Physical Review Letters* **2014,** *113* (22), 226101.
133. Hapala, P.; Kichin, G.; Wagner, C.; Tautz, F. S.; Temirov, R.; Jelínek, P., Mechanism of high-resolution STM/AFM imaging with functionalized tips. *Physical Review B* **2014,** *90* (8), 085421.
134. Minkin, V. I., Glossary of terms used in theoretical organic chemistry. *Pure and Applied Chemistry* **1999,** *71* (10), 1919-1981.
135. Watts, L. F., J. D.; Pettit, R., Cyclobutadiene. In *J .Am. Chem. Soc.*, 1965; Vol. 87, pp 3253-3254.
136. Dietrich; H., D., H., Crystal Structure of Tri(cyclooctatetraene)dititanium. In *Angew. Chem. Intern. Ed. Engl.*, 1966; Vol. 5, p 899.
137. Claus, K. H.; Krüger, C., Structure of cyclooctatetraene at 129 K. In *Acta Crystallographica Section C*, International Union of Crystallography (IUCr): 1988; Vol. 44, pp 1632-1634.
138. Nakamura, Y.; Aratani, N.; Shinokubo, H.; Takagi, A.; Kawai, T.; Matsumoto, T.; Yoon, Z. S.; Kim, D. Y.; Ahn, T. K.; Kim, D.; Muranaka, A.; Kobayashi, N.; Osuka, A., A directly fused tetrameric porphyrin sheet and its anomalous electronic properties that arise from the planar cyclooctatetraene core. In *Journal of the American Chemical Society*, 2006; Vol. 128, pp 4119-4127.

139. Ni, Y.; Sandoval-Salinas, M. E.; Tanaka, T.; Phan, H.; Herng, T. S.; Gopalakrishna, T. Y.; Ding, J.; Osuka, A.; Casanova, D.; Wu, J., [n]Cyclo-para-biphenylmethine Polyradicaloids: [n]Annulene Analogs and Unusual Valence Tautomerization. In *Chem*, 2019; Vol. 5, pp 108-121.
140. Chen, F.; Hong, Y. S.; Kim, D.; Tanaka, T.; Osuka, A., Sequential N-Alkylations of Tetrabenzotetraaza[8]circulene as a Tool To Tune Its Optical Properties. In *ChemPlusChem*, 2017; Vol. 82, pp 1048-1051.
141. Hiroto, S.; Furukawa, K.; Shinokubo, H.; Osuka, A., Synthesis and biradicaloid character of doubly linked corrole dimers. In *Journal of the American Chemical Society*, 2006; Vol. 128, pp 12380-12381.
142. Nakamura, Y.; Aratani, N.; Furukawa, K.; Osuka, A., Synthesis and characterizations of free base and Cu(II) complex of a porphyrin sheet. In *Tetrahedron*, Elsevier Ltd: 2008; Vol. 64, pp 11433-11439.
143. Chen, F.; Hong, Y. S.; Shimizu, S.; Kim, D.; Tanaka, T.; Osuka, A., Synthesis of a Tetrabenzotetraaza[8]circulene by a "Fold-In" Oxidative Fusion Reaction. In *Angewandte Chemie*, 2015; Vol. 127, pp 10785-10788.
144. Nagata, Y.; Kato, S.; Miyake, Y.; Shinokubo, H., Synthesis of Tetraaza[8]circulenes from Tetrathia[8]circulenes through an SNAr-Based Process. In *Organic Letters*, 2017; Vol. 19, pp 2718-2721.
145. Nobusue, S.; Miyoshi, H.; Shimizu, A.; Hisaki, I.; Fukuda, K.; Nakano, M.; Tobe, Y., Tetracyclopenta[def,jkl,pqr,vwx]tetraphenylene: A potential tetraradicaloid hydrocarbon. In *Angewandte Chemie - International Edition*, 2015; Vol. 54, pp 2090-2094.
146. Olah, G. A.; Liang, G.; Staral, J. S.; Paquette, L. A.; Melega, W. P.; Carmody, M. J., Novel Aromatic Systems. 8.1 Cyclooctatetraene Dications. In *Journal of the American Chemical Society*, 1977; Vol. 99, pp 3349-3355.
147. Seyferth, D., Uranocene. The first member of a new class of organometallic derivatives of the f elements. In *Organometallics*, 2004; Vol. 23, pp 3562-3583.
148. Sroor, F. M., Recent progress of organometallic cyclooctatetraenide dianion chemistry. In *Journal of Organometallic Chemistry*, Elsevier B.V.: 2021; Vol. 948, p 121878.
149. Braun, J.; Limbach, H.-H.; Williams, P. G.; Morimoto, H.; Wemmer, D. E., Observation of Kinetic Tritium Isotope Effects by Dynamic NMR. The Tautomerism of Porphyrin. *Journal of the American Chemical Society* **1996,** *118* (30), 7231-7232.
150. Limbach, H.-H.; Miguel Lopez, J.; Kohen, A., Arrhenius curves of hydrogen transfers: tunnel effects, isotope effects and effects of pre-equilibria. *Philosophical Transactions of the Royal Society B: Biological Sciences* **2006,** *361* (1472), 1399-1415.
151. Swart, M., Bond orders in metalloporphyrins. *Theoretical Chemistry Accounts* **2020,** *139* (10), 160.
152. Cyrañski, M. K.; Krygowski, T. M.; Wisiorowski, M.; van Eikema Hommes, N. J. R.; Schleyer, P. v. R., Global and Local Aromaticity in Porphyrins: An Analysis Based on Molecular Geometries and Nucleus-Independent Chemical Shifts. *Angewandte Chemie International Edition* **1998,** *37* (1-2), 177-180.
153. Feixas, F.; Solà, M.; Swart, M., Chemical bonding and aromaticity in metalloporphyrins. *Canadian Journal of Chemistry* **2009,** *87* (7), 1063-1073.
154. Aihara, J.-i., Macrocyclic Conjugation Pathways in Porphyrins. *The Journal of Physical Chemistry A* **2008,** *112* (23), 5305-5311.
155. Aihara, J.-i.; Kimura, E.; Krygowski, T. M., Aromatic Conjugation Pathways in Porphyrins. *Bulletin of the Chemical Society of Japan* **2008,** *81* (7), 826-835.
156. Faglioni, F.; Ligabue, A.; Pelloni, S.; Soncini, A.; Viglione, R. G.; Ferraro, M. B.; Zanasi, R.; Lazzeretti, P., Why Downfield Proton Chemical Shifts Are Not Reliable Aromaticity Indicators. *Organic Letters* **2005,** *7* (16), 3457-3460.
157. Wannere, C. S.; Corminboeuf, C.; Allen, W. D.; Schaefer, H. F.; Schleyer, P. v. R., Downfield Proton Chemical Shifts Are Not Reliable Aromaticity Indicators. *Organic Letters* **2005,** *7* (8), 1457-1460.
158. Wu, J. I.; Fernández, I.; Schleyer, P. v. R., Description of Aromaticity in Porphyrinoids. *Journal of the American Chemical Society* **2013,** *135* (1), 315-321.

159. Bröring, M., How Should Aromaticity Be Described in Porphyrinoids? *Angewandte Chemie International Edition* **2011,** *50* (11), 2436-2438.
160. Chen, Z.; Wannere, C. S.; Corminboeuf, C.; Puchta, R.; Schleyer, P. v. R., Nucleus-Independent Chemical Shifts (NICS) as an Aromaticity Criterion. *Chemical Reviews* **2005,** *105* (10), 3842-3888.
161. Geuenich, D.; Hess, K.; Köhler, F.; Herges, R., Anisotropy of the Induced Current Density (ACID), a General Method To Quantify and Visualize Electronic Delocalization. *Chemical Reviews* **2005,** *105* (10), 3758-3772.
162. Dobrowolski, J. C., Three Queries about the HOMA Index. *ACS Omega* **2019,** *4* (20), 18699-18710.
163. Moss, G. P., Nomenclature of tetrapyrroles (Recommendations 1986). *Pure and Applied Chemistry* **1987,** *59* (6), 779-832.
164. Auwärter, W.; Écija, D.; Klappenberger, F.; Barth, J. V., Porphyrins at interfaces. In *Nature Chemistry*, Nature Publishing Group: 2015; Vol. 7, pp 105-120.
165. Gottfried, J. M., Surface chemistry of porphyrins and phthalocyanines. In *Surface Science Reports*, Elsevier: 2015; Vol. 70, pp 259-379.
166. Clair, S.; de Oteyza, D. G., Controlling a Chemical Coupling Reaction on a Surface: Tools and Strategies for On-Surface Synthesis. *Chemical Reviews* **2019,** *119* (7), 4717-4776.
167. Ikeue, T.; Aratani, N.; Osuka, A., Synthesis and characterization of fully conjugated porphyrin tapes. In *Israel Journal of Chemistry*, 2005; Vol. 45, pp 293-302.
168. Bischoff, F.; He, Y.; Riss, A.; Seufert, K.; Auwärter, W.; Barth, J. V., Exploration of Interfacial Porphine Coupling Schemes and Hybrid Systems by Bond-Resolved Scanning Probe Microscopy. In *Angewandte Chemie - International Edition*, 2018; Vol. 57, pp 16030-16035.
169. Xiang, F.; Gemeinhardt, A.; Schneider, M. A., Competition between Dehydrogenative Organometallic Bonding and Covalent Coupling of an Unfunctionalized Porphyrin on Cu(111). In *ACS Nano*, 2018; Vol. 12, pp 1203-1210.
170. Tanaka, T.; Nakamura, Y.; Osuka, A., Bay-area selective thermal [4+2] and [4+4] cycloaddition reactions of triply linked ZnII diporphyrin with o-xylylene. In *Chemistry - A European Journal*, 2008; Vol. 14, pp 204-211.
171. Kawai, S.; Takahashi, K.; Ito, S.; Pawlak, R.; Meier, T.; Spijker, P.; Canova, F. F.; Tracey, J.; Nozaki, K.; Foster, A. S.; Meyer, E., Competing Annulene and Radialene Structures in a Single Anti-Aromatic Molecule Studied by High-Resolution Atomic Force Microscopy. In *ACS Nano*, 2017; Vol. 11, pp 8122-8130.
172. Mallada, B.; de la Torre, B.; Mendieta-Moreno, J. I.; Nachtigallová, D.; Matěj, A.; Matoušek, M.; Mutombo, P.; Brabec, J.; Veis, L.; Cadart, T.; Kotora, M.; Jelínek, P., On-Surface Strain-Driven Synthesis of Nonalternant Non-Benzenoid Aromatic Compounds Containing Four- To Eight-Membered Rings. In *Journal of the American Chemical Society*, 2021; Vol. 143, pp 14694-14702.
173. Mugarza, A.; Lorente, N.; Ordejón, P.; Krull, C.; Stepanow, S.; Bocquet, M. L.; Fraxedas, J.; Ceballos, G.; Gambardella, P., Orbital specific chirality and homochiral self-assembly of achiral molecules induced by charge transfer and spontaneous symmetry breaking. In *Physical Review Letters*, 2010; Vol. 105, pp 30-33.
174. Chen, F.; Chen, X.; Liu, L.; Song, X.; Liu, S.; Liu, J.; Ouyang, H.; Cai, Y.; Liu, X.; Pan, H.; Zhu, J.; Wang, L., Chiral recognition of zinc phthalocyanine on Cu(100) surface. In *Applied Physics Letters*, 2012; Vol. 100, pp 1-5.
175. Kügel, J.; Sixta, A.; Böhme, M.; Krönlein, A.; Bode, M., Breaking Degeneracy of Tautomerization-Metastability from Days to Seconds. In *ACS Nano*, 2016; Vol. 10, pp 11058-11065.
176. Kügel, J.; Leisegang, M.; Bode, M., Imprinting directionality into proton transfer reactions of an achiral molecule. In *ACS Nano*, 2018; Vol. 12, pp 8733-8738.
177. Auwärter, W.; Seufert, K.; Bischoff, F.; Ecija, D.; Vijayaraghavan, S.; Joshi, S.; Klappenberger, F.; Samudrala, N.; Barth, J. V., A surface-anchored molecular four-level conductance switch based on single proton transfer. In *Nature Nanotechnology*, 2012; Vol. 7, pp 41-46.

178. Bischoff, F.; Seufert, K.; Auwärter, W.; Joshi, S.; Vijayaraghavan, S.; Écija, D.; Diller, K.; Papageorgiou, A. C.; Fischer, S.; Allegretti, F.; Duncan, D. A.; Klappenberger, F.; Blobner, F.; Han, R.; Barth, J. V., How surface bonding and repulsive interactions cause phase transformations: Ordering of a prototype macrocyclic compound on Ag(111). In *ACS Nano*, 2013; Vol. 7, pp 3139-3149.
179. Stępień, M.; Latos-Grażyński, L.; Szterenberg, L., 22-Hydroxybenziporphyrin: Switching of Antiaromaticity by Phenol−Keto Tautomerization. *The Journal of Organic Chemistry* **2007,** *72* (7), 2259-2270.
180. Gross, L.; Mohn, F.; Moll, N.; Schuler, B.; Criado, A.; Guitián, E.; Peña, D.; Gourdon, A.; Meyer, G., Bond-Order Discrimination by Atomic Force Microscopy. *Science* **2012,** *337* (6100), 1326-1329.
181. Ortiz, J. V., Dyson-orbital concepts for description of electrons in molecules. *The Journal of Chemical Physics* **2020,** *153* (7), 070902.
182. Neaton, J. B.; Hybertsen, M. S.; Louie, S. G., Renormalization of Molecular Electronic Levels at Metal-Molecule Interfaces. *Physical Review Letters* **2006,** *97* (21), 216405.
183. Diller, K.; Papageorgiou, A. C.; Klappenberger, F.; Allegretti, F.; Barth, J. V.; Auwärter, W., In vacuo interfacial tetrapyrrole metallation. *Chemical Society Reviews* **2016,** *45* (6), 1629-1656.
184. Harutyunyan, H.; Callsen, M.; Allmers, T.; Caciuc, V.; Blügel, S.; Atodiresei, N.; Wegner, D., Hybridisation at the organic–metal interface: a surface-scientific analogue of Hückel's rule? *Chemical Communications* **2013,** *49* (53), 5993-5995.
185. Wang, Y.; Kröger, J.; Berndt, R.; Hofer, W. A., Pushing and Pulling a Sn Ion through an Adsorbed Phthalocyanine Molecule. *Journal of the American Chemical Society* **2009,** *131* (10), 3639-3643.
186. Nacci, C.; Kanisawa, K.; Fölsch, S., Reversible switching of single tin phthalocyanine molecules on the InAs(111)A surface. *Journal of physics. Condensed matter : an Institute of Physics journal* **2012,** *24*, 394004.
187. Grill, L.; Dyer, M.; Lafferentz, L.; Persson, M.; Peters, M. V.; Hecht, S., Nano-architectures by covalent assembly of molecular building blocks. *Nature Nanotechnology* **2007,** *2* (11), 687-691.
188. Björk, J.; Hanke, F.; Stafström, S., Mechanisms of Halogen-Based Covalent Self-Assembly on Metal Surfaces. *Journal of the American Chemical Society* **2013,** *135* (15), 5768-5775.
189. Talirz, L.; Söde, H.; Dumslaff, T.; Wang, S.; Sanchez-Valencia, J. R.; Liu, J.; Shinde, P.; Pignedoli, C. A.; Liang, L.; Meunier, V.; Plumb, N. C.; Shi, M.; Feng, X.; Narita, A.; Müllen, K.; Fasel, R.; Ruffieux, P., On-Surface Synthesis and Characterization of 9-Atom Wide Armchair Graphene Nanoribbons. *ACS Nano* **2017,** *11* (2), 1380-1388.
190. Kimouche, A.; Ervasti, M. M.; Drost, R.; Halonen, S.; Harju, A.; Joensuu, P. M.; Sainio, J.; Liljeroth, P., Ultra-narrow metallic armchair graphene nanoribbons. *Nature Communications* **2015,** *6* (1), 10177.
191. Merino-Díez, N.; Garcia-Lekue, A.; Carbonell-Sanromà, E.; Li, J.; Corso, M.; Colazzo, L.; Sedona, F.; Sánchez-Portal, D.; Pascual, J. I.; de Oteyza, D. G., Width-Dependent Band Gap in Armchair Graphene Nanoribbons Reveals Fermi Level Pinning on Au(111). *ACS Nano* **2017,** *11* (11), 11661-11668.
192. Ruffieux, P.; Wang, S.; Yang, B.; Sánchez-Sánchez, C.; Liu, J.; Dienel, T.; Talirz, L.; Shinde, P.; Pignedoli, C. A.; Passerone, D.; Dumslaff, T.; Feng, X.; Müllen, K.; Fasel, R., On-surface synthesis of graphene nanoribbons with zigzag edge topology. *Nature* **2016,** *531* (7595), 489-492.
193. Blackwell, R. E.; Zhao, F.; Brooks, E.; Zhu, J.; Piskun, I.; Wang, S.; Delgado, A.; Lee, Y.-L.; Louie, S. G.; Fischer, F. R., Spin splitting of dopant edge state in magnetic zigzag graphene nanoribbons. *Nature* **2021,** *600* (7890), 647-652.
194. Xu, X.; Di Giovannantonio, M.; Urgel, J. I.; Pignedoli, C. A.; Ruffieux, P.; Müllen, K.; Fasel, R.; Narita, A., On-surface activation of benzylic C-H bonds for the synthesis of pentagon-fused graphene nanoribbons. *Nano Research* **2021,** *14* (12), 4754-4759.
195. Gröning, O.; Wang, S.; Yao, X.; Pignedoli, C. A.; Borin Barin, G.; Daniels, C.; Cupo, A.; Meunier, V.; Feng, X.; Narita, A.; Müllen, K.; Ruffieux, P.; Fasel, R., Engineering of robust topological quantum phases in graphene nanoribbons. *Nature* **2018,** *560* (7717), 209-213.

196. Pawlak, R.; Liu, X.; Ninova, S.; D'Astolfo, P.; Drechsel, C.; Sangtarash, S.; Häner, R.; Decurtins, S.; Sadeghi, H.; Lambert, C. J.; Aschauer, U.; Liu, S.-X.; Meyer, E., Bottom-up Synthesis of Nitrogen-Doped Porous Graphene Nanoribbons. *Journal of the American Chemical Society* **2020,** *142* (29), 12568-12573.
197. Ammon, M.; Haller, M.; Sorayya, S.; Maier, S., On-Surface Synthesis of Porous Carbon Nanoribbons on Silver: Reaction Kinetics and the Influence of the Surface Structure. *ChemPhysChem* **2019,** *20* (18), 2333-2339.
198. Ajayakumar, M. R.; Di Giovannantonio, M.; Pignedoli, C. A.; Yang, L.; Ruffieux, P.; Ma, J.; Fasel, R.; Feng, X., On-surface synthesis of porous graphene nanoribbons containing nonplanar [14]annulene pores. *Journal of Polymer Science* **2022,** *60* (12), 1912-1917.
199. Zheng, X. H.; Zhang, G. R.; Zeng, Z.; García-Suárez, V. M.; Lambert, C. J., Effects of antidots on the transport properties of graphene nanoribbons. *Physical Review B* **2009,** *80* (7), 075413.
200. Rosales, L.; Pacheco, M.; Barticevic, Z.; León, A.; Latgé, A.; Orellana, P. A., Transport properties of antidot superlattices of graphene nanoribbons. *Physical Review B* **2009,** *80* (7), 073402.
201. Bai, J.; Zhong, X.; Jiang, S.; Huang, Y.; Duan, X., Graphene nanomesh. *Nature Nanotechnology* **2010,** *5* (3), 190-194.
202. Liang, X.; Jung, Y.-S.; Wu, S.; Ismach, A.; Olynick, D. L.; Cabrini, S.; Bokor, J., Formation of Bandgap and Subbands in Graphene Nanomeshes with Sub-10 nm Ribbon Width Fabricated via Nanoimprint Lithography. *Nano Letters* **2010,** *10* (7), 2454-2460.
203. Simonov, K. A.; Vinogradov, N. A.; Vinogradov, A. S.; Generalov, A. V.; Zagrebina, E. M.; Svirskiy, G. I.; Cafolla, A. A.; Carpy, T.; Cunniffe, J. P.; Taketsugu, T.; Lyalin, A.; Mårtensson, N.; Preobrajenski, A. B., From Graphene Nanoribbons on Cu(111) to Nanographene on Cu(110): Critical Role of Substrate Structure in the Bottom-Up Fabrication Strategy. *ACS Nano* **2015,** *9* (9), 8997-9011.
204. Talirz, L.; Söde, H.; Cai, J.; Ruffieux, P.; Blankenburg, S.; Jafaar, R.; Berger, R.; Feng, X.; Müllen, K.; Passerone, D.; Fasel, R.; Pignedoli, C. A., Termini of Bottom-Up Fabricated Graphene Nanoribbons. *Journal of the American Chemical Society* **2013,** *135* (6), 2060-2063.
205. Simonov, K. A.; Vinogradov, N. A.; Vinogradov, A. S.; Generalov, A. V.; Zagrebina, E. M.; Mårtensson, N.; Cafolla, A. A.; Carpy, T.; Cunniffe, J. P.; Preobrajenski, A. B., Effect of Substrate Chemistry on the Bottom-Up Fabrication of Graphene Nanoribbons: Combined Core-Level Spectroscopy and STM Study. *The Journal of Physical Chemistry C* **2014,** *118* (23), 12532-12540.
206. Sánchez-Sánchez, C.; Dienel, T.; Deniz, O.; Ruffieux, P.; Berger, R.; Feng, X.; Müllen, K.; Fasel, R., Purely Armchair or Partially Chiral: Noncontact Atomic Force Microscopy Characterization of Dibromo-Bianthryl-Based Graphene Nanoribbons Grown on Cu(111). *ACS Nano* **2016,** *10* (8), 8006-8011.
207. Sun, K.; Li, X.; Chen, L.; Zhang, H.; Chi, L., Substrate-Controlled Synthesis of 5-Armchair Graphene Nanoribbons. *The Journal of Physical Chemistry C* **2020,** *124* (21), 11422-11427.
208. Zhang, H.; Lin, H.; Sun, K.; Chen, L.; Zagranyarski, Y.; Aghdassi, N.; Duhm, S.; Li, Q.; Zhong, D.; Li, Y.; Müllen, K.; Fuchs, H.; Chi, L., On-Surface Synthesis of Rylene-Type Graphene Nanoribbons. *Journal of the American Chemical Society* **2015,** *137* (12), 4022-4025.
209. de Oteyza, D. G.; García-Lekue, A.; Vilas-Varela, M.; Merino-Díez, N.; Carbonell-Sanromà, E.; Corso, M.; Vasseur, G.; Rogero, C.; Guitián, E.; Pascual, J. I.; Ortega, J. E.; Wakayama, Y.; Peña, D., Substrate-Independent Growth of Atomically Precise Chiral Graphene Nanoribbons. *ACS Nano* **2016,** *10* (9), 9000-9008.
210. Fan, Q.; Wang, T.; Dai, J.; Kuttner, J.; Hilt, G.; Gottfried, J. M.; Zhu, J., On-Surface Pseudo-High-Dilution Synthesis of Macrocycles: Principle and Mechanism. *ACS Nano* **2017,** *11* (5), 5070-5079.
211. Piquero-Zulaica, I.; Garcia-Lekue, A.; Colazzo, L.; Krug, C. K.; Mohammed, M. S. G.; Abd El-Fattah, Z. M.; Gottfried, J. M.; de Oteyza, D. G.; Ortega, J. E.; Lobo-Checa, J., Electronic Structure Tunability by Periodic meta-Ligand Spacing in One-Dimensional Organic Semiconductors. *ACS Nano* **2018,** *12* (10), 10537-10544.
212. C.F.R.A.C.Lima, L. R. G., L.M.N.B.F.Santos, J.N.Low, CCDC 782202: Experimental Crystal Structure Determination. *CSD Communication* **2012**.

213. Fan, Q.; Wang, C.; Han, Y.; Zhu, J.; Hieringer, W.; Kuttner, J.; Hilt, G.; Gottfried, J. M., Surface-Assisted Organic Synthesis of Hyperbenzene Nanotroughs. *Angewandte Chemie International Edition* **2013,** *52* (17), 4668-4672.
214. Sun, Q.; Cai, L.; Ma, H.; Yuan, C.; Xu, W., Dehalogenative Homocoupling of Terminal Alkynyl Bromides on Au(111): Incorporation of Acetylenic Scaffolding into Surface Nanostructures. *ACS Nano* **2016,** *10* (7), 7023-7030.
215. Narita, A.; Feng, X.; Hernandez, Y.; Jensen, S. A.; Bonn, M.; Yang, H.; Verzhbitskiy, I. A.; Casiraghi, C.; Hansen, M. R.; Koch, A. H. R.; Fytas, G.; Ivasenko, O.; Li, B.; Mali, K. S.; Balandina, T.; Mahesh, S.; De Feyter, S.; Müllen, K., Synthesis of structurally well-defined and liquid-phase-processable graphene nanoribbons. *Nature Chemistry* **2014,** *6* (2), 126-132.
216. Forero-Martinez, N. C.; Baumeier, B.; Kremer, K., Backbone Chemical Composition and Monomer Sequence Effects on Phenylene Polymer Persistence Lengths. *Macromolecules* **2019,** *52* (14), 5307-5316.
217. Zhang, Q.; Peng, H.; Zhang, G.; Lu, Q.; Chang, J.; Dong, Y.; Shi, X.; Wei, J., Facile Bottom-Up Synthesis of Coronene-based 3-Fold Symmetrical and Highly Substituted Nanographenes from Simple Aromatics. *Journal of the American Chemical Society* **2014,** *136* (13), 5057-5064.
218. Staab, H. A.; Diederich, F.; Krieger, C.; Schweitzer, D., Cycloarenes, a New Class of Aromatic Compounds, II. Molecular Structure and Spectroscopic Properties of Kekulene. *Chemische Berichte* **1983,** *116* (10), 3504-3512.
219. Nguyen, G. D.; Tsai, H.-Z.; Omrani, A. A.; Marangoni, T.; Wu, M.; Rizzo, D. J.; Rodgers, G. F.; Cloke, R. R.; Durr, R. A.; Sakai, Y.; Liou, F.; Aikawa, A. S.; Chelikowsky, J. R.; Louie, S. G.; Fischer, F. R.; Crommie, M. F., Atomically precise graphene nanoribbon heterojunctions from a single molecular precursor. *Nature Nanotechnology* **2017,** *12* (11), 1077-1082.
220. Shekhirev, M.; Zahl, P.; Sinitskii, A., Phenyl Functionalization of Atomically Precise Graphene Nanoribbons for Engineering Inter-ribbon Interactions and Graphene Nanopores. *ACS Nano* **2018,** *12* (8), 8662-8669.
221. Costa, P. S.; Teeter, J. D.; Enders, A.; Sinitskii, A., Chevron-based graphene nanoribbon heterojunctions: Localized effects of lateral extension and structural defects on electronic properties. *Carbon* **2018,** *134*, 310-315.
222. Cirera, B.; Sánchez-Grande, A.; de la Torre, B.; Santos, J.; Edalatmanesh, S.; Rodríguez-Sánchez, E.; Lauwaet, K.; Mallada, B.; Zbořil, R.; Miranda, R.; Gröning, O.; Jelínek, P.; Martín, N.; Ecija, D., Tailoring topological order and π-conjugation to engineer quasi-metallic polymers. *Nature Nanotechnology* **2020,** *15* (6), 437-443.
223. Madhavan, V.; Chen, W.; Jamneala, T.; Crommie, M. F.; Wingreen, N. S., Local spectroscopy of a Kondo impurity: Co on Au(111). *Physical Review B* **2001,** *64* (16), 165412.
224. Martinez-Castro, J.; Bolat, R.; Fan, Q.; Werner, S.; Arefi, H. H.; Esat, T.; Sundermeyer, J.; Wagner, C.; Gottfried, J. M.; Temirov, R.; Ternes, M.; Tautz, F. S., Disentangling the Complex Electronic Structure of an Adsorbed Nanographene: Cycloarene C108. *arXiv e-prints* **2021**, arXiv:2110.11449.
225. El-Sayed, A.; Piquero-Zulaica, I.; Abd El-Fattah, Z. M.; Kormoš, L.; Ali, K.; Weber, A.; Brede, J.; de Oteyza, D. G.; Lobo-Checa, J.; Ortega, J. E.; Corso, M., Synthesis of Graphene Nanoribbons on a Kinked Au Surface: Revealing the Frontier Valence Band at the Brillouin Zone Center. *The Journal of Physical Chemistry C* **2020,** *124* (28), 15474-15480.
226. Hieulle, J.; Carbonell-Sanromà, E.; Vilas-Varela, M.; Garcia-Lekue, A.; Guitián, E.; Peña, D.; Pascual, J. I., On-Surface Route for Producing Planar Nanographenes with Azulene Moieties. *Nano Letters* **2018,** *18* (1), 418-423.
227. Kawai, S.; Kher-Elden, M. A.; Sadeghi, A.; Abd El-Fattah, Z. M.; Sun, K.; Izumi, S.; Minakata, S.; Takeda, Y.; Lobo-Checa, J., Near Fermi Superatom State Stabilized by Surface State Resonances in a Multiporous Molecular Network. *Nano Letters* **2021,** *21* (15), 6456-6462.
228. Feng, M.; Zhao, J.; Petek, H., Atomlike, Hollow-Core–Bound Molecular Orbitals of C60. *Science* **2008,** *320* (5874), 359-362.

229. Craes, F.; Runte, S.; Klinkhammer, J.; Kralj, M.; Michely, T.; Busse, C., Mapping Image Potential States on Graphene Quantum Dots. *Physical Review Letters* **2013,** *111* (5), 056804.
230. Talirz, L.; Söde, H.; Kawai, S.; Ruffieux, P.; Meyer, E.; Feng, X.; Müllen, K.; Fasel, R.; Pignedoli, C. A.; Passerone, D., Band Gap of Atomically Precise Graphene Nanoribbons as a Function of Ribbon Length and Termination. *ChemPhysChem* **2019,** *20* (18), 2348-2353.
231. Su, J.; Fan, W.; Mutombo, P.; Peng, X.; Song, S.; Ondráček, M.; Golub, P.; Brabec, J.; Veis, L.; Telychko, M.; Jelínek, P.; Wu, J.; Lu, J., On-Surface Synthesis and Characterization of [7]Triangulene Quantum Ring. *Nano Letters* **2021,** *21* (1), 861-867.
232. Mairena, A.; Baljozovic, M.; Kawecki, M.; Grenader, K.; Wienke, M.; Martin, K.; Bernard, L.; Avarvari, N.; Terfort, A.; Ernst, K.-H.; Wäckerlin, C., The fate of bromine after temperature-induced dehydrogenation of on-surface synthesized bisheptahelicene. *Chemical Science* **2019,** *10* (10), 2998-3004.
233. Zuzak, R.; Jančařík, A.; Gourdon, A.; Szymonski, M.; Godlewski, S., On-Surface Synthesis with Atomic Hydrogen. *ACS Nano* **2020,** *14* (10), 13316-13323.
234. Fan, Q.; Werner, S.; Tschakert, J.; Ebeling, D.; Schirmeisen, A.; Hilt, G.; Hieringer, W.; Gottfried, J. M., Precise Monoselective Aromatic C–H Bond Activation by Chemisorption of Meta-Aryne on a Metal Surface. *Journal of the American Chemical Society* **2018,** *140* (24), 7526-7532.
235. Juppe, G.; Rau, H., The attapulgus clay-catalysed thermal decomposition of terphenyls. *Journal of Applied Chemistry* **1969,** *19* (4), 120-124.
236. Tan, T. H.; Wong, R. J.; Scott, J.; Ng, Y. H.; Taylor, R. A.; Aguey-Zinsou, K.-F.; Amal, R., Multipronged Validation of Oxalate C–C Bond Cleavage Driven by Au-TiO2 Interfacial Charge Transfer Using Operando DRIFTS. *ACS Catalysis* **2018,** *8* (8), 7158-7163.
237. Tan, T. H.; Scott, J.; Ng, Y. H.; Taylor, R. A.; Aguey-Zinsou, K.-F.; Amal, R., Understanding Plasmon and Band Gap Photoexcitation Effects on the Thermal-Catalytic Oxidation of Ethanol by TiO2-Supported Gold. *ACS Catalysis* **2016,** *6* (3), 1870-1879.
238. Skraba-Joiner, S. L.; Holt, C. J.; Johnson, R. P., Acid-catalyzed rearrangements in arenes: interconversions in the quaterphenyl series. *Beilstein Journal of Organic Chemistry* **2019,** *15*, 2655-2663.
239. Klein, M. T.; Lapinas, A. T.; Gates, B. C.; Read, C. J.; Lyons, J. E.; Macris, A., Cleavage of biphenyl moieties: An efficient new reaction pathway in catalytic hydrocracking. *Journal of Catalysis* **1992,** *137* (2), 504-509.
240. Pignedoli, C. A.; Laino, T.; Treier, M.; Fasel, R.; Passerone, D., A simple approach for describing metal-supported cyclohexaphenylene dehydrogenation. *The European Physical Journal B* **2010,** *75* (1), 65-70.
241. Ormsby, J. L.; Black, T. D.; Hilton, C. L.; Bharat; King, B. T., Rearrangements in the Scholl oxidation: implications for molecular architectures. *Tetrahedron* **2008,** *64* (50), 11370-11378.
242. King, B. T.; Kroulík, J.; Robertson, C. R.; Rempala, P.; Hilton, C. L.; Korinek, J. D.; Gortari, L. M., Controlling the Scholl Reaction. *The Journal of Organic Chemistry* **2007,** *72* (7), 2279-2288.
243. Hendrich, C. M.; Sekine, K.; Koshikawa, T.; Tanaka, K.; Hashmi, A. S. K., Homogeneous and Heterogeneous Gold Catalysis for Materials Science. *Chemical Reviews* **2021,** *121* (14), 9113-9163.
244. Chintawar, C. C.; Yadav, A. K.; Kumar, A.; Sancheti, S. P.; Patil, N. T., Divergent Gold Catalysis: Unlocking Molecular Diversity through Catalyst Control. *Chemical Reviews* **2021,** *121* (14), 8478-8558.
245. Berger, R. J. F.; Fuchter, M. J.; Krossing, I.; Rzepa, H. S.; Schaefer, J.; Scherer, H., Gold(i) mediated rearrangement of [7]-helicene to give a benzo[cd]pyrenium cation embedded in a chiral framework. *Chemical Communications* **2014,** *50* (40), 5251-5253.
246. Björk, J.; Stafström, S.; Hanke, F., Zipping Up: Cooperativity Drives the Synthesis of Graphene Nanoribbons. *Journal of the American Chemical Society* **2011,** *133* (38), 14884-14887.
247. Blankenburg, S.; Cai, J.; Ruffieux, P.; Jaafar, R.; Passerone, D.; Feng, X.; Müllen, K.; Fasel, R.; Pignedoli, C. A., Intraribbon Heterojunction Formation in Ultranarrow Graphene Nanoribbons. *ACS Nano* **2012,** *6* (3), 2020-2025.

248. Ma, C.; Xiao, Z.; Bonnesen, P. V.; Liang, L.; Puretzky, A. A.; Huang, J.; Kolmer, M.; Sumpter, B. G.; Lu, W.; Hong, K.; Bernholc, J.; Li, A.-P., On-surface cyclodehydrogenation reaction pathway determined by selective molecular deuterations. *Chemical Science* **2021,** *12* (47), 15637-15644.
249. Shen, C.; Zhang, G.; Ding, Y.; Yang, N.; Gan, F.; Crassous, J.; Qiu, H., Oxidative cyclo-rearrangement of helicenes into chiral nanographenes. *Nature Communications* **2021,** *12* (1), 2786.
250. Stetsovych, O.; Švec, M.; Vacek, J.; Chocholoušová, J. V.; Jančařík, A.; Rybáček, J.; Kosmider, K.; Stará, I. G.; Jelínek, P.; Starý, I., From helical to planar chirality by on-surface chemistry. *Nature Chemistry* **2017,** *9* (3), 213-218.
251. Dössel, L.; Gherghel, L.; Feng, X.; Müllen, K., Graphene Nanoribbons by Chemists: Nanometer-Sized, Soluble, and Defect-Free. *Angewandte Chemie International Edition* **2011,** *50* (11), 2540-2543.
252. Sakaguchi, H.; Song, S.; Kojima, T.; Nakae, T., Homochiral polymerization-driven selective growth of graphene nanoribbons. *Nature Chemistry* **2017,** *9* (1), 57-63.
253. Rappe, A. K.; Casewit, C. J.; Colwell, K. S.; Goddard, W. A.; Skiff, W. M., UFF, a full periodic table force field for molecular mechanics and molecular dynamics simulations. *Journal of the American Chemical Society* **1992,** *114* (25), 10024-10035.
254. Hanwell, M. D.; Curtis, D. E.; Lonie, D. C.; Vandermeersch, T.; Zurek, E.; Hutchison, G. R., Avogadro: an advanced semantic chemical editor, visualization, and analysis platform. *Journal of Cheminformatics* **2012,** *4* (1), 17.
255. Skraba-Joiner, S. L.; Brulet, J. W.; Song, M. K.; Johnson, R. P., Acid-Catalyzed Skeletal Rearrangements in Arenes: Aryl versus Alkyl Ring Pirouettes in Anthracene and Phenanthrene. *The Journal of Organic Chemistry* **2017,** *82* (24), 13076-13083.
256. Paserba, K. R.; Gellman, A. J., Kinetics and Energetics of Oligomer Desorption from Surfaces. *Physical Review Letters* **2001,** *86* (19), 4338-4341.
257. Paserba, K. R.; Gellman, A. J., Effects of conformational isomerism on the desorption kinetics of n-alkanes from graphite. *The Journal of Chemical Physics* **2001,** *115* (14), 6737-6751.
258. Xiang, F.; Li, C.; Wang, Z.; Liu, X.; Jiang, D.; Leng, X.; Ling, J.; Wang, L., Direct observation of copper-induced metalation of 5,15-diphenylporphyrin on Au(111) by scanning tunneling microscopy. *Surface Science* **2015,** *633*, 46-52.
259. Wang, X.-Y.; Yao, X.; Müllen, K., Polycyclic aromatic hydrocarbons in the graphene era. *Science China Chemistry* **2019,** *62* (9), 1099-1144.
260. Grzybowski, M.; Skonieczny, K.; Butenschön, H.; Gryko, D. T., Comparison of Oxidative Aromatic Coupling and the Scholl Reaction. *Angewandte Chemie International Edition* **2013,** *52* (38), 9900-9930.
261. Xu, Z.; Kojima, T.; Wang, W.; Kaushik, K.; Saliniemi, A.; Nakae, T.; Sakaguchi, H., On-surface synthesis of graphene clusters from a Z-bar-linkage precursor with quaterphenyl branches. *Materials Chemistry Frontiers* **2018,** *2* (4), 775-779.
262. Stahley, M. R.; Strobel, S. A., RNA splicing: group I intron crystal structures reveal the basis of splice site selection and metal ion catalysis. *Current Opinion in Structural Biology* **2006,** *16* (3), 319-326.

Acknowledgements

Now, at the end of this stage of my career I would like to thank all those involved in the work that was presented. Without them it would not even exist.

Willi Auwärter and Johannes Barth for allowing me realize my doctorate in their group, and above all, for allowing me to use their equipment, which is without a doubt the most wonderful type of machine I have had the privilege to use as part of my career.

Knud Seufert, Karl Eberle and Reinhold Schneider for their technical and scientific expertise required to keep the machine up and running.

Viktoria Blaschek for her support with all the paperwork.

Alex Riss and Ignacio Piquero Zulaica for their continuous collaboration as the projects would have never seen completion without them, but I am also grateful for the much necessary extracurricular activities, the rides to the lakes were a healthy distraction.

Maryam Ebrahimi for the scientific discussions, the days we went hiking to the mountains and the delicious rice which I have not been able to replicate.

In no particular order, to my colleagues: Jacob Ducke, Tobias Painter, Karolina Stoiber, Domenik Zimmermann, Felix Haas, Dennis Meier, Andreas Walz, Tobias Weiß, Martin Uphoff, Matthias Kleppel. The casual conversation and the many dishes shared with them made everything more amiable. The late evenings playing Mario Kart 64, Super Smash Brothers, and PUBG were fantastic, most specially during the Covid-19 pandemic lockdowns.

Wei Ran, Nan Cao and Biao Yang for the many times they invited me to the hot-pot with them.

Johannes Küchle, Sena Tömekçe and Pablo Vezzoni who became the last people I could talk to and nag every five minutes (seconds really) during the time it took to write all this.

There is much more to be grateful for, but hardly will I be able to condense it here. I will cherish the time spent around these most fine people and memories made with them. May the heavens keep them safe.

Special considerations to Scihub, Library Genesis (Libgen), Maria Rascon and Martha Minjarez for providing key literature when there was no other option to obtain it.

The amount of people from Mexico that helped and made this possible is simply too large to even begin with. Funding for my scholarship came from CONACYT, under CVU number 591246.